PERFORMANCE OF AXIAL COMPRESSORS

WITH ASYMMETRIC INLET FLOWS

Thesis by

Robert Katz

In Partial Fulfillment of the Requirements

For the Degree of

Doctor of Philosophy

California Institute of Technology

Pasadena, California

1958

ACKNOWLEDGEMENTS

ABSTRACT

An experimental and analytical investigation was undertaken to determine the influence of asymmetric inlet flows on the performance of axial turbomachinery.

Overall performance measurements and circumferential surveys of total pressures, velocities and flow angles were obtained in an axial compressor with inlet disturbances covering approximately 25 ^{o}/o of the inlet annulus area. Three configurations were tested to find the principal effects in a single rotor, a complete stage and a multi-stage machine. A two-dimensional linearized theory was developed which includes the effect of losses and leaving angle deviations in the blade rows. The analysis may also be applied to propagating stall so that this theory allows a unified treatment of the two phenomena.

Introducing the inlet disturbances did not alter the two-dimensional character of the flow in the compressor. Considerable attenuation of the disturbances occurred through a single rotor and the disturbances were almost completely attenuated downstream of a three stage configuration. The mutual interference of the blade rows with small axial spacing was responsible for significant stator losses. The overall performance deteriorated primarily due to losses occurring in the blade rows. In the three configurations tested the inception of propagating stall, as based on the mean flow rate, was essentially unchanged. The theory qualitatively described the flow behavior and a simple application of the theory would give an estimate of the blade forces.

TABLE OF CONTENTS

NOTATION

a Constant

b Constant

c Constant

d Constant

fn Function

F Blade Force

H Perturbation Total Pressure $= \dfrac{p}{\rho} + Uu + Vv$ (Section 2:1)

k Constant

L Total Pressure Loss Coefficient

L' Slope of the Total Pressure Loss Coefficient Curve

$\mathscr{L}$ Loss Function (Section 2:2.1)

n Wave Number

p Perturbation Static Pressure

p' Static Pressure

P Mean Static Pressure

P_a Atmospheric Pressure

P_t Total Pressure

$\mathscr{P}$ Harmonic Pressure Function $= \dfrac{p}{\rho}$ (Section 2:1)

r Radius

r_h Hub Radius

r_t Tip Radius

s Blade Spacing

S Survey Plane (Figures 28 and 40)

u Perturbation Axial Velocity

u' Axial Velocity

U Mean Axial Velocity

v Perturbation Whirl Velocity

v' Whirl Velocity

V Mean Whirl Velocity

x Dimensionless Axial Coordinate $= \dfrac{x'}{r}$

x' Axial Coordinate

y Dimensionless Whirl Coordinate $= \dfrac{y'}{r}$

y' Whirl Coordinate

β Relative Flow Angle

γ Constant

δ Slope of the Leaving vs Inlet Angle Curve (Section 2:2.1)

Δ Incremental Change

ϵ Fraction of the Cascade Stalled (Section 2:2.1)

η Efficiency $= \dfrac{\psi}{\psi'}$

θ Flow Angle

Θ Angle Perturbation Function $= Uv - Vu$ (Section 2:1)

ζ Dimensionless Radius $= \dfrac{r}{r_t}$

ρ Fluid Density

σ Cascade Solidity $= \dfrac{\text{Blade Chord}}{\text{Blade Spacing}}$

φ Flow Coefficient $= \dfrac{U}{\omega r}$

ϕ Perturbation Flow Coefficient $= \dfrac{u}{\omega r_t}$

$\bar{\phi}$ Mean Flow Coefficient $= \dfrac{U}{\omega r_t}$

ψ Total Pressure Coefficient $= \dfrac{P_t - P_a}{\frac{1}{2}\rho(\omega r_t)^2}$

$\bar{\psi}$ Mean Total Pressure Coefficient

$\bar{\psi}'$ Work Coefficient (Equation 2.37)

ψ_s Static Pressure Coefficient $= \dfrac{P - P_a}{\frac{1}{2}\rho(\omega r_t)^2}$

ω Rotational Speed of the Rotor

Subscripts, etc.

$1, 2, 3, \cdots$	Flow Region, Constant Numeration, etc.
$I, II, III, \cdots$	Survey Plane Location (Figures 28 and 40)
R	Rotor
S	Stator
V	Inlet Vanes
$*$	Denotes Conjugate Function (Equation 2.14)
$\wedge$	Critical Value (Section 2:2.1)
$-$	Average Value

I. INTRODUCTION

The design of axial compressors usually presupposes a uniform flow at the inlet section, however, in practice this is not always realized. The installation of a compressor normally involves some form of ducting to direct the flow to the inlet. Due to the entrance design, bends, boundry layer build-up, and even obstacles in the flow path the flow entering the compressor inlet may be far from uniform. There is considerable interest in the distorted inlet flow problem primarily because of the use of axial compressors as a component of turbojet engines. The installation of turbojet engines in aircraft involves design compromises which entail at times complex induction systems. Common aircraft induction systems include the twin sides ducts, bottom scoops and nacelles with center bodies. These systems have various characteristics as to their ability to tolerate off-design conditions of pitch, yaw, flow-rate, etc. In any case the flow distortions which result from the induction systems impose great demands on the compressor to handle the distortions not only as it involves performance but also as it involves the fluid forces acting on the blades.

The flow distortions at the compressor inlet would, in general, be quite complex. However, the inlet distortions may be divided into two classes. One would include distortions which have a radial distribution but are axially symmetric and the other would include the distortions which have a circumferential distribution but no radial variation.

The first known work which was undertaken to determine the effect of inlet distortions on axial compressors was in 1950 by Conrad

and Sobolewski (1). They determined the overall performance of a complete turbojet engine with various radial disturbances. One example of an asymmetric inlet distortion which was to similate a twin-duct inlet was tested. Some test configurations had a slight detrimental effect while others a slight benefical effect on the performance. In general the compressor efficiencies were reduced. Their conclusions were that for the range of distortions tested the effect on performance was not serious.

Alford (2) also conducted an experimental investigation of a complete turbojet engine with various radial and asymmetric inlet distortions. He recognized that a non-uniform inlet condition may effect the propagating stall limit, but for the two asymmetric disturbances tested he found no effect. The disturbances tested were small and the efficiency and pressure ratio suffered small decreases. Strain gages were employed on the rotor and stator during the tests but no serious stresses were noted until the compressor entered a stalling condition.

There is a striking analogy between propagating stall and the asymmetric inlet distortion and the free and forced oscillations of a vibrating system. The propagating stall corresponds to a free or self-induced oscillation and the asymmetric inlet distortion to a forced oscillation. This analogy was first recognized by Rannie and Marble (3). In their paper they treat the two phenomena from a unified theoretical point of view.

Since propagating stall and the asymmetric inlet flow may be considered from a unified theoretical approach the various assumptions in the propagating stall theories may be compared with the assumptions

to be made here. All the theories make the same initial assumptions,
namely, a two-dimensional small perturbation type of flow of an
incompressible and inviscid fluid. A single blade row is considered
and this is replaced by an actuator line. In order to solve the problem
two matching conditions are required across the blade row in addition
to the continuity of axial velocity. The assumptions for the two
remaining blade row characteristics are as follows:

1. Emmons (4) assumed the static pressure is constant
    downstream of the blade row which essentially uncouples
    the regions upstream and downstream of the blade row.
    The stall is a result of a partial constriction of the blade
    channel due to flow separating from the blades. The
    available channel area is a function of the inlet angle and
    these are connected by a time lag.

2. Stenning (5) extended the theory of Emmons but
    differentiated between the boundary layer separation
    time lag and a time lag due to the inertia of the fluid in
    the blade passages.

3. Sears (6, 7) assumed small turning through the blade row
    and a constant leaving angle. Two cases for the remain-
    ing blade row characteristic were considered: (a) a lift
    dominated case where the total pressure across the
    cascade was conserved and the blade circulation and
    incidence angle of attack were connected by a time lag
    and (b) a drag dominated case where the total pressure

drop across the cascade was connected to the incidence angle by a time lag.

4. Marble (8) considered general relations for the variation of the downstream angle and pressure in terms of the upstream conditions. To obtain a solution he simplified the conditions and assumed small turning through a cascade of infinite solidity. The remaining condition was a non-linear one. Marble assumed that there was zero pressure rise downstream of the stall cell and normal pressure rise elsewhere.

5. Falk (9) extended Marble's theory to include a time lag between the incidence angle and the pressure condition across the stall cell.

6. Benenson (10) following a theory proposed by Professor W. D. Rannie assumed a linear relationship between the total pressure loss across the cascade and the incidence angle. The leaving angle from the cascade was assumed to be constant and finite turning through the cascade was allowed.

The theory to be presented here differs from the propagating stall theories, with the exception of Benenson's, in that the turning through the cascade is permitted to be large. The leaving angle from the cascade is assumed to be a linear function of the incidence angle. Two cases for cascade loss characteristics are considered. The first case assumes a linear relation between the total pressure loss and the

incidence angle as in Professor W. D. Rannie's theory. The second case assumes a non-linear relation between the total pressure loss and the incidence angle similar to Professor F. E. Marble's treatment.

The solution of the asymmetric inlet distortion problem involves an inhomogeneous set of equations. The inhomogeneous terms are functions of the total pressure disturbance upstream of the blade row. From the solution the characteristics of the entire flow field may be found, and the overall performance and additional blade forces may also be computed.

The analysis may be easily extended to the problem of propagating stall. The coordinate system is fixed to the stall cell. That is, a uniform velocity equal to the propagating stall speed is superposed on to the flow field so that the stall cell is stationary with respect to the coordinate system. Since the total pressure is uniform upstream of the blade row the solution is in the form of a homogeneous set of equations. A non-trivial solution of the homogeneous equations determines the propagating stall speed in terms of the parameters of the flow field and the blade row characteristics.

This investigation includes both a theoretical and experimental study of the effect of the asymmetric class of inlet flows on the performance of axial compressors. The theory is developed first in considerable detail in order that the physical processes may be indicated. Example results for a particular inlet disturbance are included to illustrate the theory and to allow the experimental results to be more readily understood.

The experiments were performed in a three stage axial compressor. Since it was possible to remove blades the compressor could be operated in a number of arrangements. In order to determine the influence of blade row spacing and multi-stage effects three arrangements were tested. These were: a single stage configuration with the blade rows axially displaced by two chord lengths, a single stage configuration with normal spacing between blade rows and the three stage configuration.

The inlet disturbances were introduced by means of screens blocking a sector of the inlet annulus. Downstream of the blocked area there is a total pressure loss which defines the magnitude of the disturbance. The magnitude and extent of the inlet disturbance could easily be controlled by varying the size and solidity of the blockage screens.

The test results consist of overall performance measurements and detailed circumferential surveys of total pressures, flow angles and velocities. The detailed surveys were made at several radial sections upstream and downstream of the blade rows. In addition the effect of the inlet disturbances on the inception of propagating stall was also determined.

A direct comparison of the theory with the experimental results for one case is included to illustrate the influence of losses and the leaving angle variation. Discrepancies between the theory and the experimental results are discussed in some detail.

II. THEORETICAL MODEL OF THE ASYMMETRIC
INLET DISTORTION

2:1 Description of the Flow Field

Consider the two-dimensional flow through an isolated cascade. The cascade is at the origin of the X' axis and extends from $-\pi r$ to πr along the y' axis. The flow field is confined to the infinite strip of width $2\pi r$, figure 1.

This two-dimensional flow field may be thought of as being developed from an isolated cylindrical cascade in an infinite duct of very high hub-tip ratio. Radial flow would be negligible so Cartesian coordinates may be used. The X' coordinate is along the axis of the duct and the y' coordinate along the circumferential direction. Being a cylindrical duct the y' coordinate must be periodic of period $2\pi r$.

The asymmetric inlet flow will be assumed to be a small disturbance superposed upon a known mean flow. The disturbance is stationary with respect to the coordinate system and the wave length of the disturbance will be assumed to be large compared to the blade spacing. Long wave lengths imply that the effects of individual blades on the flow may be neglected and this will be assumed to be true even when there is relative motion between the disturbance and cascade. Therefore, under these assumptions the flow will at least be quasi-steady.

Assuming an inviscid and incompressible fluid the equations governing the flow are,

$$\frac{\partial u'}{\partial x'} + \frac{\partial v'}{\partial y'} = 0$$

$$u'\frac{\partial u'}{\partial x'} + v'\frac{\partial u'}{\partial y'} = -\frac{\partial}{\partial x'}\frac{p'}{\rho}$$

$$u'\frac{\partial v'}{\partial x'} + v'\frac{\partial v'}{\partial y'} = -\frac{\partial}{\partial y'}\frac{p'}{\rho}$$

(2.1)

The velocity and pressure terms may be separated into their mean and perturbation components.

$$u' = U + u$$

$$v' = V + v$$

$$p' = P + p$$

(2.2)

The terms U, V and P define the known mean flow and have constant values upstream and downstream of the blade row. The variable terms u, v and p have zero average values.

Equations 2.1 may be linearized to:

$$\frac{\partial u}{\partial x'} + \frac{\partial v}{\partial y'} = 0$$

$$U\frac{\partial u}{\partial x'} + V\frac{\partial u}{\partial y'} = -\frac{\partial}{\partial x'}\frac{p}{\rho}$$

$$U\frac{\partial v}{\partial x'} + V\frac{\partial v}{\partial y'} = -\frac{\partial}{\partial y'}\frac{p}{\rho}$$

(2.3)

Equations 2.3 can be shown to be equivalent to the equations,

$$\frac{\partial}{\partial y'} (Uv - Vu) = \frac{\partial}{\partial x'} \frac{p}{\rho}$$

$$\frac{\partial}{\partial x'} (Uv - Vu) = -\frac{\partial}{\partial y'} \frac{p}{\rho} \qquad (2.4)$$

$$\left(U \frac{\partial}{\partial x'} + V \frac{\partial}{\partial y'} \right) \left(\frac{p}{\rho} + Uu + Vv \right) = 0$$

The following notation will be introduced.

$$\Theta = Uv - Vu$$

$$\mathcal{P} = \frac{p}{\rho}$$

$$H = \frac{p}{\rho} + Uu + Vv \qquad (2.5)$$

$$x = \frac{x'}{r}$$

$$y = \frac{y'}{r}$$

Therefore, equations 2.4 may be written as,

$$\frac{\partial \Theta}{\partial y} = \frac{\partial \mathcal{P}}{\partial x}$$

$$\frac{\partial \Theta}{\partial x} = -\frac{\partial \mathcal{P}}{\partial y} \qquad (2.6)$$

$$\left(U \frac{\partial}{\partial x} + V \frac{\partial}{\partial y} \right) H = 0$$

The quantity H is proportional to the perturbation total pressure. The last of equations 2.6 states that H is constant along the mean streamlines defined by U and V. It then follows that

$$H(x, y) = H \left(y - x \frac{V}{U} \right).$$

The first two of equations 2.6 are the Cauchy-Riemann conditions. Therefore, $\mathcal{P}$ and Θ are conjugate harmonic functions and both satisfy the two-dimensional Laplace equation. If one of the functions $\mathcal{P}$ or Θ is known then the other is consequently known.

The function $\mathcal{P}$ is clearly proportional to the perturbation pressure.

The function Θ is proportional to the perturbed flow angle, $\Delta\theta$, figure 2. This can be verified by expanding both sides of the equation

$$tan\left(\theta + \Delta\theta\right) = \frac{V + v}{U + u}$$

and retaining the first order terms. Then,

$$\Delta\theta = \frac{cos^2\theta}{U^2}\,\Theta$$

The function Θ determines the direction of the perturbed streamlines.

The cascade at the origin of the X axis divides the flow field into two regions of different mean flows. Therefore, one set of equations 2.6 defines the upstream and another set the downstream region. Denote the upstream region by the subscript 1 and the downstream region by the subscript 2.

Far from the origin the cascade has a negligible effect on the flow and the $\mathcal{P}$ and Θ functions must, therefore, vanish far from the cascade. The boundary conditions are:

$$\lim_{x \to -\infty} \varphi_1(x, y) = \lim_{x \to -\infty} \theta_1(x, y) = 0$$

$$\lim_{x \to \infty} \varphi_2(x, y) = \lim_{x \to \infty} \theta_2(x, y) = 0 \qquad (2.7)$$

$$f_n(x, y) = f_n(x, y + 2\pi)$$

The last of the boundary conditions merely states that the various functions are periodic of period 2π which is necessary to represent a cylindrical cascade.

In what follows it will be assumed that H_1 is the known function. If H_1 is known anywhere upstream of the cascade it is known everywhere upstream by equation 2.6. If the velocity components were given at the upstream infinity H_1 could be found, and conversely.

The general solution may now be constructed.

Because of the periodicity in y the functions are conveniently represented by Fourier series. Assume H_1 is given by,

$$H_1 = \sum_{n=1}^{\infty} a_{1_n} \cos n\left(y - x \frac{V_1}{U}\right) + b_{1_n} \sin n\left(y - x \frac{V_1}{U}\right) \qquad (2.8)$$

A solution for θ_1 which satisfies the Laplace equation and the boundary conditions is

$$\theta_1 = \sum_{n=1}^{\infty} \left(c_{1_n} \cos ny + d_{1_n} \sin ny\right) e^{nx} \qquad (2.9)$$

Since Θ_1 has been assumed then it follows immediately from the Cauchy-Riemann conditions that

$$\mathcal{P}_1 = \sum_{n=1}^{\infty} \left(d_{1_n} \cos ny - c_{1_n} \sin ny \right) e^{nx} \qquad (2.10)$$

The functions downstream of the cascade may similarly be written down.

$$H_2 = \sum_{n=1}^{\infty} a_{2_n} \cos n\left(y - x\frac{V_2}{U} \right) + b_{2_n} \sin n\left(y - x\frac{V_2}{U} \right) \qquad (2.11)$$

$$\Theta_2 = \sum_{n=1}^{\infty} \left(c_{2_n} \cos ny + d_{2_n} \sin ny \right) e^{-nx} \qquad (2.12)$$

$$\mathcal{P}_2 = \sum_{n=1}^{\infty} \left(-d_{2_n} \cos ny + c_{2_n} \sin ny \right) e^{-nx} \qquad (2.13)$$

With the exception of H_1 the Fourier coefficients are as yet unknown. The unknown coefficients are found by matching the upstream and downstream solutions at the cascade. Three matching relations are needed to completely specify the solution since there are three unknowns u, v and p or equivalently $\mathcal{P}$, Θ and H.

The cascade will be replaced by an actuator line at the origin of the x axis. Since the flow through the blade channels is governed by algebraic equations a finite chord length would only introduce a phase shift between the solutions of regions 1 and 2. Any phase shift may be

ignored.

The three matching equations result in six algebraic equations due to the linear independence of the trigonometric terms. For a inlet disturbance of n wave lengths there are $6n$ algebraic equations for the $6n$ unknowns (c_{1_n}, d_{1_n}, c_{2_n}, d_{2_n}, a_{2_n}, b_{2_n}) in terms of the $2n$ knowns (a_{1_n}, b_{1_n}).

It will prove convenient in the analysis that follows to introduce an operational notation. If Θ_1 is assumed to be given by equation 2.9 then it may be shown that P_1 is given by

$$P_1(x,y) = \frac{1}{2\pi} \int_{-\pi}^{\pi} \Theta_1(x,\eta) \cot\left(\frac{y-\eta}{2}\right) d\eta$$

Therefore, P_1 is just the Hilbert transform of Θ_1.

Define the Hilbert transform as the conjugate function and denote it by an asterisk.

$$f_n^*(x,y) = \frac{1}{2\pi} \int_{-\pi}^{\pi} f_n(x,\eta) \cot\left(\frac{y-\eta}{2}\right) d\eta \qquad (2.14)$$

The following relations may be proved.

$$P_1^*(x,y) = \Theta_1(x,y)$$
$$\Theta_1^*(x,y) = -P_1(x,y)$$
$$P_2^*(x,y) = -\Theta_2(x,y) \qquad (2.15)$$
$$\Theta_2^*(x,y) = P_2(x,y)$$

and

$$\left(\cos n y\right)^* = \sin n y$$

$$\left(\sin n y\right)^* = -\cos n y$$

$$\left\{\left[f_n(x,y)\right]^*\right\}^* = -f_n(x,y) \qquad (2.16)$$

If the concept of the conjugate function is used the three matching equations and their conjugates define six algebraic equations. These are just sufficient to determine the 6 unknowns (P_1, θ_1, P_2, θ_2, H_2, H_2^*) in terms of the 2 knowns (H_1, H_1^*).

The extension of the analysis to multiple blade rows will be indicated by an example in a later section.

2:2 Matching Conditions at a Blade Row

2:2.1 Rotor Blade Row

The three matching conditions at the blade row will be found from the continuity equation, a relation for the leaving angle from the cascade and the Bernoulli equation.

As in the previous section the subscripts 1 and 2 will denote the upstream and downstream regions, respectively.

It is clear the continuity equation requires that

$$u_1(0, y) = u_2(0, y) \qquad (2.17)$$

The leaving angle from a blade row, β_2, can in general be written

$$\beta_2 = \overline{\beta_2} + T(\beta_1)$$

where $\overline{\beta_2}$ is a constant and $T(\beta_1)$ is a function of the inlet angle, β_1, figure 3.

For very high solidity, $T(\beta_1) = 0$ and the leaving angle is a constant regardless of the upstream conditions. $T(\beta_1)$ will be presumed known from cascade tests or otherwise.

Since the inlet disturbance perturbs the flow field, the inlet angle will be a function of the circumferential coordinate. The relationship for the leaving angle and, therefore, the second matching condition will be found from the linear term of the Taylor expansion about the operating point.

$$\Delta\beta_2 = \delta_R \, \Delta\beta_1 \qquad (2.18)$$

The δ_R is the slope of the leaving angle vs inlet angle curve evaluated at the point corresponding to the mean inlet angle. The slope would generally be small and positive for normal solidities while a $\delta_R = 0$ corresponds to infinite solidity.

The Bernoulli equation for the flow through a rotor is

$$p_1' + \frac{1}{2}\rho\left[u_1'^2 + \left(v_1' - \omega r\right)^2\right] = p_2' + \frac{1}{2}\rho\left[u_2'^2 + \left(v_2' - \omega r\right)^2\right]$$
$$+ \frac{1}{2}\rho u_1'^2 \, L_R(\tan\beta_1)$$

where the assumption of quasi-steady flow is implied. The L_R is a loss coefficient referred to the upstream axial velocity and is a function of the tangent of the relative inlet angle.

Two cases for the loss through the rotor will be considered:
(1) a linear and (2) a non-linear loss relationship.

(1)   The linear loss representation is shown schematically in figure 4. The mean value of L_R is known from the curve at a given flow condition. When the flow is perturbed the loss may be found from the Taylor expansion.

$$L_R\left\{tan\left(\beta_1 + \Delta\beta_1\right)\right\} = L_R\left\{tan\beta_1\right\} + \Delta\beta_1 \, sec^2\beta_1 \, L_R'\left\{tan\beta_1\right\}$$

L_R' is the slope of the curve at the mean operating point.

The Bernoulli equation for the mean flow is

$$P_1 + \frac{1}{2}\rho\left[U^2 + (V_1 - \omega r)^2\right] = P_2 + \frac{1}{2}\rho\left[U^2 + (V_2 - \omega r)^2\right] + \frac{1}{2}\rho U^2 L_R$$

The Bernoulli equation for the perturbed flow yields the remaining matching relation.

$$\frac{p_1}{\rho} + U u_1 + (V_1 - \omega r)v_1 = \frac{p_2}{\rho} + U u_2 + (V_2 - \omega r)v_2$$
$$+ U L_R u_1 + U^2 sec^2\beta_1 \frac{L_R'}{2}\Delta\beta_1 \tag{2.19}$$

It should be noted that the linear loss representation does not alter the mean total pressure downstream of the rotor.

(2)   The non-linear loss to be considered is shown schematically in figure 5. The loss over the normal operating range will be assumed to be zero. When the inlet angle exceeds a critical value, $\hat{\beta}_1$, the loss takes on the constant value $\hat{L}_R$.

The mean flow angle will be assumed to be less than the critical value so total pressure is conserved in the mean flow. For sufficiently large disturbances the inlet angles may exceed the critical value over a portion of the cascade.

If the losses extend over a fraction, ϵ , of the cascade centered about $\hat{y}$, L_R is given by

$$L_R = \hat{L}_R \qquad |y-\hat{y}| < \frac{\epsilon}{2}$$
$$= 0 \qquad |y-\hat{y}| > \frac{\epsilon}{2} \qquad (2.20)$$

which has the Fourier representation

$$L_R = \epsilon \hat{L}_R + \hat{L}_R \sum_{n=1}^{\infty} \frac{2}{n\pi} \sin n\pi\epsilon \cos n\left(y-\hat{y}\right)$$

$$(2.21)$$

$$= \epsilon \hat{L}_R + \mathcal{L}_R$$

Equation 2.21 has an average value. Since, by assumption, the perturbation components have zero mean value it is necessary to add the average loss to the Bernoulli equation describing the mean flow. Therefore, it is possible for a disturbance to alter the mean flow when the non-linear loss is considered. The mean flow will be related by,

$$P_1 + \frac{1}{2}\rho\left[U^2 + (V_1 - \omega r)^2\right] = P_2 + \frac{1}{2}\rho\left[U^2 + (V_2^2 - \omega r)^2\right]$$
$$+ \frac{1}{2}\rho U^2 \epsilon \hat{L}_R$$

The third matching condition is,

$$\frac{p_1}{\rho} + Uu_1 + (V_1 - \omega r)v_1 = \frac{p_2}{\rho} + Uu_2 + (V_2 - \omega r)v_2$$
$$+ \frac{1}{2}U^2\mathcal{L}_R$$

where $\mathcal{L}_R$ is given by equation 2.21.

The extent of the loss region is initially unknown but will be assumed to extend over the section of the cascade with incidence angles exceeding the critical value computed on the basis of zero loss. That is, the addition of the loss function, $\mathcal{L}_R$, will be assumed not to affect the extent of the loss region.

The linear loss would be known from compressor tests. This representation of loss would be the obvious choice to employ in the matching relations in order to be consistent with small disturbances and quasi-steady flow. However, for moderately large disturbances or when the mean operating point is near the stall limit the linear loss may be inadequate to describe stalling of several blades and more or less normal operation of the remaining blades. The non-linear loss representation would be more adequate to describe the possibility of stalling, and consequently large losses, in several blade channels with small losses elsewhere.

The matching conditions at the plane of the rotor may be written in terms of the $\mathcal{P}$, Θ and H variables. Using the definitions, equation 2.5, along with $\varphi = \dfrac{U}{\omega r}$ and $\Delta\beta = -\dfrac{cos^2\beta}{U^2}\left[\Theta + \dfrac{U u}{\varphi}\right]$:

linear loss and $\delta_R \neq 0$,

$$H_2 + \left(\frac{\cos\theta_1}{\cos\theta_2}\right)^2 \tan\theta_1 \Theta_1 + \left(\frac{\cos\theta_1}{\cos\theta_2}\right)^2 P_1 - \tan\theta_2 \Theta_2 - P_2 = \left(\frac{\cos\theta_1}{\cos\theta_2}\right)^2 H_1$$

$$\left[\delta_R \cos^2\beta_1 + \frac{\cos^2\theta_1 \tan\theta_1}{\varphi}\left(\cos^2\beta_2 - \delta_R \cos^2\beta_1\right)\right]\Theta_1 + \left[\frac{\cos^2\theta_1}{\varphi}\left(\cos^2\beta_2 - \delta_R \cos^2\beta_1\right)\right]P_1$$

$$-\cos^2\beta_2 \,\Theta_2 = \left[\frac{\cos^2\theta_1}{\varphi}\left(\cos^2\beta_2 - \delta_R \cos^2\beta_1\right)\right]H_1$$

$$\text{(2.22)}$$

$$H_2 + \left[\frac{1}{\varphi} - \frac{L_R'}{2} + \frac{\cos^2\theta_1 \tan\theta_1}{\varphi}\left(\tan\theta_2 - \tan\theta_1 + \frac{L_R'}{2} - \varphi L_R\right)\right]\Theta_1$$

$$+\left[\frac{\cos^2\theta_1}{\varphi}\left(\tan\theta_2 - \tan\theta_1 + \frac{L_R'}{2} - \varphi L_R\right)\right]P_1 - \frac{1}{\varphi}\Theta_2$$

$$= \left[1 + \frac{\cos^2\theta_1}{\varphi}\left(\tan\theta_2 - \tan\theta_1 + \frac{L_R'}{2} - \varphi L_R\right)\right]H_1$$

non-linear loss and $\delta_R = 0$,

$$H_2 + \left(\frac{\cos\theta_1}{\cos\theta_2}\right)^2 \tan\theta_1 \Theta_1 + \left(\frac{\cos\theta_1}{\cos\theta_2}\right)^2 P_1 - \tan\theta_2 \Theta_2 - P_2 = \left(\frac{\cos\theta_1}{\cos\theta_2}\right)^2 H_1$$

$$\frac{\cos^2\theta_1}{\varphi}\tan\theta_1 \Theta_1 + \frac{\cos^2\theta_1}{\varphi}P_1 - \Theta_2 = \frac{\cos^2\theta_1}{\varphi}H_1$$

$$\text{(2.23)}$$

$$H_2 + \left[\frac{1}{\varphi} + \frac{\cos^2\theta_1}{\varphi}\tan\theta_1\left(\tan\theta_2 - \tan\theta_1\right)\right]\Theta_1$$

$$+\left[\frac{\cos^2\theta_1}{\varphi}\left(\tan\theta_2 - \tan\theta_1\right)\right]P_1 - \frac{1}{\varphi}\Theta_2$$

$$= \left[1 + \frac{\cos^2\theta_1}{\varphi}\left(\tan\theta_2 - \tan\theta_1\right)\right]H_1 - \frac{1}{2}U^2\mathcal{L}_R$$

2:2.2 Stator Blade Row

The matching conditions across a stator are just a special case of the matching conditions across a rotor. The equality of the axial velocity is the same for a rotor and a stator. The remaining two equations for a stator may be obtained from the rotor matching equations by replacing β by θ, changing the subscripts R to S and letting $\omega = 0$.

In terms of the φ, θ and H variables the matching equations may be summarized as follows:

linear loss and $\delta_S \neq 0$,

$$H_2 + \left|\frac{\cos \theta_1}{\cos \theta_2}\right|^2 \tan \theta_1 \, \theta_1 + \left|\frac{\cos \theta_1}{\cos \theta_2}\right|^2 \varphi_1 - \tan \theta_2 \, \theta_2 - \varphi_2 = \left|\frac{\cos \theta_1}{\cos \theta_2}\right|^2 H_1$$

$$\delta_S \left|\frac{\cos \theta_1}{\cos \theta_2}\right|^2 \theta_1 - \theta_2 = 0 \qquad\qquad (2.24)$$

$$H_2 + \left[\frac{L'_S}{2} + \cos^2 \theta_1 \tan \theta_1 \, L_S\right] \theta_1 - \left[\cos^2 \theta_1 \, L_S\right] \varphi_1 = \left[1 - \cos^2 \theta_1 \, L_S\right] H_1$$

non-linear loss and $\delta_S = 0$,

$$H_2 + \left|\frac{\cos \theta_1}{\cos \theta_2}\right|^2 \tan \theta_1 \, \theta_1 + \left|\frac{\cos \theta_1}{\cos \theta_2}\right|^2 \varphi_1 - \tan \theta_2 \, \theta_2 - \varphi_2 = \left|\frac{\cos \theta_1}{\cos \theta_2}\right|^2 H_1$$

$$\theta_2 = 0 \qquad\qquad (2.25)$$

$$H_2 = H_1 - \frac{1}{2} U^2 \mathcal{L}_S$$

2:3 Complete Solution for Particular Configurations

2:3.1 Isolated Rotor

Figure 1 illustrates the problem to be solved. The rotor is replaced by an actuator line at $X = 0$. The mean flow is described by

U, V_1 and P_1 upstream and U, V_2 and P_2 downstream of the blade row.

The input disturbance H_1 is assumed known and the general solutions for the unknowns are given by equations 2.8 to 2.13.

Assume the matching conditions are given by equations 2.23 which are rewritten below.

$$H_2 + k_6 \theta_1 + k_7 P_1 - k_8 \theta_2 = (1+k_7)H_1 - \frac{1}{2}U^2 \mathcal{L}_R$$

$$H_2 + k_1 \theta_1 + k_2 P_1 - k_3 \theta_2 - P_2 = k_2 H_1 \qquad (2.26)$$

$$k_4 \theta_1 + k_5 P_1 - \theta_2 = k_5 H_1$$

with

$$k_1 = k_2 \tan \theta_1$$

$$k_2 = \left(\frac{\cos \theta_1}{\cos \theta_2}\right)^2$$

$$k_3 = \tan \theta_2$$

$$k_4 = k_5 \tan \theta_1 \qquad (2.27)$$

$$k_5 = \frac{\cos^2 \theta_1}{\varphi}$$

$$k_6 = k_8 + k_7 \tan \theta_1$$

$$k_7 = k_5 (\tan \theta_2 - \tan \theta_1)$$

$$k_8 = \frac{1}{\varphi}$$

The three matching equations and their conjugates define the solution which in matrix form is,

$$
\begin{bmatrix}
1 & 0 & k_6 & k_7 & -k_8 & 0 \\
0 & 1 & k_7 & -k_6 & 0 & -k_8 \\
1 & 0 & k_1 & k_2 & -k_3 & -1 \\
0 & 1 & k_2 & -k_1 & 1 & -k_3 \\
0 & 0 & k_4 & k_5 & -1 & 0 \\
0 & 0 & k_5 & -k_4 & 0 & -1
\end{bmatrix}
\begin{Bmatrix}
H_2 \\
H_2^* \\
\Theta_1 \\
\mathscr{P}_1 \\
\Theta_2 \\
\mathscr{P}_2
\end{Bmatrix}
=
\begin{Bmatrix}
(1+k_7)H_1 - \frac{1}{2}U^2\mathscr{L}_R \\
(1+k_7)H_1^* - \frac{1}{2}U^2\mathscr{L}_R^* \\
k_2 H_1 \\
k_2 H_1^* \\
k_5 H_1 \\
k_5 H_1^*
\end{Bmatrix}
\qquad (2.28)
$$

The coefficient matrix may be simplified and it's inverse found. The inverted equation is,

$$
\begin{Bmatrix}
H_2 \\
H_2^* \\
\Theta_1 \\
\mathscr{P}_1 \\
\Theta_2 \\
\mathscr{P}_2
\end{Bmatrix}
=
\begin{bmatrix}
1 & 0 & k_{14} & -k_{15} & 0 & 0 \\
0 & 1 & k_{15} & k_{14} & 0 & 0 \\
0 & 0 & k_{16} & k_{17} & 0 & 0 \\
0 & 0 & k_{17} & -k_{16} & 0 & 0 \\
0 & 0 & k_{18} & -k_{19} & 1 & 0 \\
0 & 0 & k_{19} & k_{18} & 0 & 1
\end{bmatrix}
\begin{bmatrix}
(1+k_{10})H_1 - \frac{1}{2}U^2\mathscr{L}_R \\
(1+k_{10})H_1^* - \frac{1}{2}U^2\mathscr{L}_R^* \\
-k_{13}H_1 - k_5 H_1^* + \frac{1}{2}U^2\mathscr{L}_R \\
k_5 H_1 - k_{13}H_1^* + \frac{1}{2}U^2\mathscr{L}_R^* \\
-k_5 H_1 \\
-k_5 H_1^*
\end{bmatrix}
\qquad (2.29)
$$

The additional constants are:

$$k_9 = k_6 - k_4 k_8$$

$$k_{10} = k_7 - k_5 k_8$$

$$k_{11} = k_1 - k_6 - k_5 + k_4 \left(k_8 - k_3 \right)$$

$$k_{12} = k_2 - k_7 + k_4 + k_5 \left(k_8 - k_3 \right)$$

$$k_{13} = 1 + k_7 - k_2 - k_5 \left(k_8 - k_3 \right)$$

$$k_{14} = - \frac{k_9 k_{11} + k_{10} k_{12}}{k_{11}^2 + k_{12}^2}$$

$$k_{15} = \frac{k_9 k_{12} - k_{10} k_{11}}{k_{11}^2 + k_{12}^2}$$

$$k_{16} = \frac{k_{11}}{k_{11}^2 + k_{12}^2}$$

$$k_{17} = \frac{k_{12}}{k_{11}^2 + k_{12}^2}$$

$$k_{18} = \frac{k_4 k_{11} + k_5 k_{12}}{k_{11}^2 + k_{12}^2}$$

$$k_{19} = - \frac{k_4 k_{12} - k_5 k_{11}}{k_{11}^2 + k_{12}^2}$$

$$(2.30)$$

The case for the linear loss may be set up similar to equations 2.26. The inverted matrix equation may then be written down directly by merely identifying the corresponding constants.

While this work was in progress Ehrich (11) published a paper on an analytical treatment of the asymmetric inlet flow problem. His approach differs from the development here in the method of obtaining the solution and the matching conditions. He assumed a constant leaving angle from the blade row and further assumed that losses could be neglected.

The final results will be left in matrix form. The algebraic expressions cannot be simplified greatly and the results will be

presumed to be obtained numerically *for* any given example.

The result for the total pressure, in the case of no losses, may be written as $H_2 = \gamma_1 H_1 + \gamma_2 H_1^*$. The γ's are constants and are functions of the mean flow parameters. For the case of the linear loss and the linear flow deviation the γ's would also be functions of δ_R, L_R and L_R'. The remaining results may be expressed in a similar fashion, for example, $\Theta_1 = \gamma_3 H_1 + \gamma_4 H_1^*$. The form of the answers has several immediate consequences:

(1) The coefficients, γ, are independent of the harmonic content of the inlet disturbance.

(2) The results are given at the plane of the blade row. The $\mathcal{P}$ and Θ functions decrease from the plane of the blade row with components of wave number n decreasing like $e^{-n|x|}$.

(3) If the inlet disturbance has but one wave length then the form of the total pressure profile is unchanged upon passing through the rotor. The result may be expressed as $H_2(x,y) = \sqrt{\gamma_1^2 + \gamma_2^2} \; H_1(x,y-\alpha)$. The α is a phase shift given by $\alpha = \tan^{-1}\frac{\gamma_2}{\gamma_1}$.

(4) If the inlet disturbance contains many wave lengths then the total pressure profile downstream of the rotor is distorted from its original form.

A closer examination of the expression for the total pressure will indicate the flow processes involved. In dimensionless form the total pressure $\psi_2 = \gamma_1 \psi_1 + \gamma_2 \psi_1^*$. For no losses and infinite solidity,

$$\gamma_1 = \left[1 - \frac{\cos^2 \theta_1}{\varphi} (\tan \theta_1 + \tan \beta_2) \right] - \left[k_{13} k_{14} + k_5 k_{15} \right] \quad (2.31)$$

A simple calculation for a single rotor shows that the ideal
pressure rise is

$$\overline{\psi_2} = \overline{\psi_1} + 2 - 2 \varphi (\tan \theta_1 + \tan \beta_2) \quad (2.32)$$

If the upstream is disturbed by $\overline{\psi_1} + \psi_1'$ (and $\varphi + \phi_1$) then the
perturbation terms satisfy

$$\psi_2' = \psi_1' - 2 (\tan \theta_1 + \tan \beta_2) \phi_1 \quad (2.33)$$
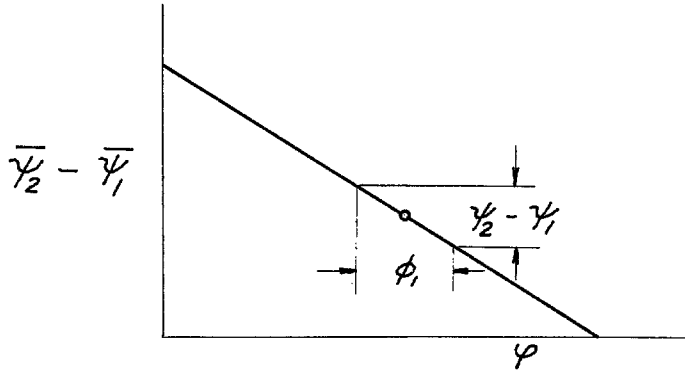
When the axial velocity is less than the mean (ϕ_1 is negative) the
total pressure rise is increased. This may be seen from equation 2.33,
the curve of $\overline{\psi_2} - \overline{\psi_1}$ vs φ or by examining the velocity diagrams
at the blade row, figure 6.

When pressure and angle perturbations are zero the flow
coefficient is given by $\phi_1 = \frac{\cos^2 \theta_1}{2 \varphi} \psi_1'$. Therefore, equation 2.33

becomes

$$\gamma_2 = \left[\, 1 - \frac{\cos^2 \theta_1}{\varphi} (\tan \theta_1 + \tan \beta_2) \right] \gamma_1 \tag{2.34}$$

Comparing equations 2.31 and 2.34 it is seen that the first bracketed term of γ_1 is due to the increased work addition by the rotor calculated only on the basis of the disturbance introduced far upstream.

The second bracketed term of γ_1 and the coefficient γ_2 are a result of pressure fields. When a non-uniform flow is turned through a cascade the flow upstream must adjust to the change which induces a pressure and angle perturbation field. The next section will illustrate the pressure field resulting from the turning of a non-uniform flow through a stator. There is another component of the pressure field in the case of a rotor which is similar to the pressure field resulting from the flow through a propeller.

Two effects may be attributed to the pressure field. First, the action of the pressure field is to accelerate the low velocity fluid and decelerate the high velocity fluid so that the amplitude of the velocity disturbance at the plane of the rotor is decreased with respect to the velocity disturbance far upstream. The second bracketed term of the coefficient γ_1 is, therefore, a correction term due to the reduced amplitude of the velocity disturbance. The second effect of the pressure field is to cause the streamlines to deviate and induce angles of attack at the rotor in such a manner that part of the fluid experiences

an increase in total pressure and another part a decrease. This latter effect accounts for the term $\gamma_2 \psi_1^*$ in the downstream total pressure expression and the distortion of the original total pressure profile.

In summary the total pressure change through a rotor is caused by different amounts of work being added to various regions of the fluid. There is first the direct effect which may be computed on the basis of the original inlet disturbance and the cascade characteristics (equation 2.34). There is also an indirect effect arising from the pressure field which results in a correction and the distortion of the original inlet disturbance.

The effect of the cascade characteristics may be seen in figure 7. The original disturbance is attenuated most for small turning through the blade row which corresponds to large values of β_2. The larger upstream whirl angles θ_1, also indicate the greatest attenuation. The coefficient γ_2 is an indication of the pressure field influence and it is seen to be the dominant term. The effect of varying the flow rate, φ, may be estimated by noting that a small value of φ corresponds to a large whirl angle θ_1, so attenuation is greatest for small φ. Figure 8 illustrates the effect of finite solidity. The coefficient γ_2 is the most sensitive to cascade solidity.

Figures 7 and 8 indicate that a rotor designed for zero work input to the mean flow is most effective for reducing disturbances. It has long been established that a free-wheeling rotor is a useful device to smooth out irregularities in wind tunnels, reference (12). Although the net work input by a free-wheeling device must be zero, there is

work added to low velocity fluid and work extracted from high velocity fluid.

2:3.2 Isolated Stator

The solution for the case of an isolated stator may be found by following the procedure used in the case of the isolated rotor.

For the case of no losses and infinite solidity the results at the plane of the stator are particularly simple.

$$
\begin{aligned}
H_2 &= H_1 \\
\mathcal{P}_2 &= 0 \\
\Theta_2 &= 0 \\
\mathcal{P}_1 &= (\cos^2\theta_1 - \cos^2\theta_2)(H_1 - \tan\theta_1 H_1^*) \\
\Theta_1 &= (\cos^2\theta_1 - \cos^2\theta_2)(\tan\theta_1 H_1 - H_1^*)
\end{aligned}
\tag{2.35}
$$

The pressure and angle perturbation fields are zero downstream of the stator due to the assumption of infinite solidity. There is a pressure and related angle perturbation field upstream except in the special example of $\theta_1 = -\theta_2$ in which case the flow is unperturbed everywhere.

2:3.3 Inlet Vanes-Rotor-Stator Configuration

2:3.3.1 Exact Solution

The three blade rows will be replaced by actuator lines where the rotor is at $X = 0$, the inlet vanes at $X = -X_V$ and the stator at $X = X_S$, figure 9. The mean flow is defined by U, V_1, P_1 with,

i	Region
0	$-\infty < x < -x_v$
1	$-x_v < x < 0$
2	$0 < x < x_s$
3	$x_s < x < \infty$

and $V_0 = 0$.

The equations governing the flow are:

$$\nabla^2 \Theta_i = 0$$

$$\mathcal{P}_i(x,y) = \frac{1}{2\pi} \int_{-\pi}^{\pi} \Theta_i(x,\eta) \cot\left(\frac{y-\eta}{2}\right) d\eta$$

$$\left(U\frac{\partial}{\partial x} + V_i \frac{\partial}{\partial y}\right) H_i = 0$$

The boundary conditions are:

$$\Theta_0(-\infty, y) = \mathcal{P}_0(-\infty, y) = 0$$

$$\Theta_3(\infty, y) = \mathcal{P}_3(\infty, y) = 0$$

$$f_n(x,y) = f_n(x, y + 2\pi)$$

The input disturbance is given by an expression similar to equation 2.8 and the upstream functions by equations 2.9 and 2.10. Downstream of the stator the functions are similar to equations 2.11 to 2.13. The potential functions between the blade rows required both

the positive and negative exponentials.

There are three matching conditions at each blade row which define six algebraic equations. In all there are 18 equations which must be solved simultaneously for the unknowns. Since the functions must be matched at different axial locations the coefficients of the unknown functions depend upon the axial spacing. In addition each wave number, n, has an exponential behavior, $e^{\pm nX}$, so that the unknown coefficients also depend on the harmonic content of the input disturbance. Therefore, the set of 18 equations must be solved for each wave length present.

2.3.3.2 Zero Axial Gap Approximation

The exact solution for the inlet vane-rotor-stator configuration may be drastically simplified by assuming zero axial gap between the blade rows. The three blade rows may then be reduced to actuator lines at the plane $X = 0$ keeping in mind that a finite chord only introduces a phase shift which may be ignored.

Since the analysis is restricted to long wave lengths any variation of the potential functions between the normally small blade gaps will be small. The zero axial gap approximation assumes no variation occurs in the space between blade rows.

The differential equations are valid in the regions denoted by the subscripts 0 and 3 . The matching conditions are combined algebraically to give the relations between the upstream and downstream regions.

For the case of zero losses and infinite solidity the results are especially simple. At the plane $X = 0$ the results are:

$$H_1 = H_0$$

$$H_3 = H_2$$

$$H_3 = \left[\cfrac{1}{1 + \cfrac{\cos^2\theta_3}{\varphi}(\tan\theta_1 + \tan\beta_2)} \right] H_0$$

$$\Theta_0 = H_0^* - \cos^2\theta_3 \, H_3^*$$

$$\mathcal{P}_0 = H_0 - \cos^2\theta_3 \, H_3$$

$$\Theta_1 = 0$$

$$\mathcal{P}_1 = 0$$

$$\Theta_2 = - \frac{\cos^2\theta_3}{\varphi} H_3$$

$$\mathcal{P}_2 = \left[1 - \cos^2\theta_3 \left(1 - \frac{\tan\theta_2}{\varphi} + \tan^2\theta_2 \right) \right] H_3$$

$$\Theta_3 = 0$$

$$\mathcal{P}_3 = 0$$

(2.36)

The downstream total pressure, H_3 , is a fraction of the input disturbance, H_0 . There is no distortion of the total pressure profile due to the assumption of infinite solidity cascades. For a given cascade geometry the attenuation of the disturbance is a function of φ and the attenuation varies between 0 and 1 for a variation of φ between 0 and ∞ .

Figures 10 and 11 illustrate the effects of the cascade geometry on the attenuation of the input disturbance. As in the case of the isolated rotor, the attenuation is greatest for lightly loaded blades. A

reduced solidity increases the distortion of the total pressure profile which is in contrast to the isolated rotor case.

2:3.3.3 Interference of Neighboring Blade Rows

The case of an isolated blade row requires the solution of a 6×6 matrix equation. The case of the inlet vanes-rotor-stator configuration requires the solution of an 18×18 matrix equation. In general if there are m blade rows the exact solution involves $6m$ algebraic equations. For multiple blade rows the algebraic equations must be solved for each wave length contained in the input total pressure profile. The approximation of zero axial gap between blade rows is certainly reasonable for two or even three blade rows but the extension of this assumption to a greater number of stages becomes less reasonable. Because of the great amount of algebra involved in multiple blade row solutions, it is obvious that an approximate method of solution would be advantageous. A simple iterative procedure may be used which is best illustrated by an example.

Assume a rotor-stator configuration. The blade rows are to be replaced by actuator lines. Let the rotor be at $X = 0$ and the stator at $X = X_s$. Let the subscripts 1, 2, 3 denote the regions upstream of the rotor, between the rotor and stator and downstream of the stator, respectively.

The procedure is as follows:

a) Solve the case of the isolated rotor at $X=0$ and obtain the solutions

$$H_2^{(iR)} , \mathscr{P}_1^{(iR)} , \Theta_1^{(iR)} , \mathscr{P}_2^{(iR)} , \Theta_2^{(iR)} ,$$

in terms of the input $H_1^{(iR)}$.

b) Solve the case of the isolated stator at $X = 0$ with the input $H_2^{(iS)} = H_2^{(iR)}$. Obtain the solutions,

$$H_3^{(iS)} \,, \; P_2^{(iS)} \,, \; \Theta_2^{(iS)} \,, \; P_3^{(iS)} \,, \; \Theta_3^{(iS)}$$

c) To find the solution near the plane of the rotor assume that the rotor is at $X = 0$ and the stator is superposed at $X = X_s$. The effect of superposing the isolated stator solution onto the isolated rotor solution is to perturb the pressure and angle deviation fields. Therefore, at the plane of the rotor the superposed solution, which may be considered the zeroth order solution, is:

$$H_1^{(o)} = H_1^{(iR)}$$

$$H_2^{(o)} = H_2^{(iR)}$$

$$P_1^{(o)} = P_1^{(iR)} + P_2^{(iS)}(X - X_s, y - y_s)$$

$$\Theta_1^{(o)} = \Theta_1^{(iR)} + \Theta_2^{(iS)}(X - X_s, y - y_s)$$

$$P_2^{(o)} = P_2^{(iR)} + P_2^{(iS)}(X - X_s, y - y_s)$$

$$\Theta_2^{(o)} = \Theta_2^{(iR)} + \Theta_2^{(iS)}(X - X_s, y - y_s)$$

d) Since the pressure and angle fields of the superposed stator disrupts the solution of the isolated rotor, the matching conditions for the rotor are no longer satisfied. In order for the matching conditions to be satisfied a correction term

must be added to the zeroth order solution which then gives the first order solution.

$$H_1^{(1)} = H_1^{(0)} = H_1^{(iR)}$$

$$H_2^{(1)} = H_2^{(0)} + H_2^{(c)} = H_2^{(iR)} + H_2^{(c)}$$

$$P_1^{(1)} = P_1^{(0)} + P_1^{(c)} = P_1^{(iR)} + P_2^{(iS)}(x-x_s, y-y_s) + P_1^{(c)}$$

$$etc.$$

The correction terms are found by substituting the first order terms into the matching conditions. Since $P_2^{(iR)}$, $P_3^{(iR)}$, etc. satisfy the matching conditions, the correction terms are found in terms of $P_2^{(iS)}(x-x_s, y-y_s)$ and $\Theta_2^{(iS)}(x-x_s, y-y_s)$.

e) To find the solution near the stator the pressure field $P_2^{(iR)}$ and angle deviation field $\Theta_2^{(iR)}$ are superposed on the isolated stator solution and a procedure similar to steps (c) and (d) is followed. However, in this case the input total pressure is now the first order solution $\left(H_2^{(0)} = H_2^{(iR)} + H_2^{(c)} \right)$ from step (d).

In step (c) the term $P_2^{(iS)}(x-x_s, y-y_s)$ includes the exponential decay of the harmonic function, $x-x_s$, and also a phase shift, $y-y_s$, which is necessary since the input profile is transported along the direction of the mean streamline and is, therefore, a function of the axial spacing between blade rows.

Figure 12 shows a graphical representation of the iterative procedure which illustrates the method.

The second order solution for the rotor can be obtained by adding the first order correction pressure from the stator solution and repeating step (d). Any number of iterations can then be performed. The successive iterations are not difficult since the original coefficient matrix is found only once and if put in the form of equation 2.29 the correction terms may be computed directly.

It was not explicitly stated in the development of the iterative procedure but only one wave length was assumed for the input disturbance. The extension of the procedure to many wave lengths requires that the order of magnitude of each added term be considered. For example the pressure field upstream of the rotor is

$$\mathscr{P}_1 = \mathscr{P}_1^{(iR)} + \mathscr{P}_1^{(C_1)} + \mathscr{P}_1^{(C_2)} + \mathscr{P}_1^{(C_3)} + \cdots$$

where $\mathscr{P}_1^{(C_{n+1})} < \mathscr{P}_1^{(C_n)}$. $\mathscr{P}_1^{(iR)}$ will have all wave lengths present in the initial disturbance. $\mathscr{P}_1^{(C_1)}$ will have an exponential term e^{-X_s} so only the wave length $n = 1$ is superposed onto the isolated case. $\mathscr{P}_1^{(C_2)}$ will have exponential term e^{-2X_s} so the wave length $n = 2$ is superposed as well as the correction term from the first order term. It then follows that the first order solution accounts for the interference of the immediately adjacent blade rows and the second order term adds the interference correction of the blade rows displaced by a distance $2X_s$, and so on.

2:4 Overall Performance

The overall performance of a compressor is characterized by the total pressure coefficient, $\mathscr{Y}$, the work coefficient, $\mathscr{Y}'$, and the

flow coefficient, Φ . The efficiency of the blade row is given by

$$\eta = \frac{\Psi}{\Psi'} .$$

It has been shown that the mean total pressure coefficient is changed by an inlet distortion only when it is assumed that the losses through the blade rows are represented by the non-linear type. By assumption Φ is unchanged with an inlet distortion. The work coefficient will, however, be changed by an inlet distortion since it has been demonstrated that the blade row will add different amounts of work to the various regions of the disturbed inlet flow.

For a single rotor Ψ' is given by,

$$\Psi' = \frac{\displaystyle\int_0^{2\pi}\int_{r_h}^{r_t} \rho \omega r \left(v_2' - v_1' \right) u_1' r \, dr \, dy}{\displaystyle\int_0^{2\pi}\int_{r_h}^{r_t} \frac{1}{2} \rho \left(\omega r_t \right)^2 u_1' r \, dr \, dy} \tag{2.37}$$

Assuming an inlet distortion and no radial variation of u and v (unit hub-tip ratio) the work coefficient is,

$$\Psi' = \overline{\psi'} + \psi' \tag{2.38}$$

where $\overline{\psi'}$ is the mean value and ψ' a perturbation due to the distorted inlet flow.

$$\psi' = \frac{1}{\pi r \omega U} \int_0^{2\pi} (v_2 - v_1) u_1 \, dy \tag{2.39}$$

The subscripts 1 and 2 refer to planes immediately upstream and down-stream of the rotor.

The integrand of equation 2. 39 is the product of two first order quantities so ψ' is of second order and the work coefficient is only changed by a second order quantity.

The fractional change of the efficiency $\dfrac{\Delta \eta}{\eta} = \dfrac{\Delta \psi}{\psi} - \dfrac{\Delta \psi'}{\psi'}$ can differ by a first order quantity since $\Delta \psi$ will be of first order if the non-linear loss is assumed.

2:5 Blade Forces

The fluid forces on a blade may be resolved into a force parallel and a force perpendicular to the plane of the blade row. The force parallel to the blade row is,

$$ F_y' = \rho s\, u' \left(v_1' - v_2' \right) $$

and the force perpendicular to the blade row is,

$$ F_x' = s \left(p_1' - p_2' \right) $$

When the inlet flow has a distortion the forces are composed of a mean value plus a variable component. For a rotor the additional force terms will be periodic with the wheel speed ω .

The additional force components are given by,

$$ \frac{F_x}{\rho s} = \mathcal{P}_1 - \mathcal{P}_2 \tag{2.40} $$

$$ \frac{F_y}{\rho s} = \Theta_1 - \Theta_2 + 2\cos^2\theta_1 \left(\tan\theta_1 - \tan\theta_2 \right)\left(H_1 - \mathcal{P}_1 - \tan\theta_1\, \Theta_1 \right) \tag{2.41} $$

where the subscripts 1 and 2 refer to locations immediately upstream and downstream of the blade row.

2:6 Example Results

2:6.1 Isolated Rotor

The solution for the isolated rotor was discussed in section 2:3.1. The solution was given in terms of the initial disturbance H_1 and its conjugate H_1^*. For a single wave length the disturbance profile is not changed but for a complex input the profile is changed by the addition of the conjugate function H_1^*. In this section an example case will be computed in order to demonstrate the results with a complex inlet distortion.

The input will be assumed to be a rectangular depression of the upstream total pressure. The reason for this particular input is two-fold. First, the experiments to be discussed in a later section have as their inputs a distortion closely approximated by a rectangular depression. Second, a simple analytical expression representing the input is known which has the extremely convenient property that the exponential behavior of all the harmonics may be calculated in one step.

Consider the function,

$$F = \ln \left[\frac{\sinh \frac{1}{2}(x + iy - i\alpha\pi)}{\sinh \frac{1}{2}(x + iy + i\alpha\pi)} \right]$$

By a straight forward calculation the function F can be shown to have the properties that

$$\mathcal{Rl}\, F = -\sum_{n=1}^{\infty} \frac{2\sin n\pi\alpha}{n} \sin ny\, e^{\pm nx} \quad , \quad x \lessgtr 0$$

$$\mathcal{Im}\, F = \pm \left[\alpha\pi + \sum_{n=1}^{\infty} \frac{2\sin n\pi\alpha}{n} \cos ny\, e^{\pm nx} \right] \quad , \quad x \lessgtr 0$$

where $\mathcal{R}\ell$ and $\mathcal{I}m$ refer to the real and imaginary parts.

The functions have the following wave forms:
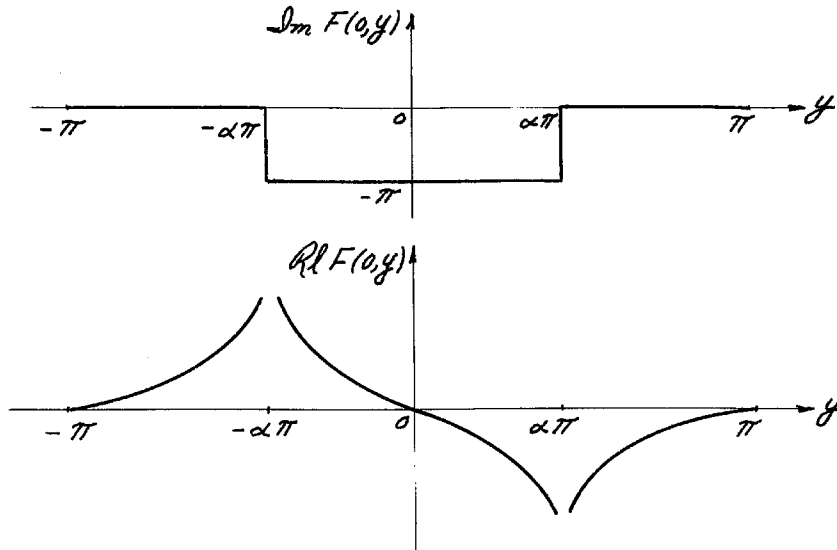
The function $\mathcal{R}\ell \, F(0,y)$ has logarithmic singularities at $x = \pm \alpha \pi$.

The input at $x = 0$ is given by,

$$H_1(0,y) = -\frac{1}{\pi} \left[\mathcal{I}m \; F(0,y) - \alpha \pi \right]$$

and the conjugate function H_1^* is

$$H_1^*(0,y) = \frac{1}{\pi} \left[\mathcal{R}\ell \, F(0,y) \right]$$

Since H_1 contains all wave lengths the assumption of quasi-steady flow is not strictly satisfied but this fact as well as the fact that the results contain singularities at the edges of the rectangular depression will be ignored.

Assume the mean flow parameters are:

$$\varphi = \frac{1}{2}$$
$$\theta_1 = 20°$$
$$\theta_2 = 45°$$
$$U = 1$$

Also assume no losses and infinite solidity.

Figure 13 illustrates the total pressure profiles in relation to the rotor blade row and the mean flow parameters. The magnitude of the depression is taken as unity and covers a 90° sector. The total pressure profile is grossly distorted upon passing through the rotor which indicates that the pressure and angle deviation fields account for the majority of the change.

Figure 14 shows the axial velocity profiles far upstream of the blade row ($X = -\infty$), at the plane of the rotor ($X = 0$) and far downstream ($X = \infty$). The profile far upstream is the same form as the input total pressure since the flow there is undisturbed so that the axial velocity is directly proportional to the total pressure. At the plane of the rotor the low velocity region has been accelerated and the high velocity region decelerated; in addition the pressure field has distorted the shape of the original pattern. Far downstream the profile of the axial velocity is similar to the downstream total pressure since the static pressure field has become zero and the axial velocity is again directly proportional to the total pressure.

The change of the axial velocity profile at several locations upstream of the rotor is shown in figure 15. Not much change occurs for $-\infty < X < -2$, however, there is considerable change between $-2 < X < 0$ due to the pressure field. The velocities at the edges of the wake undergo a drastic transformation between $X = -.125$ and the plane of the rotor which will presently be seen to cause a rapid contraction of the wake region near the blade row. Downstream of the

rotor the axial velocity profiles, figure 16, show a much smoother

transition to the final form at the downstream infinity.

Figure 17 shows the form of the absolute flow angles at the

plane of the rotor. The angles upstream are almost entirely anti-

symmetric about $y = 0$ so the relative angles of attack are also anti-

symmetric. Since the relative leaving angle, β_2 , is constant by

assumption, the relative angles upstream of the rotor account for the

antisymmetric form of the total pressure profile. A positive value of

θ_1 indicates a reduced relative angle of attack. Note that the profile

of θ_2 is the negative of the profile of $\phi_1(0,y)$ which is the result of

assuming a constant relative leaving angle.

Figure 18 illustrates the form of the blade force components, F_x

and F_y .

The first order analysis assumes that the total pressure is

transported along the mean streamlines. A second order analysis

would correct the solution to account for the deviation of the stream-

lines. In essence the results of the first order analysis define the

corrected streamlines which may be found from a knowledge of u and

v , or $\Delta\theta$ everywhere in the flow field. Figure 19 shows the

streamlines for a value of $y_1 = \frac{1}{4}$. These streamlines were found

graphically by first plotting the streamline directions at various values

of x and then tracing the streamline paths. The perturbation angles

$\Delta\theta_1(-1,y)$ and $\Delta\theta_2(1,y)$ change the streamline direction by at most

one degree so the flow may be considered to be nearly uniform for

$|X| \gtrsim 1$. In fact an inspection of the figure shows that the greatest streamline change occurs in the interval $|X| < \frac{1}{4}$. The streamlines defining the edges of the rectangular depression first start out covering 90° then reduce to 78° at the plane of the rotor and finally reduce to 66° far downstream of the rotor. The total contraction is approximately 27 °/o. Half of the contraction occurs by the time the pattern reaches the plane of the rotor which is analogous to the contraction of the wake for simple propellor theory.

Figure 20 demonstrates the effect of including the linear loss. It can be seen that the function H_2 has more of its original form than it has when assuming no losses.

Figure 21 illustrates the effect of assuming the non-linear loss over a part of the circumference. In this case the losses have the greatest influence only over a part of the circumference (compare with figure 20) and additional distortions of the initial profile result.

For comparison some of the numerical results are given below:

no losses,

$$H_2 = -.210\, H_1 - .778\, H_1^*$$

$$\frac{F_x}{\rho s} = .743\, H_1 + .703\, H_1^*$$

$$\frac{F_y}{\rho s} = .605\, H_1 + .389\, H_1^*$$

with linear loss: $L_R = 0.25$, $L_R' = 1.0$,

$$H_2 = .145\, H_1 - .329\, H_1^*$$

$$\frac{F_x}{\rho s} = .484\, H_1 + .317\, H_1^*$$

$$\frac{F_y}{\rho s} = .396\, H_1 + .243\, H_1^*$$

The numerical results for the non-linear loss are the same as for the no loss case but with terms added to account for the extent of the loss region.

The addition of the linear loss has a suprisingly beneficial effect on the blade forces and the attenuation of the pressure field component of H_2 .

The numerical results for the overall performance may be tabulated.

	$\dfrac{\Delta \Psi'}{\Psi'}$	$\dfrac{\Delta \Psi}{\Psi}$	$\dfrac{\Delta \eta}{\eta}$
No Losses	$-.91$ °/o		$.91$ °/o
Linear Loss $\begin{bmatrix} L_R = 0.25 \\ L'_R = 1 \end{bmatrix}$	$-.89$ °/o		$.89$ °/o
Non-Linear Loss $\begin{bmatrix} \hat{L}_R = 1 \\ \epsilon = \frac{1}{6} \end{bmatrix}$	$-.20$ °/o	-6.55 °/o	-6.35 °/o

The performance is calculated on a basis of the input, $\Psi_1 = \frac{1}{4}$. In the case of the non-linear loss the value $\hat{L}_R$ corresponds to approximately 40 °/o of the mean total pressure rise and the losses apply to the region where the local angle of attack exceeds 4°.

The numerical results for the overall performance demonstrate that any change is of second order except when the non-linear loss is

assumed $\Delta \Psi$ and $\Delta \eta$ are of first order.

2:6.2 Inlet Vanes-Rotor-Stator Configuration

Numerical results for the case of an inlet vane-rotor-stator configuration with zero axial gap may be compared with the results for the isolated rotor. The mean flow parameters are assumed to be:

$$\varphi = \frac{1}{2}$$
$$\theta_0 = 0°$$
$$\theta_1 = 20°$$
$$\theta_2 = 45°$$
$$\theta_3 = 25°$$
$$U = 1$$

Assume no losses and infinite solidity. Then,

$$H_2 = .308 H_1$$

$$\frac{F_x}{\rho S} = -.308 H_1$$

$$\frac{F_y}{\rho S} = .184 H_1$$

Comparing these results with those for the isolated rotor with no loss, it is seen that the total pressure is attenuated less but the distortion of the input profile is not present. The direction of the X component of force is reversed and the magnitudes of the forces are considerably smaller for this particular configuration. The fractional change in the work coefficient, $\frac{\Delta \Psi'}{\Psi'} = .68$ °/o, is not significantly different from the isolated rotor case.

Allowing the blade rows to be displaced from one another by a small amount would not alter the results appreciably.

The effect of the blade row gap may be best illustrated by a numerical example. The flow parameters and other assumptions are

as above except that the input distortion is assumed to be a simple cosine wave and the blade gaps are equal. The results are for the total pressure downstream of the rotor in terms of the total pressure upstream,

$$H_2 = \gamma_1 \cos \psi + \gamma_2 \sin \psi$$

In addition to the exact results which were computed on a Datatron Digital Computer, the approximate results, computed by the iterative procedure outlined in section 2:3.3.3, are tabulated for comparison. In the tabulation of the results the superscripts iR, 1, 2, 3 refer to the solutions for an isolated rotor, first, second and third order corrections, respectively.

X_s	$\gamma_1^{(iR)}$	$\gamma_1^{(1)}$	$\gamma_1^{(2)}$	$\gamma_1^{(3)}$	γ_1 (exact)
2	.360	.304	.318	.322	.321
1	.080	-.021	.206	.168	.098
$\frac{1}{2}$	-.066	-.053	.542	.255	.230
$\frac{1}{4}$	-.139	-.003	.933	.320	.284
$\frac{1}{8}$	-.175	.041	1.223	.351	.302
0					.308

X_s	$\gamma_2^{(iR)}$	$\gamma_2^{(1)}$	$\gamma_2^{(2)}$	$\gamma_2^{(3)}$	γ_2 (exact)
2	-.721	-.747	-.713	-.715	-.715
1	-.802	-.665	-.520	-.585	-.676
$\frac{1}{2}$	-.803	-.522	-.293	-.394	-.342
$\frac{1}{4}$	-.794	-.460	-.144	-.162	-.184
$\frac{1}{8}$	-.787	-.430	-.054	.048	-.094
0					0

The magnitude of γ_1 does not vary greatly with the spacing but the change in γ_2, which is the pressure field effect, is appreciable.

The iterative solutions are, of course, much better for large spacing. For the spacing $X_s > 1$ the isolated rotor case may be used with not much error. Since the isolated rotor solution overestimates the pressure field effect, and consequently the blade forces, it would be a reasonable approximation. For $X_s < \frac{1}{8}$ the approximation of zero axial gap could be used. For $\frac{1}{8} < X_s < 1$ the two extreme assumptions of zero or infinite gap would not yield reasonable results and the exact solution or several iterations would have to be computed.

III. EXPERIMENTAL EQUIPMENT AND PROCEEDURE

3:1 Test Compressor and Instrumentation

The experiments were performed on an axial-flow compressor. Figure 22 is a cross section of the test installation and indicates the principle details of the compressor and associated ducting. The air enters through the bell mouth, flows through the straight duct section and then through the compressor proper. The air is exhausted vertically by turning the air leaving the compressor in the aft-duct section. Driving power is supplied by a dynamometer.

The compressor has an outer diameter of 36 inches and a hub-tip ratio of 0.6. The normal compliment of blades is a stage of inlet vanes to impart a prerotation to the fluid, three stages of rotor-stator combinations and finally two stages of exit vanes to recover the remaining whirl velocity. There are 30 blades per rotor row and 32 blades per stator row. The blades are removable so the compressor may be operated in a variety of configurations. Free vortex blades were used exclusively in the experiments and figure 23 shows the root and tip sections of these blades. The design operating point is $\psi' = 0.40$ at $\phi = 0.43$.

The flow rate is regulated by a throttle valve at the exhaust section. The throttle consists of motor driven doors which control the exit area and thereby provide a flow resistance which determines the operating point.

The performance of the compressor is determined by overall measurements and detailed flow surveys. The overall performance

is obtained by measurements of the rotational speed, flow rate, work input and exit-duct static pressure. There are survey ports for obtaining detailed pressure, angle and velocity measurements at any radial position upstream and downstream of each blade row.

The rotational speed of the machine is set by regulating the electrical power supplied to the dynamometer and the speed measured by a tachometer or a revolution counter in conjunction with a timer. The tachometer and revolution counter are electrically driven by a synchronous generator which is coupled to the dynamometer shaft. It is possible to set the speed to within $\frac{1}{2}$ RPM using these indicators.

The flow coefficient is correlated with the static pressure at the wall of the entrance duct. The duct is calibrated by means of velocity traverses across the duct area. The static pressure at the duct wall is averaged by four pressure taps and the pressure is measured by a precision water-micromanometer which can be read to an accuracy of .001 inch of water.

The work input is determined by a measurement of the reaction torque on the dynamometer at a given rotational speed. The torque is measured by a diagram type force meter which is loaded on one side by the reaction force and is balanced on the other side by air pressure. The balancing air pressure is connected to a mercury manometer and the height of the mercury column is calibrated in terms of torque. The calibration consists of statically loading the dynamometer with known weights on an accurate lever arm. The calibration is performed (with the dynamometer decoupled from the compressor) before and after a

test run and an average calibration used. During the testing auxillary motors rotate the outer races of the dynamometer roller bearings in a direction opposite to the compressor rotation which essentially eliminates the bearing friction.

The exit-duct static pressure is a rough indication of the compressor operation and is, therefore, a useful measurement.

Figure 24 shows the probe carriages and the pressure detecting unit used for detailed flow surveys. Figure 25 illustrates the test probes used. The probe carriage can position the probes radially and in the yaw direction. There are survey holes between each blade row and several survey holes about the circumference at each of the axial planes. The pressure from the test probes is detected by a Statham strain-gage pressure transducer. The strain-gage elements form one leg of a bridge circuit and the adjacent leg is a Brown self-balancing potentiometer and indicator. The indicator and bridge circuit is the large instrument to the side of the compressor in figure 24 and the pressure transducer is the small instrument mounted on top of the indicator. The indicator scale is initially calibrated against the precision water-micromanometer. This system is particularly advantageous since the strain-gage transducer requires a negligible volume flow from the probes and fluctuating pressures may be averaged fairly rapidly.

Further details of the compressor and equipment may be found in reference 13.

3:2 Inlet Disturbance and Test Procedure

The asymmetric inlet disturbance is introduced upstream of the compressor section by blocking a sector of the annulus with screens. The screens are mounted on a wire framework for support. Figure 26 illustrates the blockage screen and the axial location of the screen and framework assembly.

The extent of the area blocked and the magnitude of the disturbance may be varied easily by using different size and solidity screens. Most of the experimental work was performed with a blockage of approximately $\frac{1}{4}$ of the inlet area. Combinations of screens were used to adjust the magnitude of the disturbance. The screens had a uniform radial density so that the input distortion had only a circumferential distribution and no radial variation.

Since it was one of the primary purposes of the experiments to obtain detailed flow surveys some method of positioning the test probe in relation to the screen was needed. The method used was to keep the test probe fixed and rotate the screen. Figure 27 is a pictorial diagram of the screen positioning mechanism. The wooden inlet fairing is hollow and the remote selsyn and gears are mounted inside. The inlet fairing with the screen framework is rotated on an overhung shaft rigidly fixed to the compressor housing. The electrical wires for the remote selsyn are led out the centerline of the inlet duct and then to the positioning selsyn located at the operating desk. The rotation of the remote selsyn was geared so that a 9° rotation of the positioning selsyn moved the inlet fairing assembly by 1°. The selsyns ordinarily have

sufficient torque so auxillary drives are not necessary; however, when several screens were used a friction cable drive was employed to rotate the assembly and the selsyns were used as indicators. The cables were led out through holes in the duct to the operating desk. The electrical wires and the cables for the friction drive have a negligible effect on the normal flow through the duct and compressor. The screen may be positioned to within approximately $\frac{1}{4}°$.

The calibration of the flow rate with the duct static pressure was performed with the inlet disturbance installed. It was found that for a blockage covering up to $\frac{1}{3}$ of the inlet annulus the flow rate was independent of the magnitude of the disturbance and its circumferential position. This was due in part to the screens being introduced sufficiently far downstream of the plane of the pressure measurement and also in part due to the averaging of the wall pressure by the four pressure taps.

In all the tests the rotational speed of the machine was 750 RPM. The testing required extended periods of time and the speed was maintained within $\pm$ 2 RPM by repeated checks.

The overall measurements were obtained with the screen at any arbitrary position. The method of obtaining the detailed circumferential surveys was to locate the probe at a given radius and axial location and the screen turned to the desired circumferential position. After a measurement was taken the screen was rotated to the next circumferential position and another measurement taken. When the screen was rotated through $360°$ the probe was relocated at another

radius or axial location and the procedure repeated.

A circumferential survey requires an average of 75 measurements and when angle, velocity and total pressure surveys are required at several radii and between each blade row, the number of measurements quickly add up. Therefore, the rapid and accurate method of positioning the screen for the circumferential surveys as well as the use of the fast response pressure indicator may be appreciated.

IV. EXPERIMENTAL RESULTS

4:1 Presentation of Results

Detailed flow surveys were made about the entire circumference; however, the results are shown for only half of the circumference. The remaining area is not affected appreciably and the main features of the flow are retained in the curves. The flow patterns have been shifted by the circumferential displacement of a mean streamline path so that the center of the wakes appear at the same circumferential angle on the curves.

The results of the surveys are presented by lines drawn through the test points while the actual data points are omitted from the curves. Measurements were taken at 2° or even 1° intervals in the wake region where the flow changes rapidly and at 5° or 10° intervals outside of the wake where the profiles become relatively smooth. The total pressure measurements at the edges of the screen fluctuate considerably and the results represent an average of the maximum and minimum readings. Downstream of the rotor the pressure fluctuations are much smaller but cover a larger circumferential angle (approximately two blade spacings or 24°) at the edges of the wake.

Two single stage configurations were tested extensively and in addition several tests with the complete three stage configuration were made. The single stage configurations are termed an expanded single stage and a normal single stage and they are described in the following sections.

The blockage screens introduce a wake corresponding to a total pressure loss through which the blades of the rotor traverse. The edge of the loss wake the blades first encounter from the direction of undisturbed flow is termed the leading edge. The edge of the wake the blades pass through from the loss region to the undisturbed flow is termed the trailing edge.

The blockage screens are referred to as the No. 1, No. 2 or No. 3 screen and these indicate the magnitude of the disturbance they introduce at the entrance of the compressor. The No. 3 screen produces the largest total pressure loss. The No. 1 screen was one sheet of high solidity material and the larger disturbance screens were made by superposing additional sheets of the same material. The superposed screens were displaced circumferentially and wires stripped from the ends of the screens so the wake edges would not cause abrupt velocity or pressure changes in the flow.

4:2 Expanded Single Stage Configuration

The expanded single stage configuration consists of the inlet vanes, second rotor and third stator. Figure 28 shows the blockage screen, blade rows and survey planes approximately to scale; exact dimensions are given in Table I.

This particular configuration was chosen so that measurements at several planes upstream and downstream of the rotor could be made. Since this configuration approximates an isolated rotor the test results may be compared qualitatively with the example results of section 2:6.1.

Figure 29, 30 and 31 together comprise a complete flow survey at the mean radius, ξ = 0.8. The total pressure survey upstream of the inlet vanes (S_I) in figure 29 is considered the input disturbance. A comparison of the total pressure surveys upstream of the rotor (S_I and S_{IV}) indicate the contraction of the wake. Downstream of the rotor the two total pressure surveys (S_V and S_{VII}) appear to be dis-placed circumferentially which is a result of the wake contraction downstream of the rotor.

The flow angle survey upstream of the inlet vanes (S_I), figure 30, are disturbed due to the turning through the vanes and also due to the influence of the rotor. The rapid change in the angles upstream of the rotor (S_{II} and S_{IV}) occurs in less than six inches. The angles downstream of the rotor (S_V and S_{VII}) show the rapid decay of the perturbation fields.

The flow coefficients in figure 31 show the acceleration of the low velocity fluid (S_I and S_{IV}). The survey downstream of the rotor is the same form as the total pressure survey at the identical position which indicates that the static pressure perturbation is almost zero and this is further substantiated by the angle survey at the same plane.

A qualitative comparison of the wave forms of the test results may be made with the example results for the isolated rotor case. The flow angles measured at the survey planes upstream of the rotor (S_{IV}) and downstream of the rotor (S_V) compare favorably with the angles in figure 17. The flow coefficient surveys upstream of the rotor (S_I and S_{IV}) also have the features of the calculated profiles at $X = -\infty$

and $\chi = -.125$ in figure 15. The total pressure profile downstream of the rotor (S_v) does not seem to compare with the example profiles in figures 13, 20 or 21. The characteristic dip in the total pressure at the leading edge of the wake (40°) is present to a degree but the characteristic peak at the trailing edge of the wake (140°) appears to occur more toward the center of the wake area in the test results. This apparent discrepancy will be examined more fully later.

Figures 32, 33 and 34 are radial surveys which correspond to the results in figures 29, 30 and 31. Since the upstream angles in figure 33 and the upstream total pressure in figure 32 are similar the flow must be nearly two-dimensional. Downstream of the rotor the total pressures and angles indicate that three-dimensional effects are concentrated near the trailing edge of the wake region. In figure 34 the dip in the leaving angle at 100° for $\xi = 0.7$ corresponds to an increased velocity area which correlates with the peak in the total pressure survey, figure 32. Similarly the peak in the angles at 110° for $\xi = 0.8$ corresponds to the lower total pressure at the same point.

Radial surveys of the total pressure at two other flow rates are given in figures 35 and 36. There is more nearly two-dimensional flow downstream of the rotor at the higher flow rates which is due to the compressor operating nearer the design point. Also the losses through the blade row would be smaller at the higher flow rates.

A comparison of the total pressures at the three flow rates are given in figures 37, 38 and 39. Consider the curves for $\xi = 0.8$,

figure 38. The sharp dip at the trailing edge of the screen wake (130°) is seen to increase in width as the flow rate is lowered. The considerable variation of the flow angles from the design value at 130°, figure 33, induces large incidence angles at the rotor inlet which in turn must result in large losses. The incidence angles and consequently the losses would be greatest at the lower flow rates. It can be concluded that the dip in the total pressure curves at the trailing edge of the screen wake is a result of losses and the characteristic peak one would expect from the example results, figures 13, 20 or 21, has been cut off. As the flow rate is reduced the loss region increases from approximately 15° to 60° which is approximately 1 to 5 blade channels. The effect of losses is also apparent at ξ = 0.7 in figure 37 but to a lesser degree at ξ = 0.9 in figure 39.

4:3 Normal Single Stage Configuration

The normal single stage configuration, as the terminology implies, consists of the inlet vanes, rotor and stator in their usual positions. Figure 40 shows the blade row and survey planes.

Figures 41-43 comprise a complete survey at the mid-blade height, ξ = 0.8. In figure 41 the total pressure surveys upstream of the rotor (S_I and S_{II}) show some contraction of the wake which is less than occurred in the expanded stage. The total pressure downstream of the rotor (S_{III}) has two sharp dips near the center of the wake region and these are localized losses since the widths are approximately one blade spacing. There are additional losses through

the stator (compare S_{III} and S_{IV}) mainly at the trailing edge. The peaks at the center of the wakes downstream of the rotor do not coincide since there is greater turning of the fluid in the center of the wake than elsewhere.

The angles upstream of the vanes (S_I), figure 42, are more perturbed than in the expanded stage. However, the angles upstream of the rotor are considerably less disturbed for the normal stage than the expanded stage; compare the surveys at S_{IV} in figure 30 with S_{II} in figure 42. The high solidity of the inlet vanes and the small gap between the blades in the normal stage are responsible for the flow angles upstream of the normal stage rotor being more uniform.

The flow coefficient downstream of the stator (S_{IV}) is similar in form to the total pressure survey at the same plane which indicates the pressure is approximately uniform. This is verified by the leaving angles from the stator, figure 42, being approximately constant.

Comparing the surveys at ξ = 0.7 downstream of the rotor and stator, figures 44 and 45, show the large losses at the root section. The flow angles measured downstream of the stator, figure 47, also indicate considerable angle variation where the losses occur.

The losses and angle variation in the stator are a result of the mutual interference between blade rows. In the expanded single stage the blades are sufficiently displaced so that the rotor blade row may be considered an isolated cascade. Since the potential functions, $\mathcal{P}$ and Θ , decay exponentially from a cascade the disturbed angles decrease downstream of the rotor and at the plane of the stator are considerably

reduced in magnitude, figure 30. However, in the normal single stage
the proximity of the blade rows to one another do not allow the expo-
nential decay to progress significantly and the large angle disturbances
downstream of the rotor are approximately the same magnitude
immediately upstream of the stator. As a consequence stalling and
flow separation occur in the stator blades.

For completeness and as a basis of comparison complete
surveys at another flow rate, figures 48-51, and with two other blockage
screens, figures 52-55 and figures 56-59, are included.

The effect of the flow rate and blockage screens can be
determined from figures 60-63 which compare the total pressure
measurements downstream of the rotor and stator at the three radial
survey sections. The losses are most pronounced at the hub section
where the turning angle is largest and the possibility of flow separation
greatest.

4:4 Three Stage Configuration

Total pressure surveys with two inlet disturbances were
obtained in the complete three stage configuration, figures 64 and 65.
Both disturbances are diminished considerably behind the second rotor
and evidence of the smaller disturbance is hardly detectable behind the
third stage.

Since the inlet disturbances are large there must be stalling and
flow separation in at least the first stator row as was found in the case
of the normal single stage. However, regardless of any stator losses

tending to increase or maintain the magnitude of the flow distortion the inlet disturbance is rapidly attenuated through the three stages. These results indicate that in a multi-stage compressor the influence of an asymmetric inlet flow would be limited to the first few stages.

4:5 Wake Contraction

The contraction of the screen wake was measured by tracing streamline paths in the compressor. Stream tubes at the edges of the screen were heated and then followed downstream by means of a total temperature probe.

A coil of Nicrome wire heated by an AC current formed the heat source, figure 66. Just downstream of the probe a stream tube of approximately $\frac{1}{4}$ inch diameter was heated.

The total temperature probe, figure 66, has a small thermocouple sensing element. The EMF induced at the thermocouple was balanced by a reverse EMF in a balancing circuit. A galvanometer was used to determine when the voltages were nullified and the maximum deflection of the ammeter scale determined the center of the heated stream tube. Details of the thermocouples and balancing circuit may be found in reference 14.

Figure 67 shows the streamline paths as viewed in the direction of the flow. The streamlines originating at the counterclockwise edge of the screen are considerably overturned as compared with the streamlines originating at the clockwise edge of the screen. There is not much radial variation of the streamlines except downstream of the rotor at the

clockwise edge of the screen. The radial and circumferential shift of the streamlines are given in Table II.

Figure 68 is a two-dimensional view of one streamline path. The angle leaving the inlet vane is approximately 20° and is turned almost axial at the rotor inlet. The flow angles from figure 30 at the corresponding points are 17° and 2^O. It was not possible to measure further downstream than survey station $S_{V/}$ since the heated stream tube became too diffuse to detect.

The wake sector at the mid-blade height, $\xi = 0.8$, starts out being approximately 110° and contracts to 93° downstream of the rotor. The decrease is $15.4 ^O/o$ which compares favorably with the $13.5 ^O/o$ contraction of the 90° wake in the example results of section 2:6.1.

4:6 Overall Measurements

The work coefficient as a function of the flow coefficient was measured in the two single stage configurations. Results obtained with the No. 3 blockage screen installed at the inlet are compared with measurements with no inlet disturbance.

In the expanded single stage configuration, figure 69, the work coefficient is decreased with the blockage screen installed when $\varPhi \lesssim 0.36$. When the flow rate $\varPhi > 0.36$ the work coefficient with the blockage screen is only slightly increased above the value without the screen blockage. At $\varPhi = 0.40$ the work coefficient is approximately $3 ^O/o$ less with the No. 3 screen as compared to normal operation. The decrease in the work coefficient calculated in the example results,

section 2:6.1, is approximately 1 $^{\circ}$/o. The agreement is good consider-
ing the example results were computed assuming unit *hub-tip ratio*
which neglects the contributions from all radial sections.

The results for the normal stage, figure 70, indicate no deviation
in the work coefficients at the higher flow rates, at least within experi-
mental accuracy. At the lower flow rates the losses in the stages cause
the work coefficient measured with the blockage screen installed to
increase over the no disturbance values.

Downstream of the compressor stages the static pressure less
the atmospheric pressure, at a given flow rate, is a measure of the
total pressure rise. If the static pressure measurement is corrected
for the average total pressure at the inlet section the static pressure
measurement can be a useful indication of the total pressure rise when
a disturbance is introduced at the inlet.

Figure 71 shows the static pressure coefficient measurements
for no screen, No. 3 screen and the No. 3 screen corrected for the
entrance loss. The entrance loss was obtained from the detailed
surveys of the total pressure downstream of the screen for this con-
figuration. Three corrected points are shown on the curve which
correspond to the three detailed surveys at ϕ = 0.35, 0.40 and 0.45.
It was found that the loss could be expressed as a drag coefficient
multiplied by the square of the mean flow coefficient which allows the
corrected curve to be extended beyond the actual measured flow rates.
The difference between the corrected curve and the curve without the
screen may be considered the additional total pressure loss through

the compressor due to the inlet disturbance. For flow rates $\phi \gtrsim 0.45$ the additional losses are negligible but losses become important near the peaks of the curves.

Figure 72 shows the results with the No. 3 screen installed in the normal single stage. The additional losses in this configuration are larger than in the expanded stage which is due to the stator influence. Stator losses were evident in the detailed flow surveys, figures 60-63. Figure 73 shows the effect of stator losses with the smallest disturbance tested; compare with figure 72.

It will be recalled that the first order analysis with the linear loss representation implies no change of the mean flow. The figures 71, 72 and 73 indicate that there is a mean total pressure loss. Therefore, a non-linear loss representation or a second order analysis is required to predict the additional losses due to the inlet disturbance.

The inception of propagating stall was determined with and without the blockage screens installed at the inlet. It was initially supposed that the inlet distortion would have a significant effect on the flow rate where stall first occurs; however, the results were surprising in that no appreciable change was found. The results are tabulated below.

Compressor Configuration	Inlet Condition	Φ_{Stall}
Expanded Single Stage	No Screen	.313
	No. 3 Screen	.318
Normal Single Stage	No Screen	.311
	No. 1 Screen	.311
	No. 2 Screen	.312
	No. 3 Screen	.311
Three Stages	No Screen	.410
	No. 1 Screen	.418

The propagating stall referred to here is the large amplitude stall as defined in reference 15. The first occurrence of propagating stall in this compressor is the so-called partial stall which is confined to only a portion of the blade height. The results tabulated above are for the inception of this partial stall. The stall was detected by means of a hot-wire anemometer although the stall is distinctly audible and could be detected without hot-wire equipment.

The flow coefficient at the stall point is the average flow rate from the entrance duct static pressure. The inlet disturbance covered approximately a 90° sector so $\frac{1}{4}$ of the fluid was retarded and $\frac{3}{4}$ accelerated. Therefore, only $\frac{1}{4}$ of the fluid with a velocity less than the mean is conducive to stall while the remaining $\frac{3}{4}$ with higher velocity tends to impede the propagation of a stall patch. When the mean flow rate is reduced the magnitude of the disturbance decreases (see figure 37) and the velocity in $\frac{3}{4}$ of the annulus area is also reduced with respect to the mean velocity. At the low flow rates where stall occurs the high velocity fluid is not sufficiently large to impede

the stall patch from propagating. This explains why stall occurs at approximately the same mean flow rate with and without the blockage screens.

Turner, Richie and Moss (16) report in a recent paper that the stall limit was unchanged with the introduction of asymmetric inlet distortions covering 50 ^{o}/o and 75 ^{o}/o of the inlet area of a single stage compressor. Since their disturbances were introduced by screens the reason for no change in the inception of propagating stall must be as explained above.

At a flow rate approximately 10 ^{o}/o greater than the point of incipient stall it was observed that velocity fluctuations occurred near the tip section of the blades. The fluctuations were considerably larger than the background turbulence level but smaller in magnitude than propagating stall. In addition the fluctuations seemed periodic at certain circumferential positions, random at other positions and disappeared at still other positions. It was assumed that these fluctuations were the initiation of propagating stall. A representative hot-wire record of the velocity fluctuations is shown in figure 74. For comparison figure 75 shows a hot-wire record of the propagating stall. The recording level in each figure is constant and demonstrates the change in amplitude of the fluctuations about the circumference; however, no significance should be attributed to the relative amplitudes of the two figures.

From the detailed flow surveys it is known that the region of large incidence angles is at the trailing edge of the screen wake (105°)

and in the absolute coordinate system a stall patch would propagate in the direction of 0° to 360°. Referring to figure 74 the large amplitude pulses appear at 120°, are decreased in magnitude at 160° and decrease to zero at 240°. These results seem to verify that the large velocity fluctuations are the initiation of stall patches but do not fully develop due to their propagation into a high velocity region.

V. COMPARISON OF EXPERIMENT AND THEORY

A direct comparison of the experimental results with the theory for one case is shown in figures 76 and 77. The test results are for the expanded single stage configuration with the No. 3 screen, $\mathscr{P}$ = 0.45 and ξ = 0.8 .

The mean flow parameters were assumed to be the average of the circumferential surveys; these values were equal, within experimental accuracy, to measurements with a uniform inlet flow. The theoretical curves were calculated on the basis of an isolated rotor, section 2:3.1, with the linear deviation angle and the linear loss. The values defining the deviation angle and the linear loss were taken from reference 14.

The assumed input profile is shown in figure 76. The Fourier representation of the input only includes wave numbers up to 18 so details of the flow cannot be expected for a circumferential extent of less than 20° or approximately two channel widths.

Figure 76 is the comparison for the total pressure survey. Figure 77 is the comparison for the angles measured upstream and downstream of the rotor and the flow coefficient measured upstream of the rotor. Two theoretical curves are shown in each case; one for no loss or leaving angle variation and the other including the loss and leaving angle variation. Referring to the figures it can be seen that the theoretical comparison which includes the loss and angle variation is a much better representation. Any theory which neglects these factors, e.g. reference 11, would not be as satisfactory.

Consider the comparison of the experiments with the theory assuming losses and a leaving angle variation. One primary discrepancy is a result of the first order theory not accounting for the contraction of the screen wake. For example the peaks of the angles upstream of the rotor, θ_1 , do not coincide nor do the edges of the flow coefficient, ϕ_1 . The wake contraction should cause the flow within the wake region to accelerate which can be seen to occur in the circumferential region 120°-190°. The greater total pressure rise than predicted by the theory in the region 120°-180° may be justified somewhat by the acceleration of the fluid in the wake. Another discrepancy is the losses which are confined to approximately one blade channel at the circumferential angle of 220°, figure 76. The losses must be accompanied by flow separation and a partial blockage of that particular blade channel which would explain the larger leaving angles, θ_2 in figure 77, at that circumferential angle.

The losses assumed for the theoretical curves are based on the mean flow and are, therefore, small. The losses in the wake region are considerably larger since the incidence angles at the rotor inlet would be large. By assuming a greater value of the loss the theoretical curve could be made to agree more nearly with the experiments but at the sacrifice of introducing unknowns and further assumptions into the theory. The non-linear loss representation, as has been previously indicated, could account for large losses in the wake region and small losses elsewhere. However, two unknowns would be introduced which are the magnitude of the loss and the value of the critical angle.

The virtue of the linear loss, besides simplicity, is the availability of the required information from actual compressor tests.

The theoretical calculations are based on the isolated rotor case so the interference effects of the inlet vanes and stator have been neglected. The isolated rotor case has been seen to overestimate the term responsible for the distortion of the input profile, section 2:6.2. Therefore, the slope of the theoretical total pressure curve in the wake region would be decreased and made to agree more nearly with the experiments by accounting for the interference of the neighboring blade rows.

VI. CONCLUDING REMARKS

A total pressure disturbance at the inlet of a compressor stage is considerably reduced in magnitude and distorted from its original form downstream of the stage. The circumferential extent of the total pressure disturbance is also decreased downstream of the stage. The reduction of the disturbance is due to the unequal work added by the rotor to the various parts of the fluid. Pressure and flow angle perturbations which are induced upstream and downstream of the blade rows are responsible for the reduction of the circumferential extent of the disturbance.

The angle perturbations are a maximum at the plane of a blade row and decrease exponentially upstream and downstream. Large perturbed flow angles downstream of a rotor blade row can, therefore, cause stalling and flow separation in the following stator blade row when the axial spacing is small. If the stalling of the stator is severe the disturbance initially reduced by a preceding rotor could be increased sufficiently so that the magnitude downstream of the stator is greater than the original magnitude upstream of the rotor-stator combination.

In a multi-stage compressor an inlet disturbance is rapidly reduced through the stages. This reduction occurs regardless of the stalling and flow separation which must occur in at least the first stator. In the present investigation with a three stage compressor the largest disturbance tested was almost completely diminished downstream of the last stage. This tends to indicate that the asymmetric inlet disturbances would be limited to the first few stages of a multi-stage machine.

Ideally the average total pressure is unaffected by an inlet disturbance; however, losses which occur in the rotor and stator blade rows cause the average total pressure to be reduced. At the lower flow rates the losses are the greatest. The work coefficient was not affected appreciably by the disturbances employed in the tests. At the higher flow rates the work coefficient was slightly reduced in the expanded single stage and approximately the same in the normal single stage. When the flow rate was reduced below the point where stall occurs the work coefficient was increased somewhat over the no disturbance value in both single stage configurations. Since the work coefficient is roughly unaffected and the average total pressure is decreased with an inlet disturbance the efficiency is, therefore, reduced. The inception point of propagating stall was essentially unaffected by the inlet disturbances.

The linearized theory developed here correctly describes the flow process. The quantitative agreement for the wake contraction, section 4:5, and the work coefficient, section 4:6, may be considered reasonable under the assumptions of the linearized theory. There could be better agreement with the circumferential surveys and the additional losses occurring in the blade rows by extending the theory to a second order one.

It has been demonstrated that the additional blade forces are largest when losses and the leaving angle deviations are neglected. Therefore, a safe estimate of blade forces may be made with only a knowledge of the disturbance and the mean flow characteristics of the compressor.

REFERENCES

1. Conrad, E. W. and Sobolewski, A. E., "Investigation of Effects of Inlet-Air Velocity Distortion on Performance of Turbojet Engine," NACA RM E50G11, (1950).

2. Alford, J. S., "Inlet Duct-Engine Flow Compatability," Presented at the Fifth International Aeronautical Conference, Sherman M. Fairchild Publication Fund Preprint No. 566, (1955).

3. Rannie, W. D. and Marble, F. E., "Unsteady Flows in Axial Turbomachines," Communication Aux Journees Internationales de Sciences Aeronautiques, Paris, (1957).

4. Emmons, H. W., Pearson, C. E., and Grant, H. P., "Compressor Surge and Stall Propagation," Presented at the ASME Annual Meeting, New York, N. Y., Paper No. 53-A-56, (1953).

5. Stenning, A. H., "Stall Propagation in Cascades of Air-Foils," Journal of the Aeronautical Sciences, (1954), Vol. 21, p. 711.

6. Sears, W. R., "On Asymmetric Flow in an Axial-Flow Compressor Stage," Journal of Applied Mechanics, (1953), Vol. 20, p. 57.

7. Sears, W. R., "A Theory of 'Rotating Stall' in Axial-Flow Compressors," Graduate School of Aeronautical Engineering, Cornell University, Ithica, N. Y., prepared under Contract AF33 (038)-21406, U. S. Air Force, Office of Scientific Research, Air Research and Development Command, Baltimore, Maryland, (1953).

8. Marble, F. E., "Propagation of Stall in a Compressor Blade Row," Daniel and Florence Guggenheim Jet Propulsion Center, California Institute of Technology, Pasadena, California, Tech. Report No. 4, prepared under Contract AF18(600)-178, U. S. Air Force, Office of Scientific Research, Air Research and Development Command, (1954).

9. Falk, T. J., "Rotating Stall in Single-Stage Axial Flow Compressors," Graduate School of Aeronautical Engineering, Cornell University, Ithica, N. Y., prepared under Contract AF18(600)1523, U. S. Air Force, Office of Scientific Research, Air Research and Development Command, (1956).

10. Benenson, D. M., "Characteristics of Propagating Stall in Axial-Flow Compressors," PhD Thesis, California Institute of Technology, Pasadena, California, (1957).

11. Ehrick, F., "Circumferential Inlet Distortions in Axial Flow Turbomachinery," Journal of the Aeronautical Sciences, (1957), Vol. 24, No. 6, p. 413.

12. Collar, A. R., "The Use of a Freely Rotating Windmill to Improve the Flow in a Wind Tunnel," Aeronautical Research Council R. and M. No. 1866, (1938).

13. Bowen, J. T., Sabersky, R. H. and Rannie, W. D., "Theoretical and Experimental Investigation of Axial Flow Compressors," Mechanical Engineering Laboratory, California Institute of Technology, Pasadena, California, Prepared under Navy Contract N6-ORI-102, Task Order IV, (1949).

14. Alsworth, C. C., Iura, T., "Theoretical and Experimental Investigation of Axial Flow Compressors, Part 3, Progress Report on Loss Measurements in Vortex Blading," Mechanical Engineering Laboratory, California Institute of Technology, Pasadena, California, prepared under Navy Contract N6-ORI-102, Task Order IV, (1951).

15. Iura, T., Rannie, W. D., "Observations of Propagating Stall in Axial-Flow Compressors," Mechanical Engineering Laboratory, California Institute of Technology, Pasadena, California, prepared under Navy Contract N6-ORI-102, Task Order IV, Report No. 4, (1953).

16. Turner, R. C., Ritchie, J. and Moss, C. E., "The Effect of Inlet Circumferential Maldistribution on an Axial Compressor Stage," Aeronautical Research Council R. and M. No. 3066, (1958).

TABLE I.

Axial Location of Survey Planes and Blade Row

Plane	Axial Location (inches from reference)
Screen	47
S_I	39.750
S_{II}	35.500
S_{III}	32.313
S_{IV}	29.625
S_V	26.563
S_{VI}	23.875
S_{VII}	20.813
S_{VIII}	18.125
Inlet Vanes	37.250
No. 1 Rotor	34.250
No. 1 Stator	31.375
No. 2 Rotor	28.500
No. 2 Stator	25.625
No. 3 Rotor	22.750
No. 3 Stator	19.875

TABLE II.

Streamline Paths (See Fig. 67)

Survey Plane	Radius (inches)	Angular Displacement (Deg.)
	No Screen	
Heater Probe	12.7	
S_I	12.66	0
S_{III}	12.64	10
S_V	12.65	27
Heater Probe	14.4	
S_I	14.38	0
S_{III}	14.34	8
S_V	14.33	22
Heater Probe	16.2	
S_I	16.19	0
S_{III}	16.16	5
S_V	16.12	15
	Center of Screen	
Heater Probe	12.6	
S_I	12.48	0
S_{III}	12.46	9
S_V	12.51	25

TABLE II. (Continued)

Survey Plane	Radius (inches)	Angular Displacement (Deg.)
Heater Probe	14.4	
S_I	14.28	0
S_{III}	14.30	7
S_V	14.28	19
Heater Probe	16.2	
S_I	16.16	0
S_{III}	16.14	5
S_V	16.12	16
Counterclockwise Edge of Screen		
Heater Probe	12.6	
S_I	12.54	0
S_{III}	12.48	13
S_V	12.50	37
Heater Probe	14.4	
S_I	14.20	0
S_{III}	14.00	10
S_V	14.40	28
Heater Probe	16.2	
S_I	15.94	0
S_{III}	16.06	6
S_V	16.14	23

TABLE II. (Continued)

Survey Plane	Radius (inches)	Angular Displacement (Deg.)
	Clockwise Edge of Screen	
Heater Probe	12.6	
S_I	12.44	0
S_{III}	12.56	7
S_V	12.02	16
Heater Probe	14.4	
S_I	14.24	0
S_{II}	14.20	2
S_{III}	14.30	5
S_{IV}	14.30	5
S_V	13.40	11
S_{VI}	13.40	21
Heater Probe	16.2	
S_I	16.18	0
S_{III}	16.18	3
S_V	15.40	9
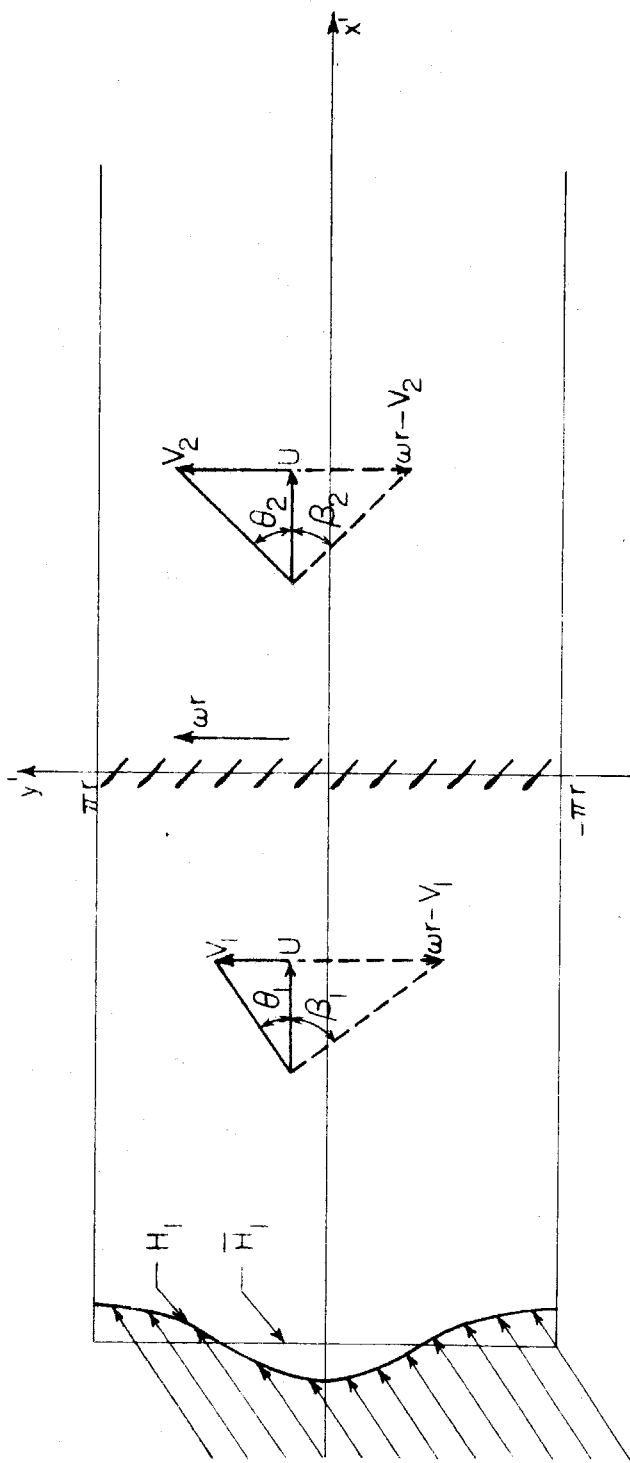
Fig. 1. Isolated Rotor Blade Row with an Inlet Distortion.
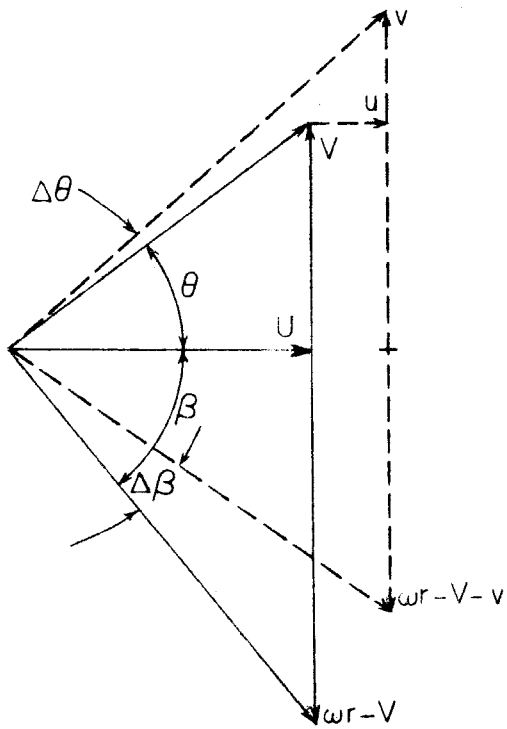
Fig. 2. Mean and Perturbation Fow Angles.
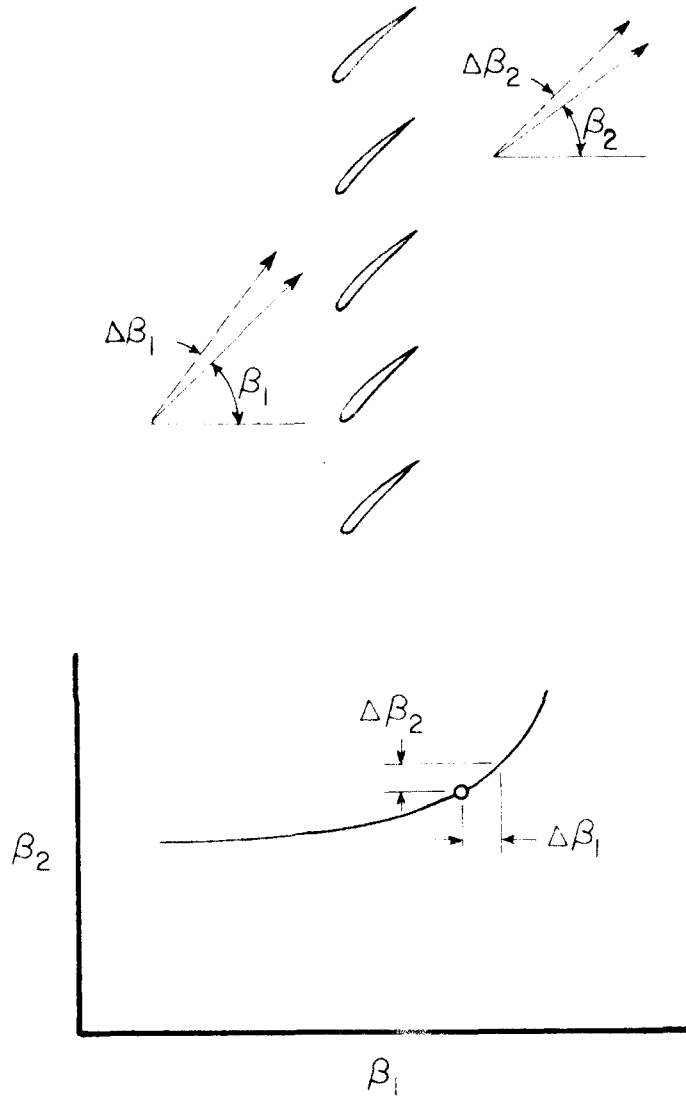
Fig. 3. Flow Angles at a Blade Row.
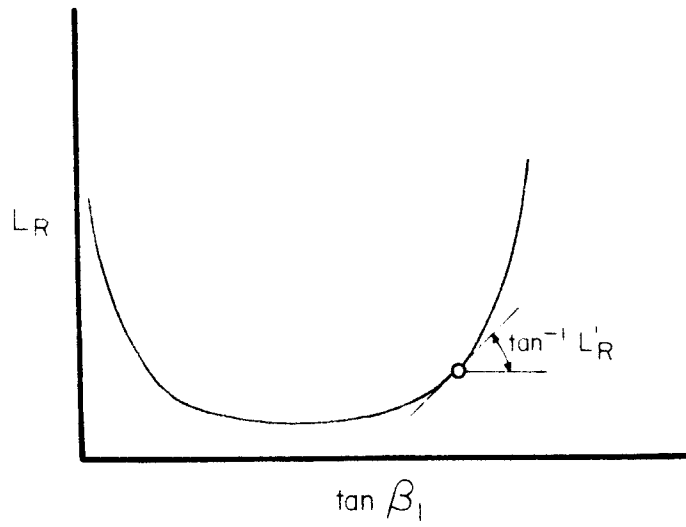
Fig. 4. Linear Loss Coefficient.
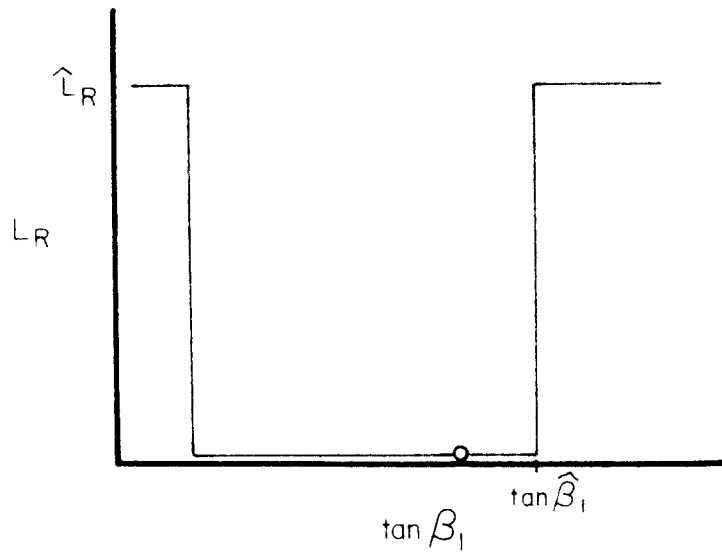
Fig. 5. Non-linear Loss Coefficient.
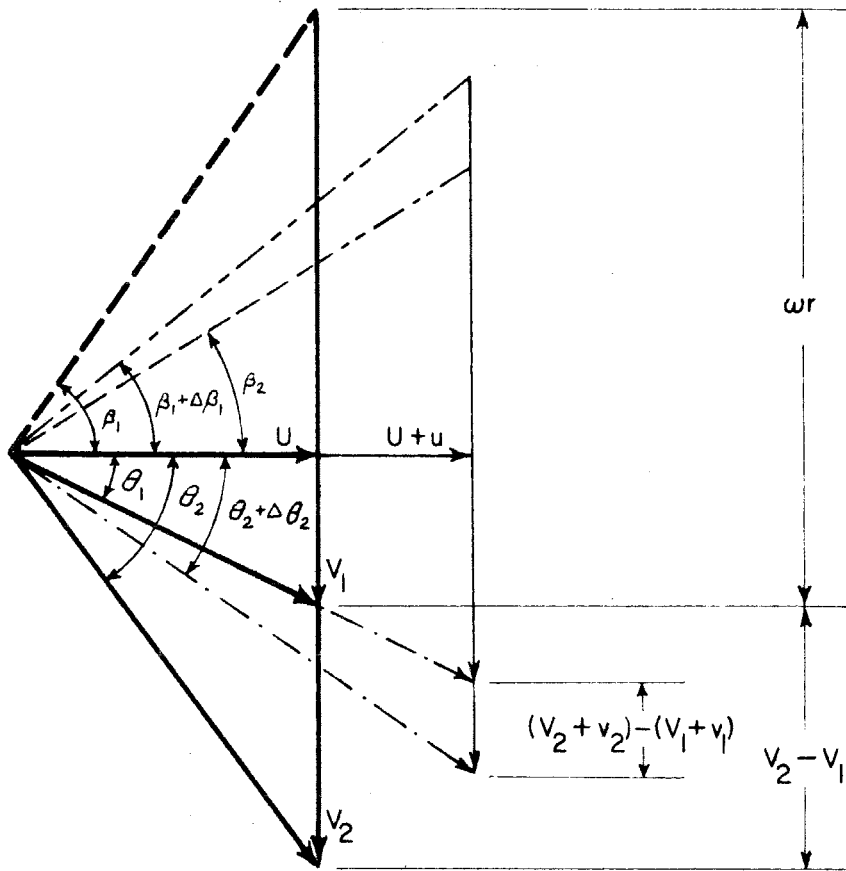
Fig. 6.   Velocity Diagrams at a Rotor Blade Row.
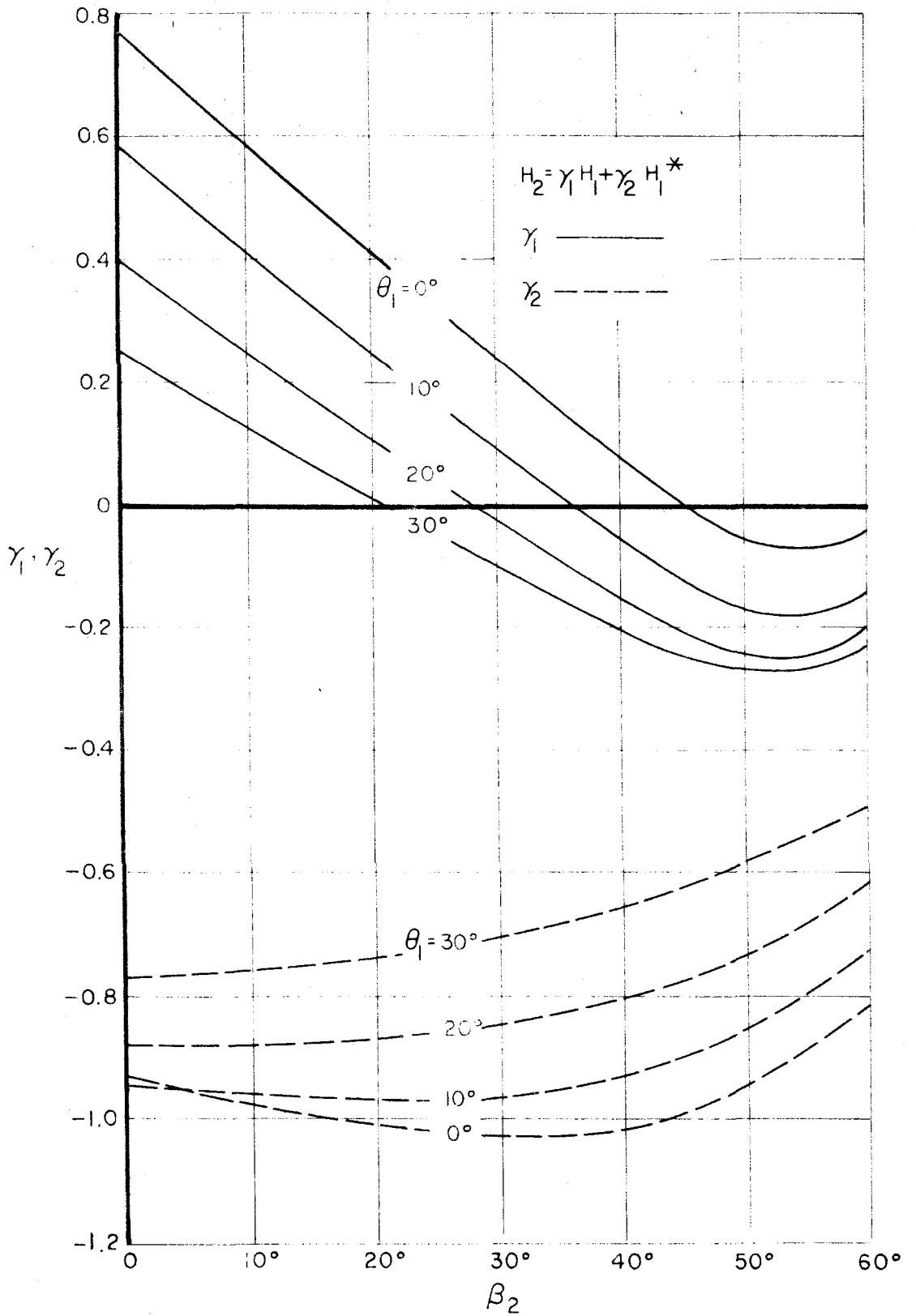
Fig. 7. Attenuation of an Inlet Distortion Through an

Isolated Rotor. No Losses, $\delta_R = 0$, $\varphi = \frac{1}{2}$.
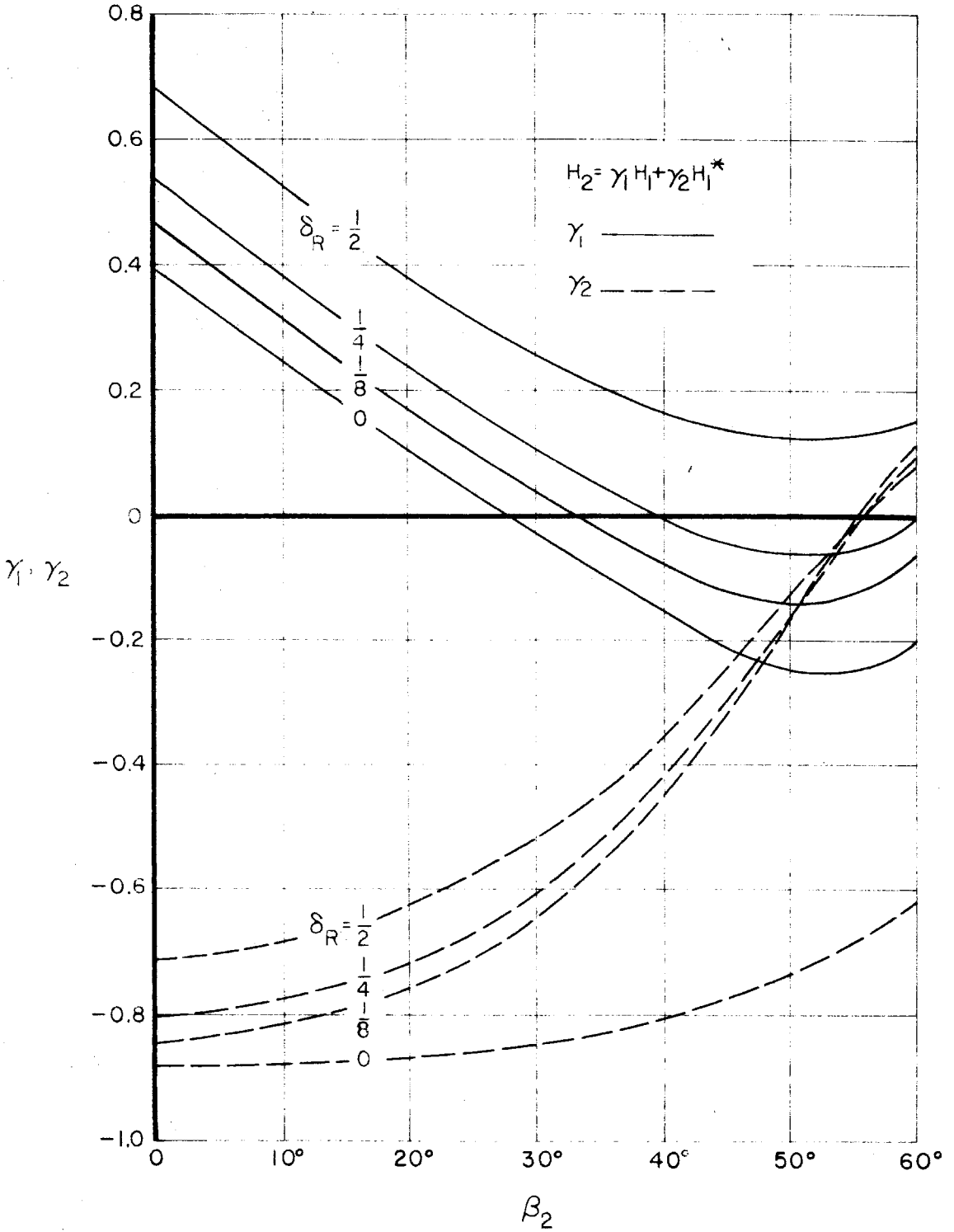
Fig. 8. Attenuation of an Inlet Distortion Through an Isolated Rotor. No Losses, $\delta_R \neq 0$, $\theta_1 = 20°$, $\varphi = \frac{1}{2}$.
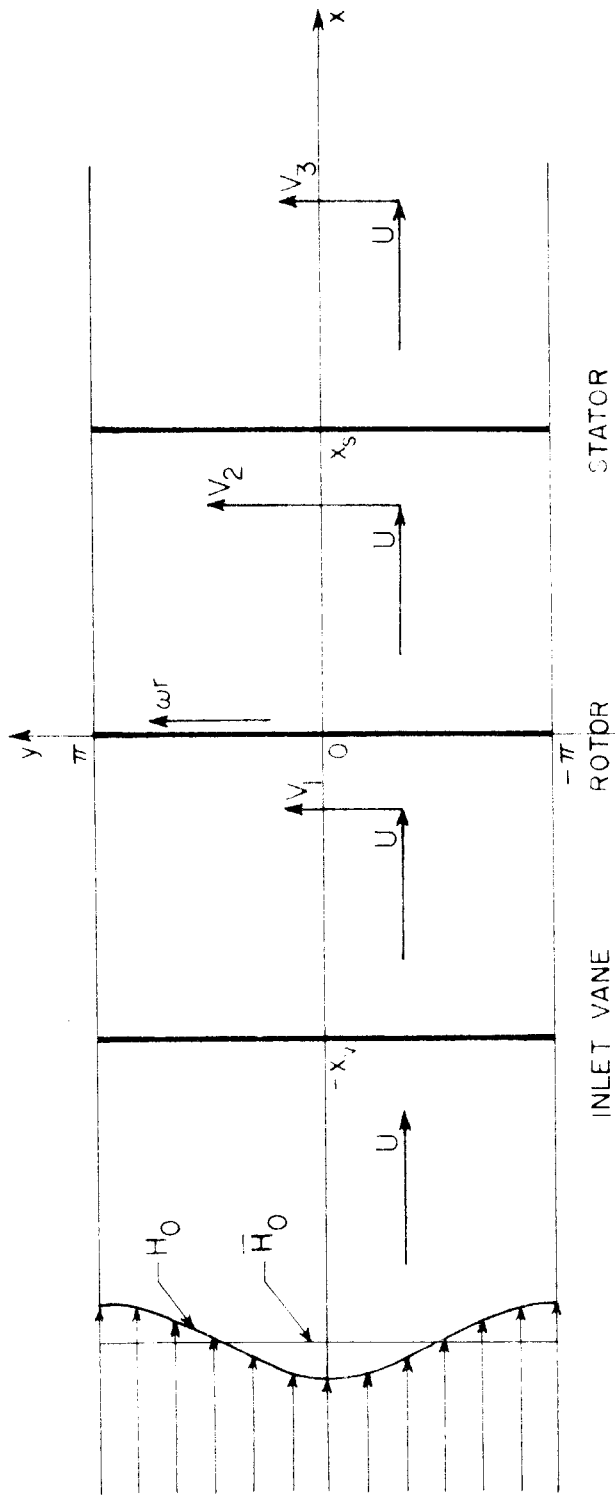
Fig. 9. Inlet Vane - Rotor - Stator Configuration.
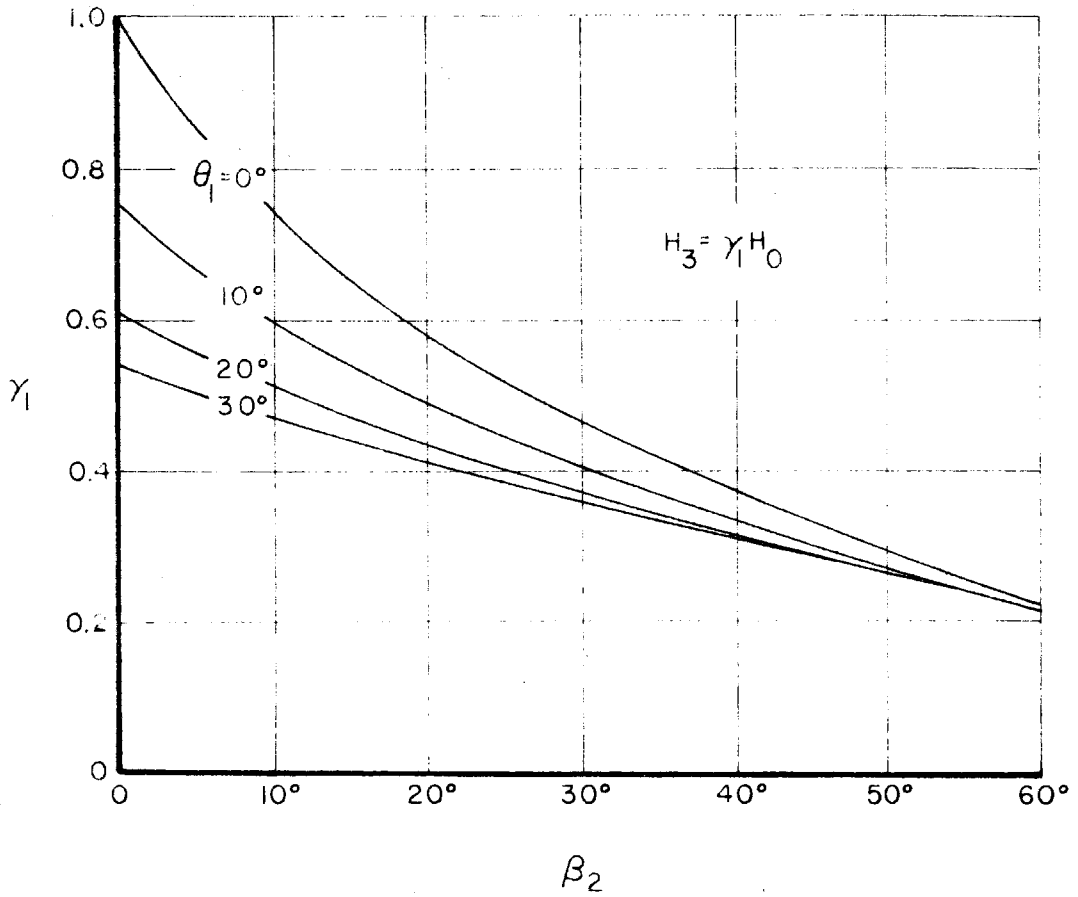
Fig. 10. Attenuation of an Inlet Distortion Through an Inlet Vane - Rotor - Stator Configuration. Zero Axial Gap, No Losses, $\delta_V = \delta_R = \delta_S = 0$, $\theta_1 = \theta_3$, $\varphi = \frac{1}{2}$.
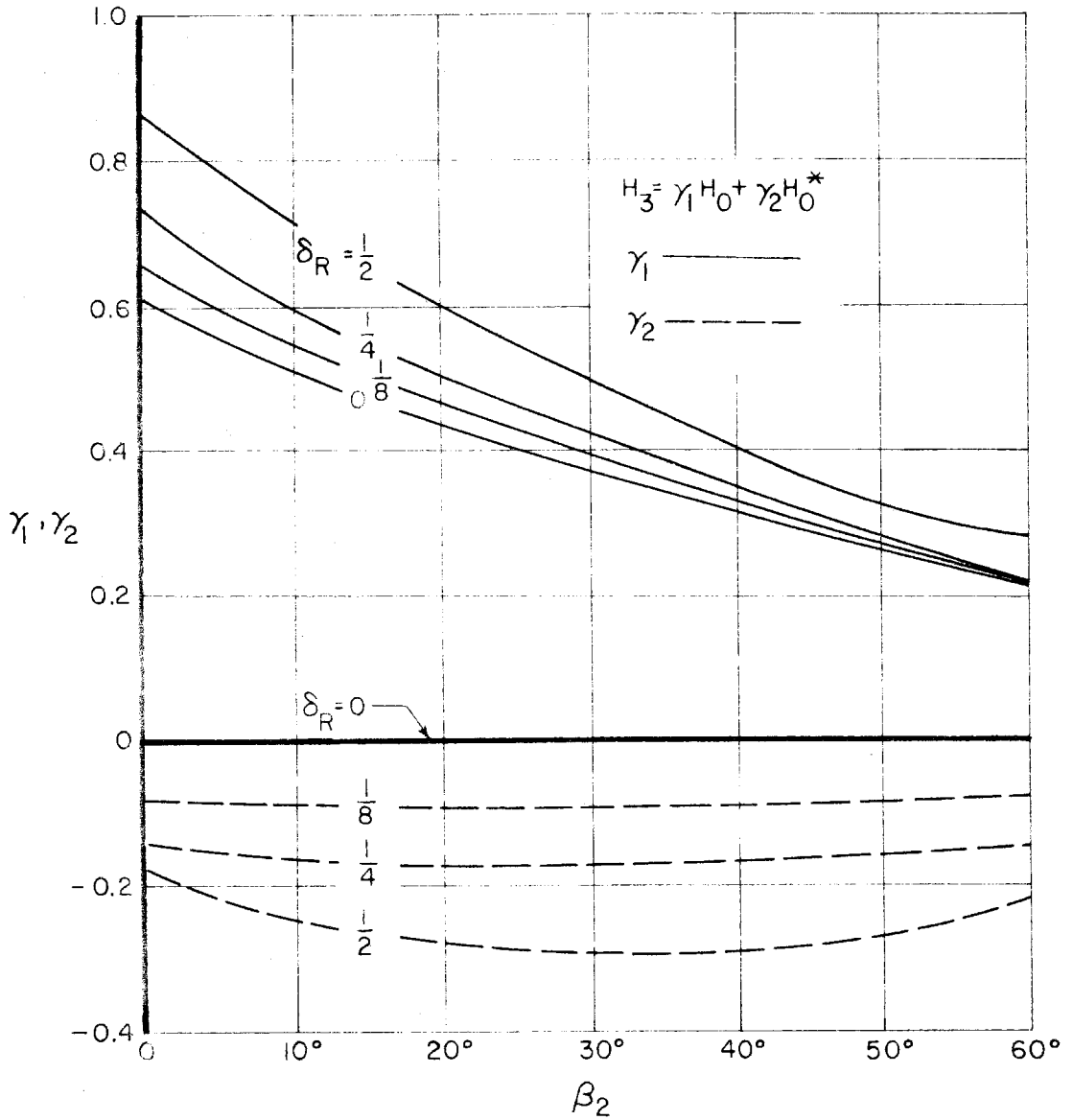
Fig. 11. Attenuation of an Inlet Distortion Through an Inlet Vane - Rotor - Stator Configuration. Zero Axial Gap, No Losses, $\delta_V = \delta_R = \delta_S \neq 0$, $\theta_1 = \theta_3 = 20°$, $\varphi = \frac{1}{2}$.
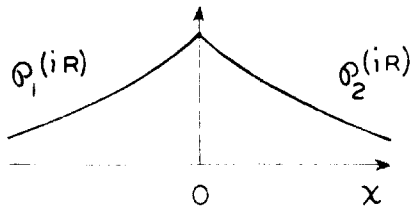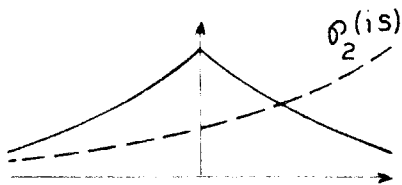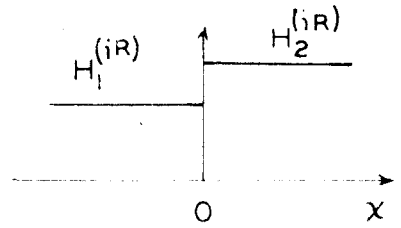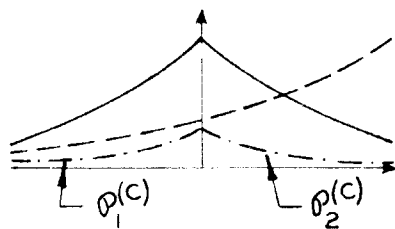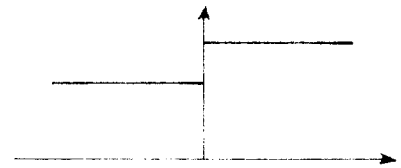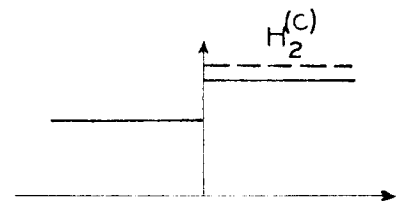
ROTOR WITH SUPERPOSED STATOR
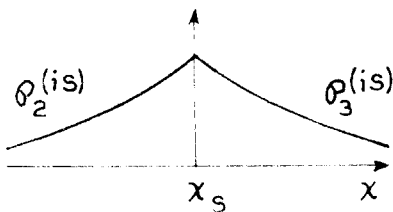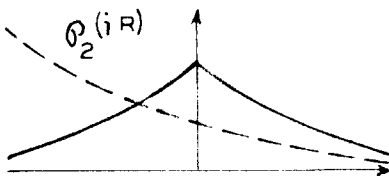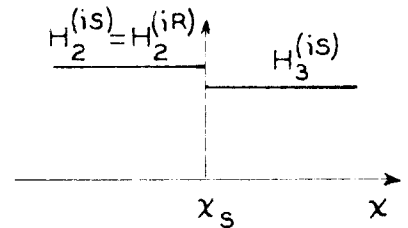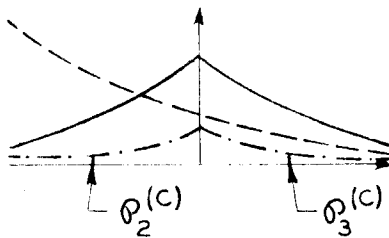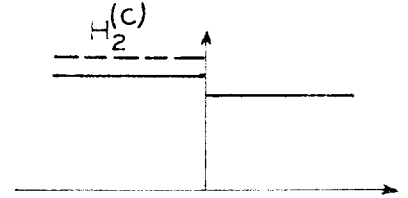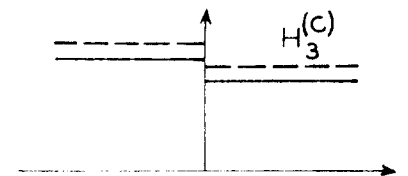
STATOR WITH SUPERPOSED ROTOR

Interference of Neighboring Blade Rows.
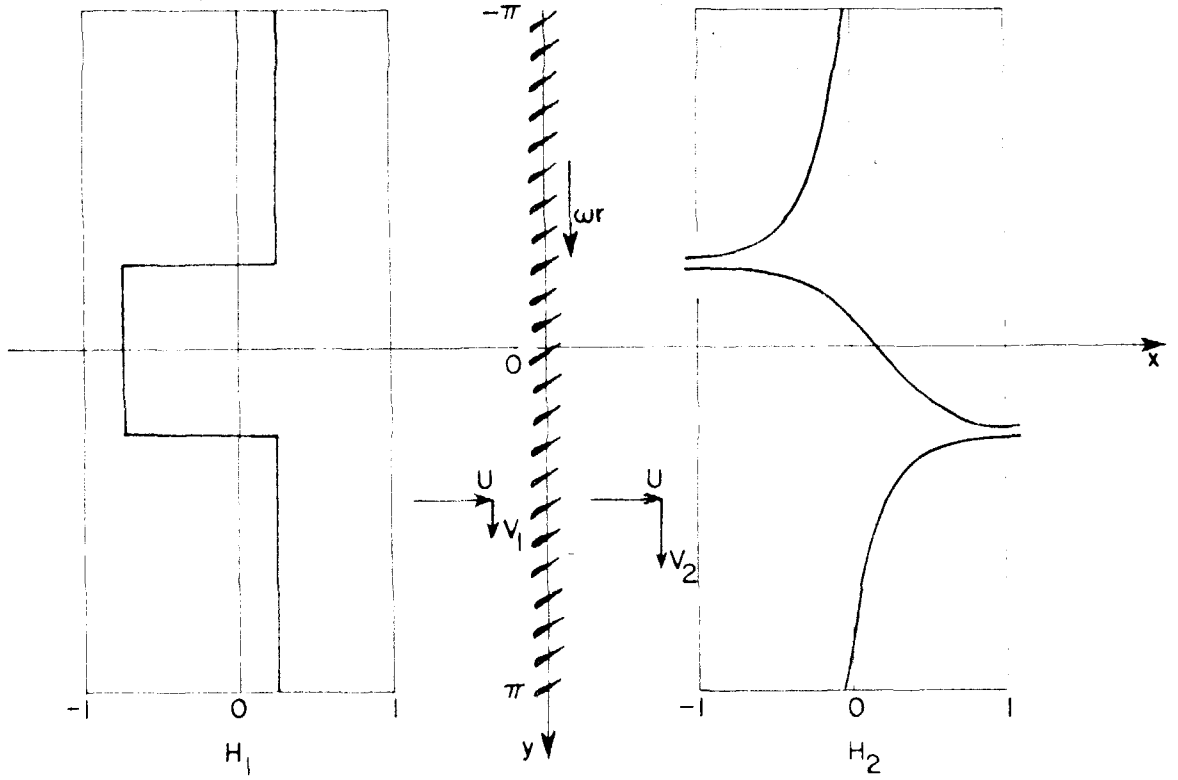
Fig. 13. Example Total Pressure Profile.
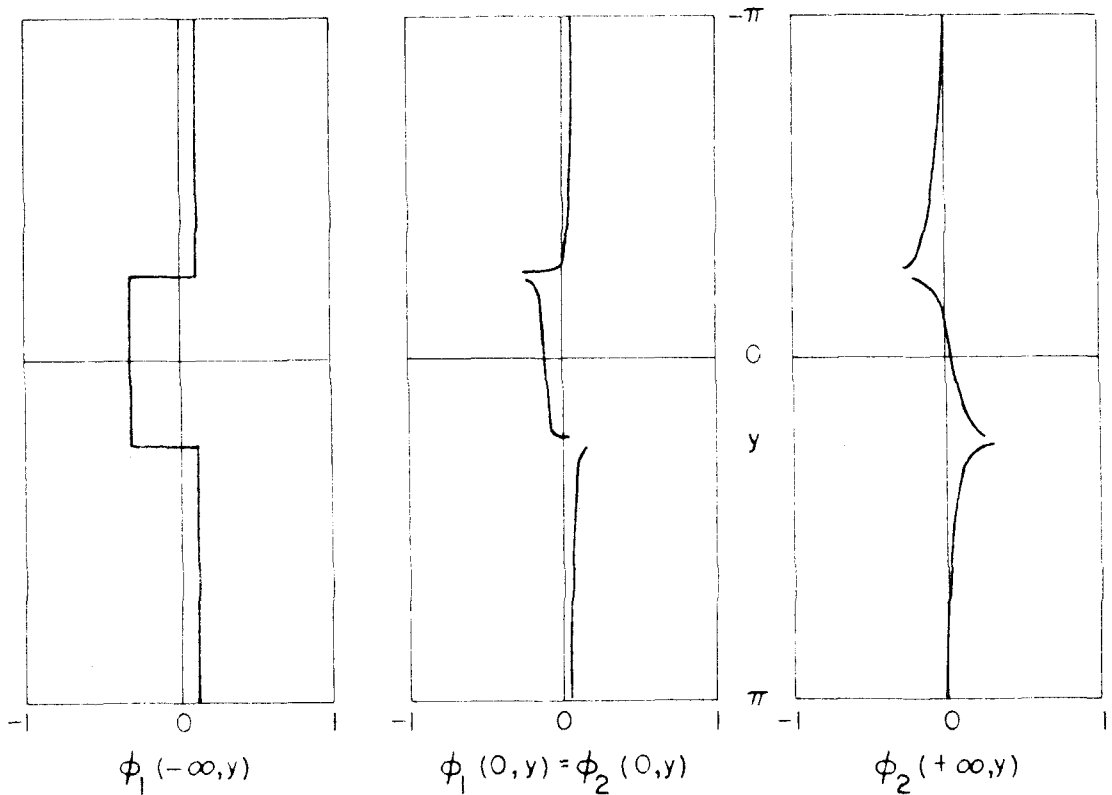
Fig. 14. Example Axial Velocity Profiles.
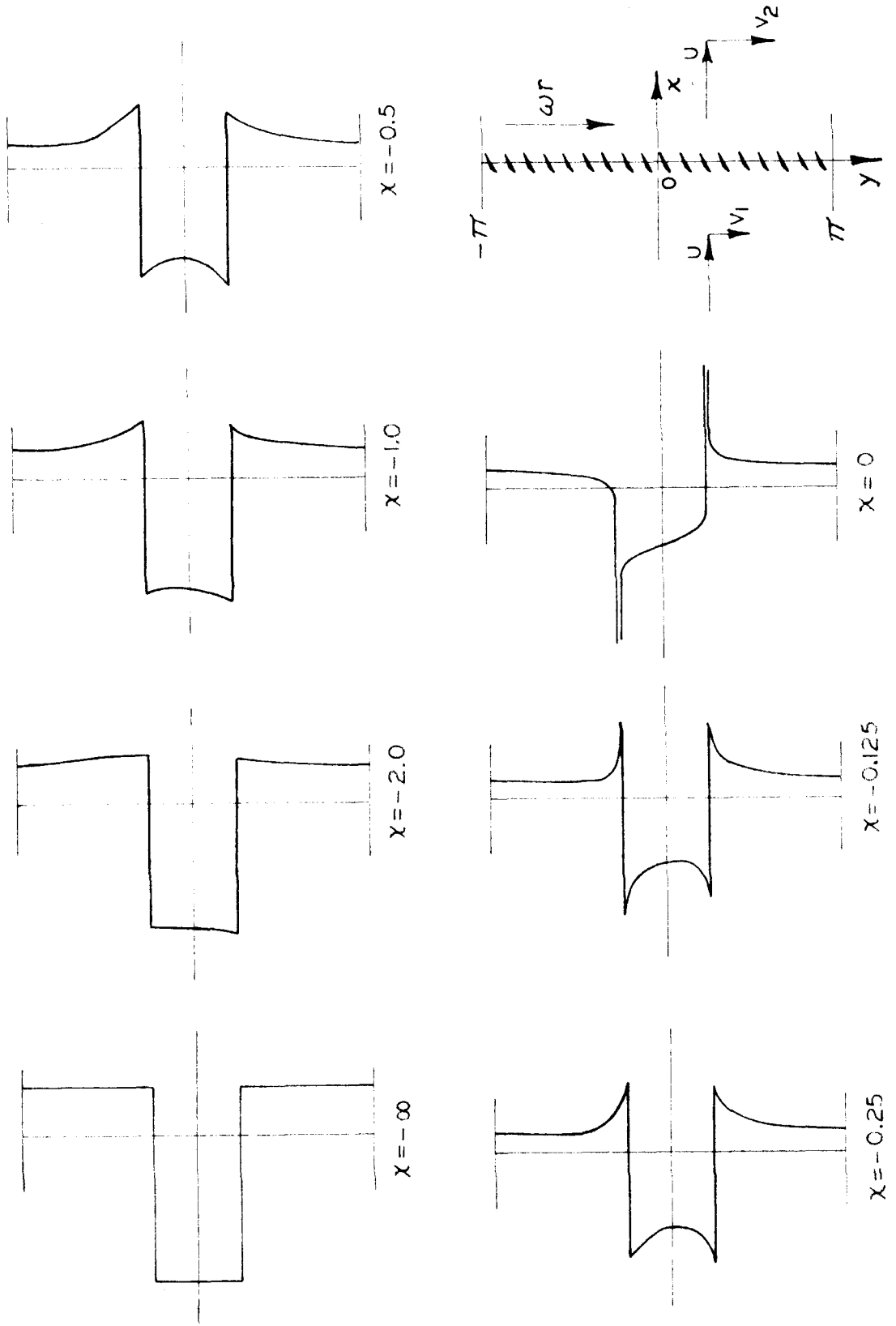
Fig. 15. Example Axial Velocity Profiles Upstream of the Rotor.
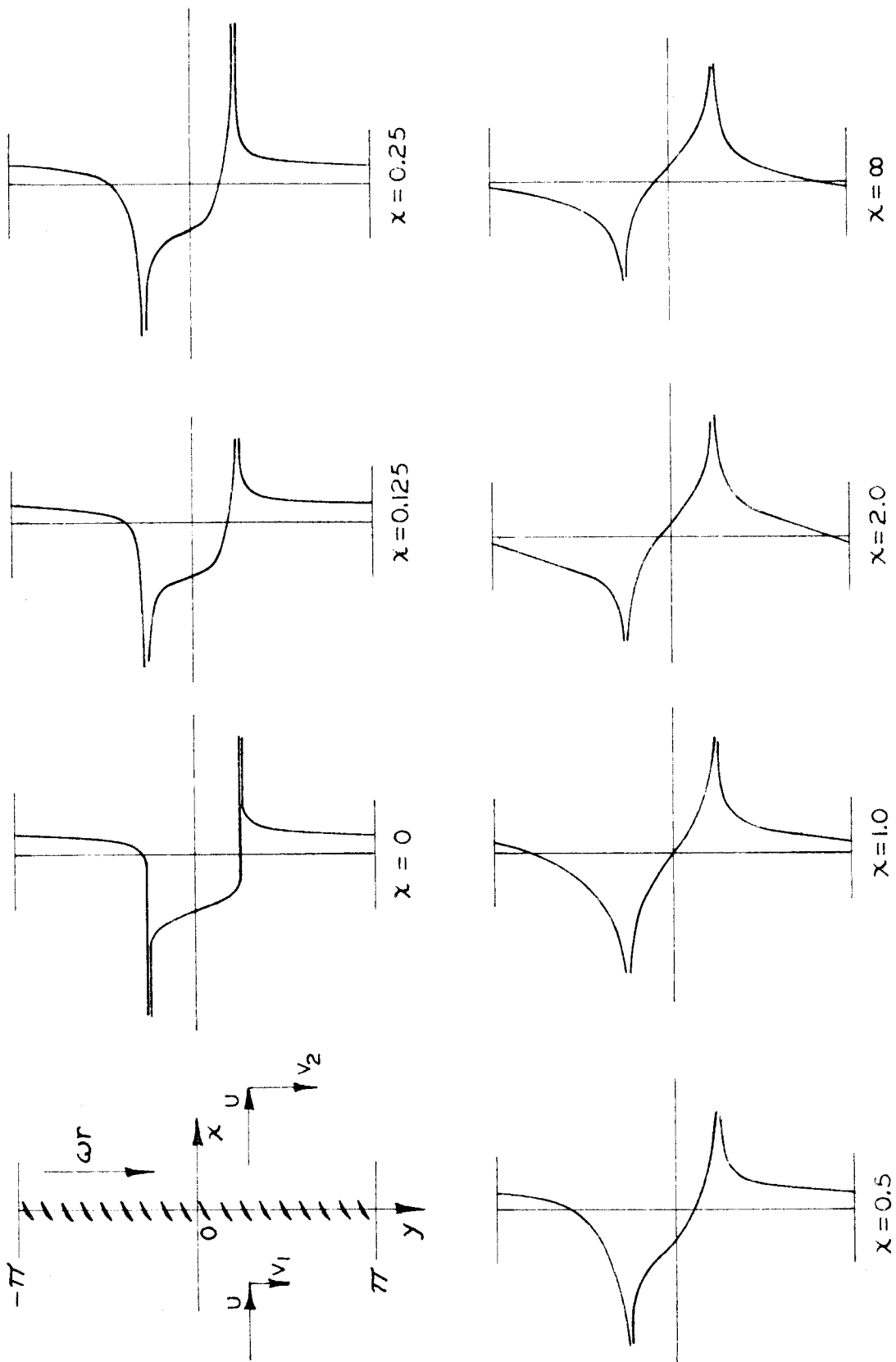
Fig. 16. Example Axial Velocity Profiles Downstream of the Rotor.
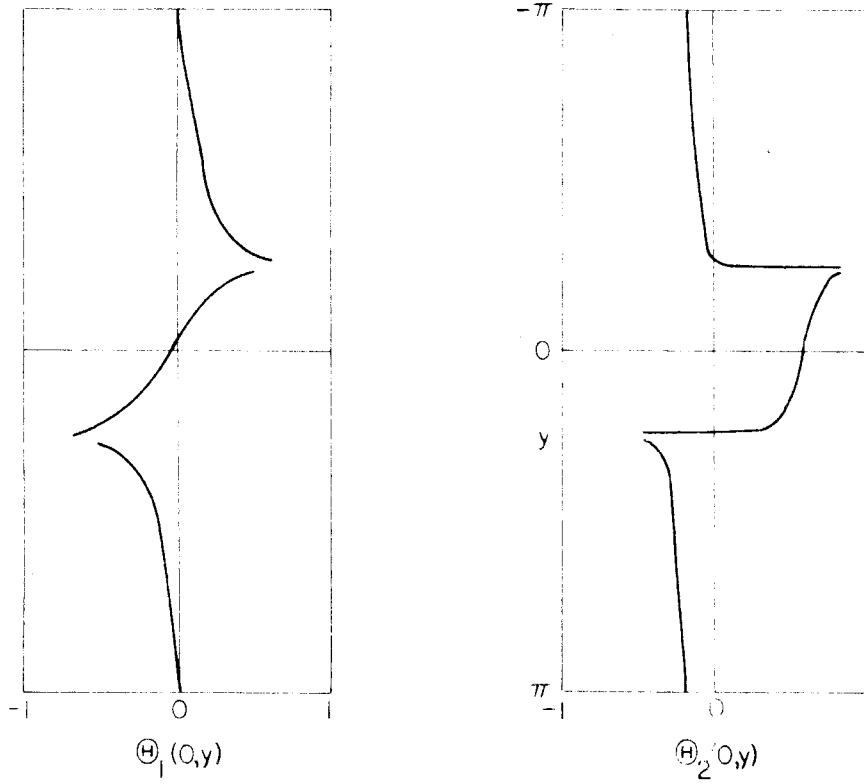
Fig. 17. Example Flow Angle Profiles.
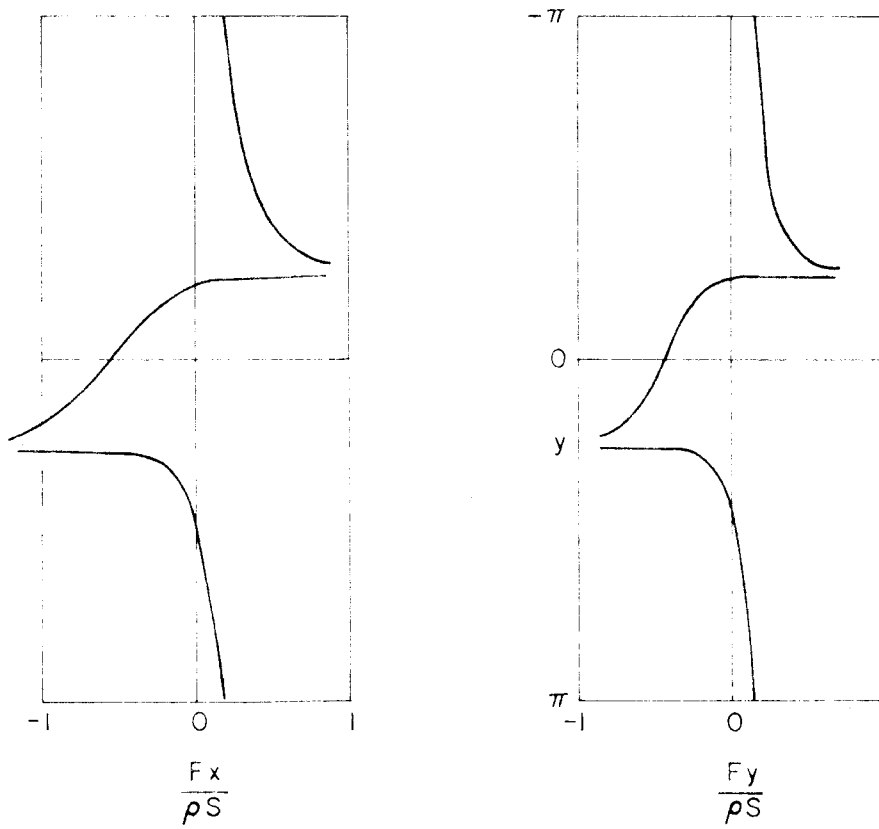
Fig. 18. Example Blade Force Profiles.
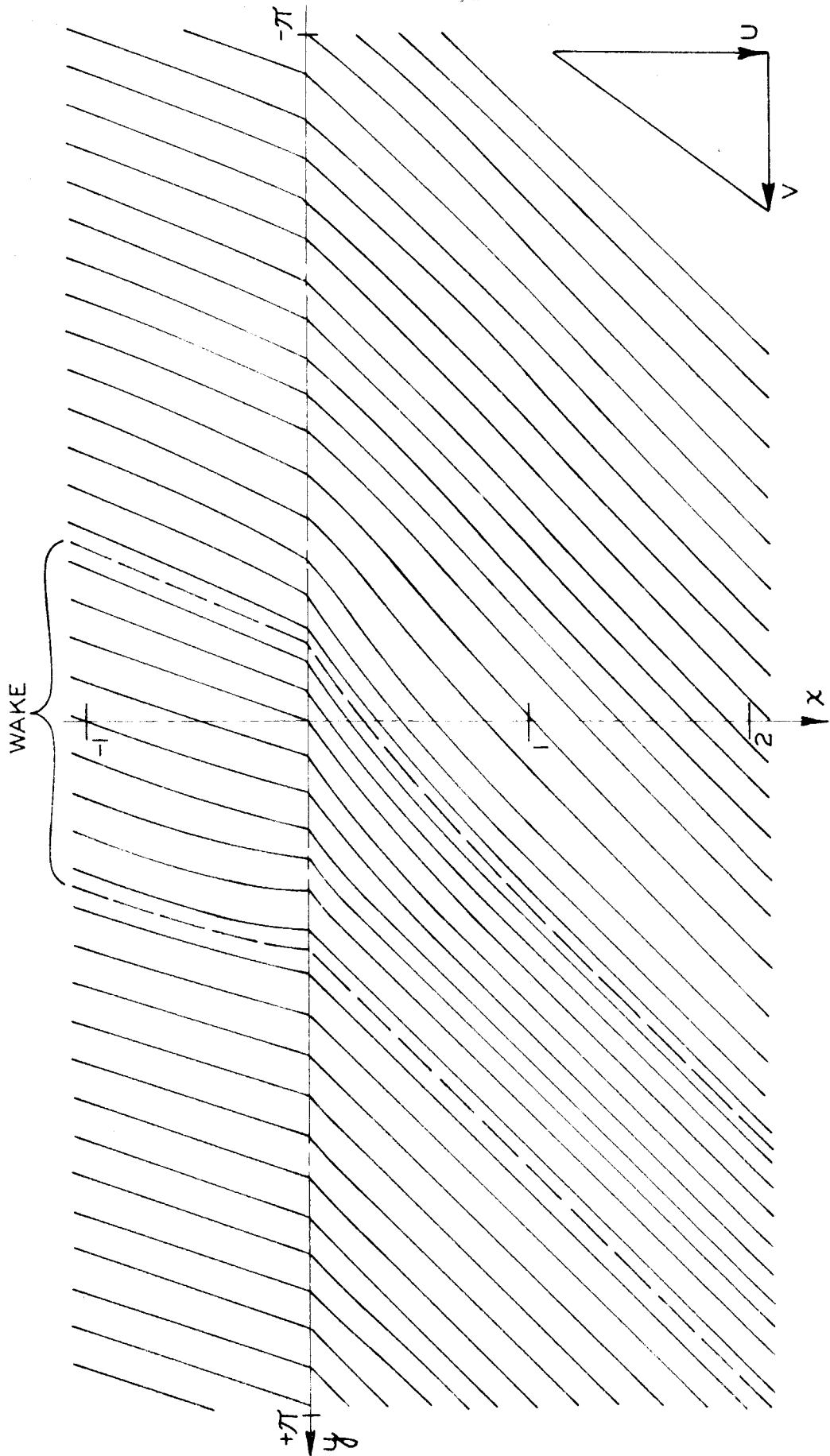
Fig. 19. Example Streamlines.
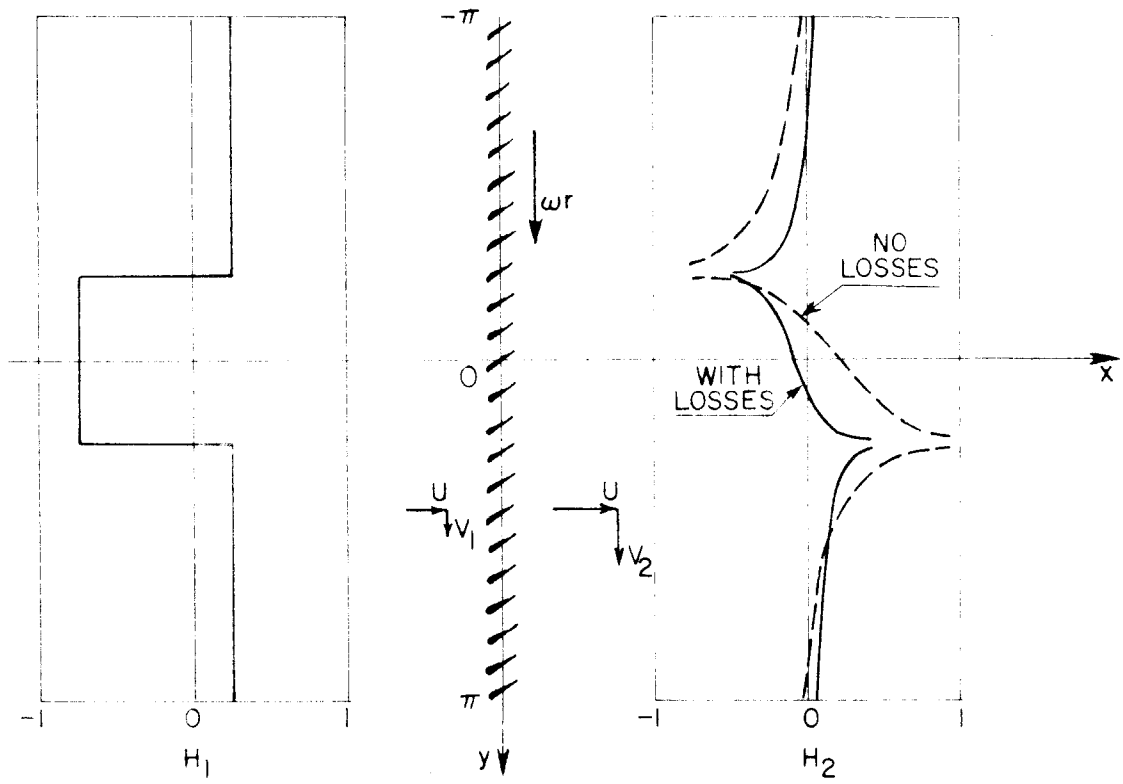
Fig. 20. Example Total Pressure Profiles with the Linear Loss.
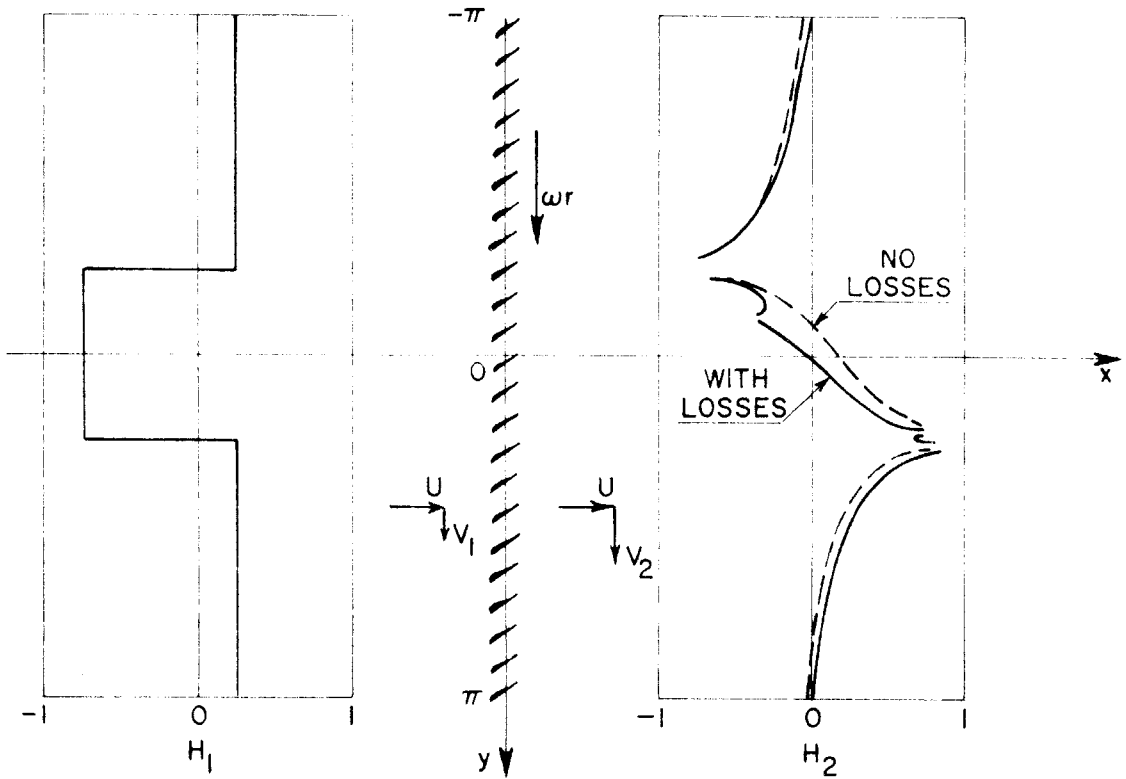
Fig. 21. Example Total Pressure Profiles with the Non-linear Loss.

Fig. 22. Axial-Flow Compressor

AIR
FLOW

ROTATION

INLET VANE

$\xi = 0.60$ $\xi = 1.00$

ROTOR

$\xi = 1.00$

$\xi = 0.60$

STATOR

$\xi = 0.60$

$\xi = 1.00$

$\mathcal{C}$
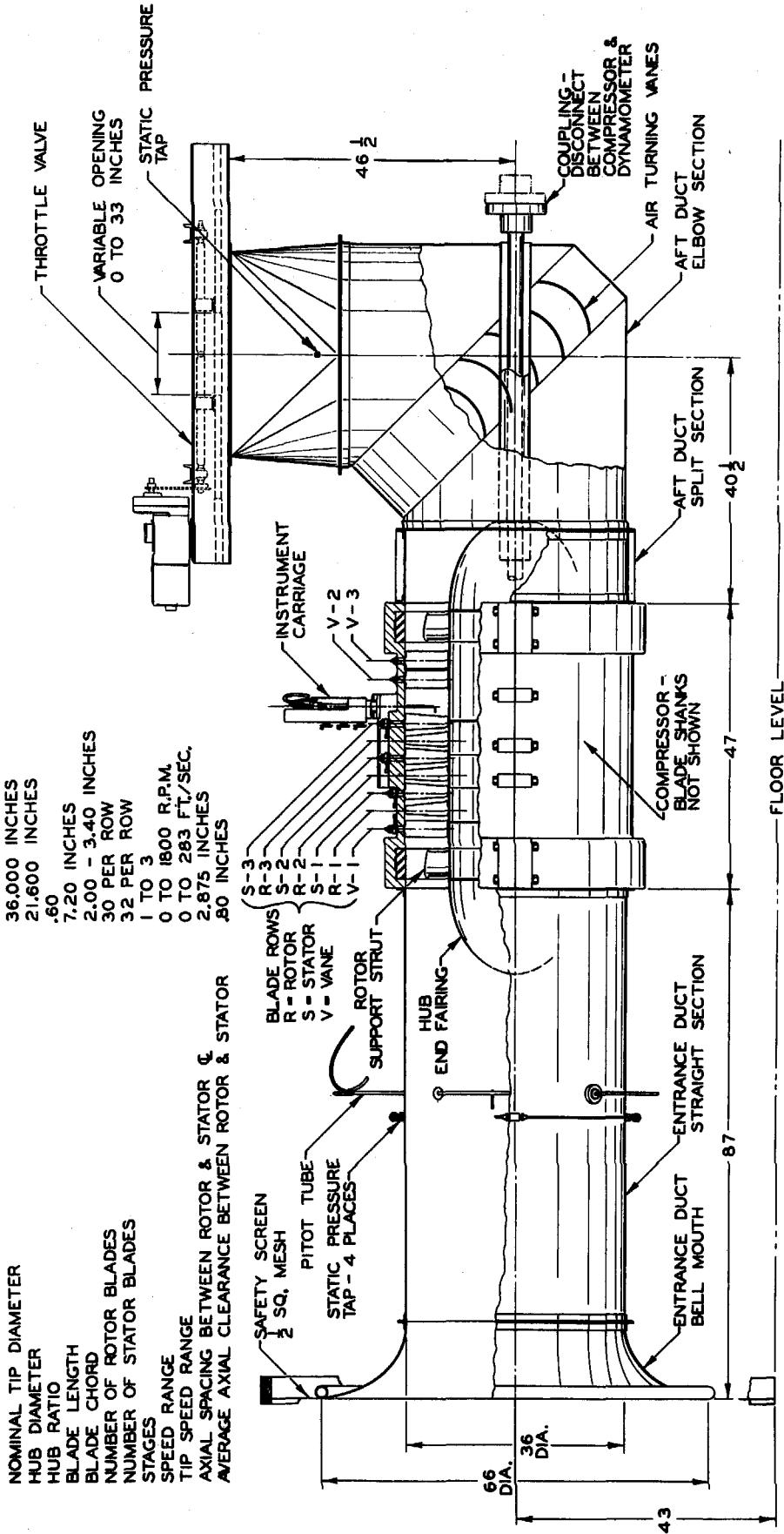
COMPR.
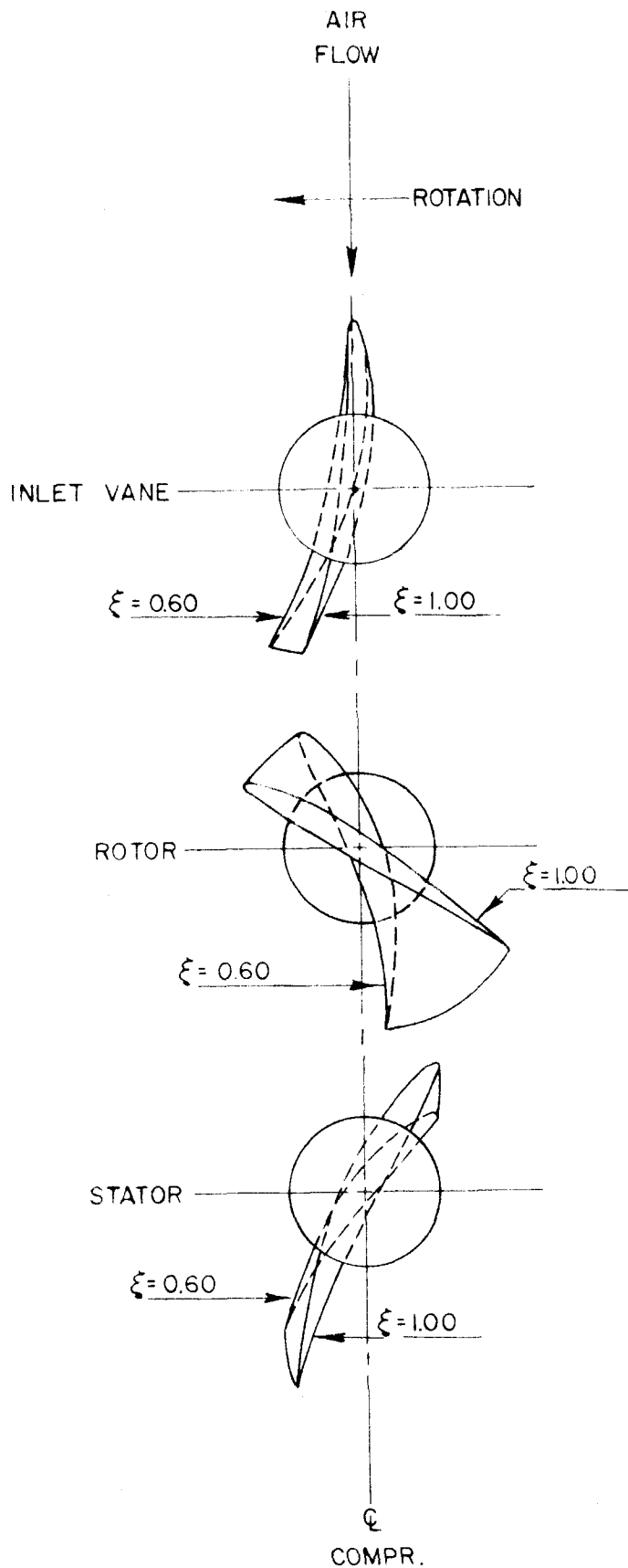
Fig. 23.   Free Vortex Blading.
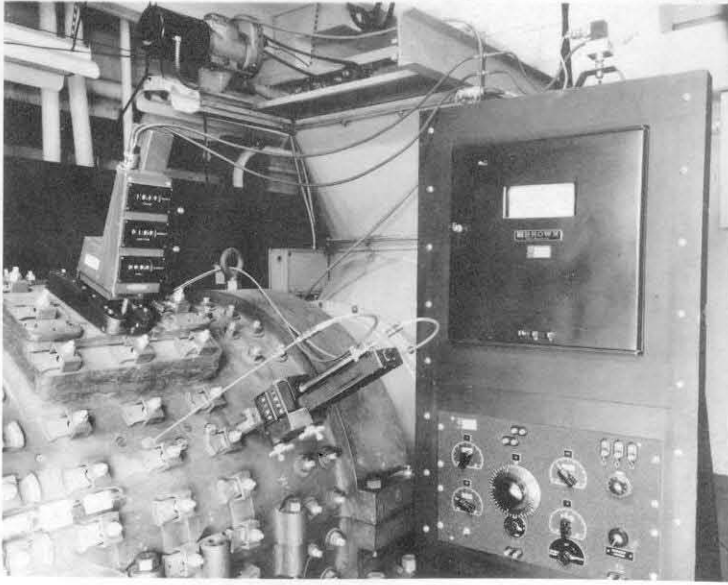
Fig. 24. Probe Carriages and Pressure Detecting Unit.

$\frac{5}{32}$ DIA. TYP.

CLAW TYPE
(DIRECTIONAL)

PITOT
(VELOCITY
HEAD)

KIEL
(TOTAL
HEAD)

PROBES SHOWN APPROX. ACTUAL SIZE

Fig. 25.   Test Probes.

SCREEN

WIRE FRAMEWORK

SCREEN

INLET VANE

INLET FAIRING
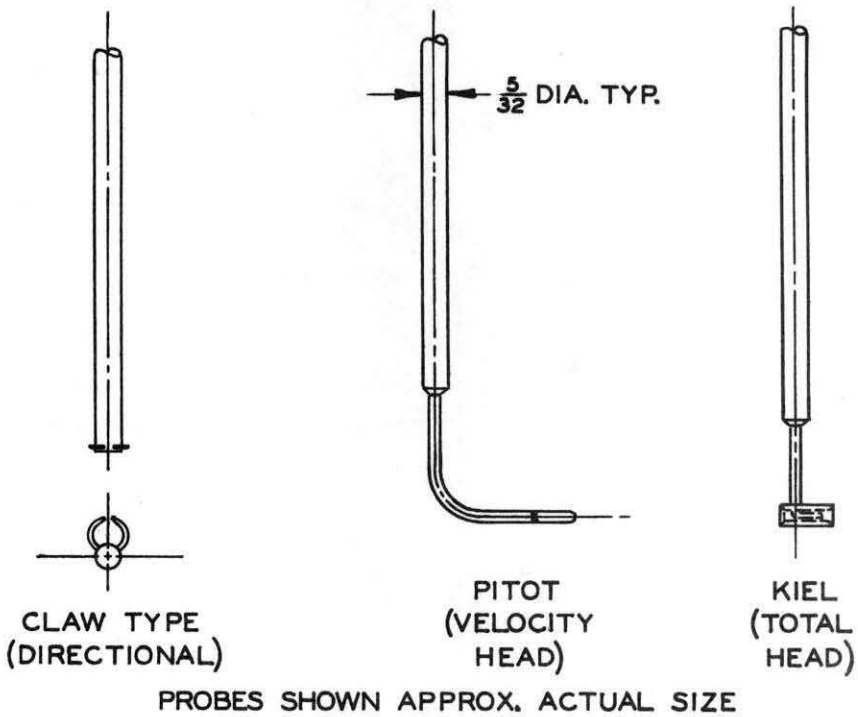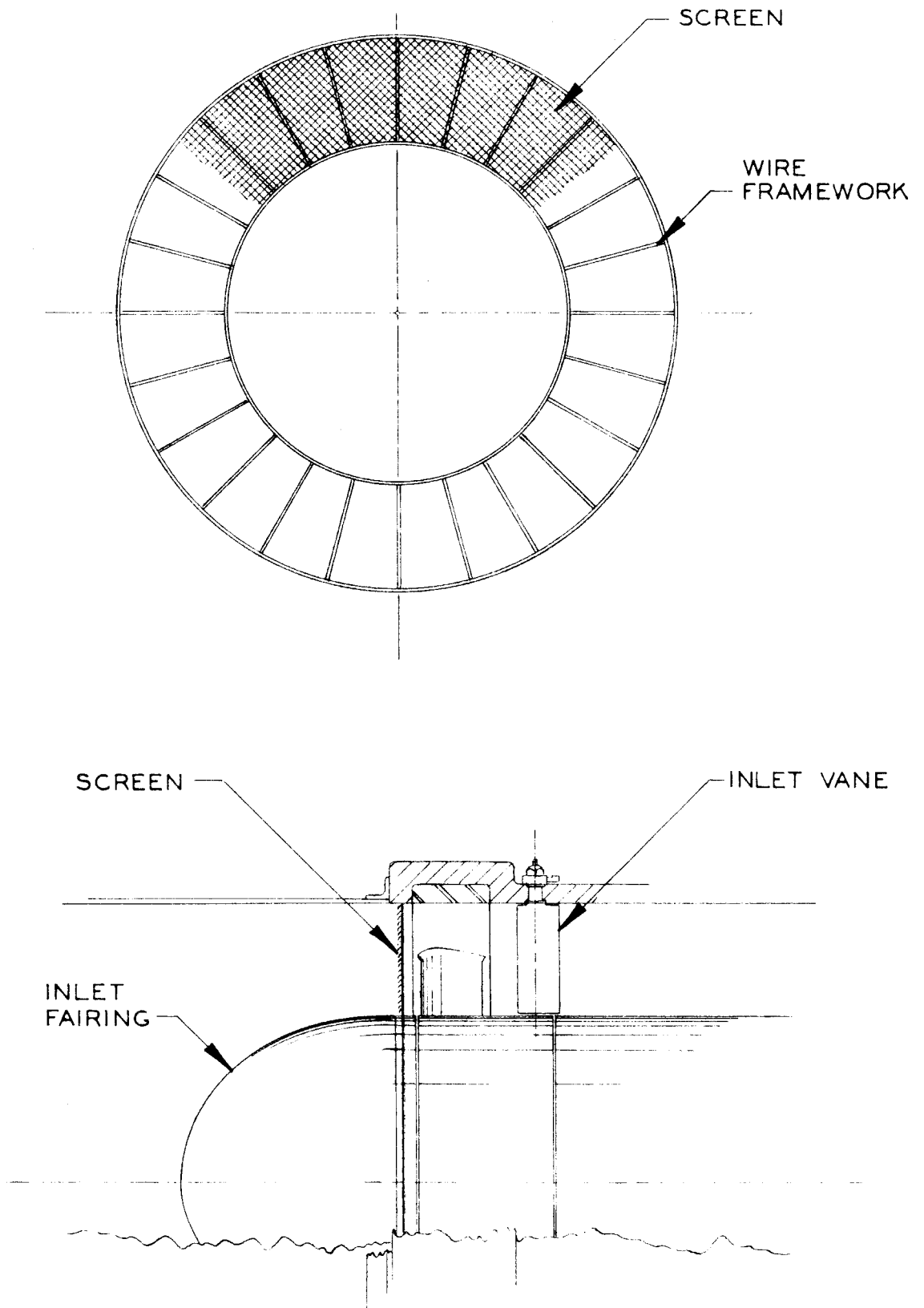
Fig. 26. Blockage Screen.
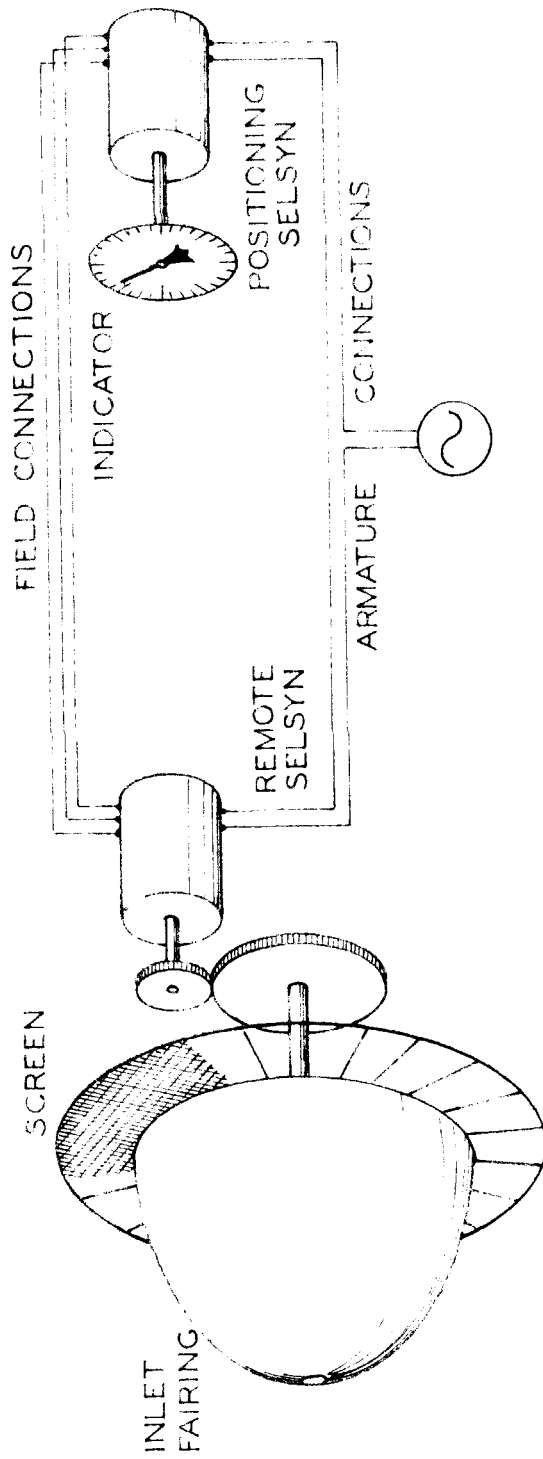
Fig. 27. Pictorial Diagram of the Screen Positioning Device.
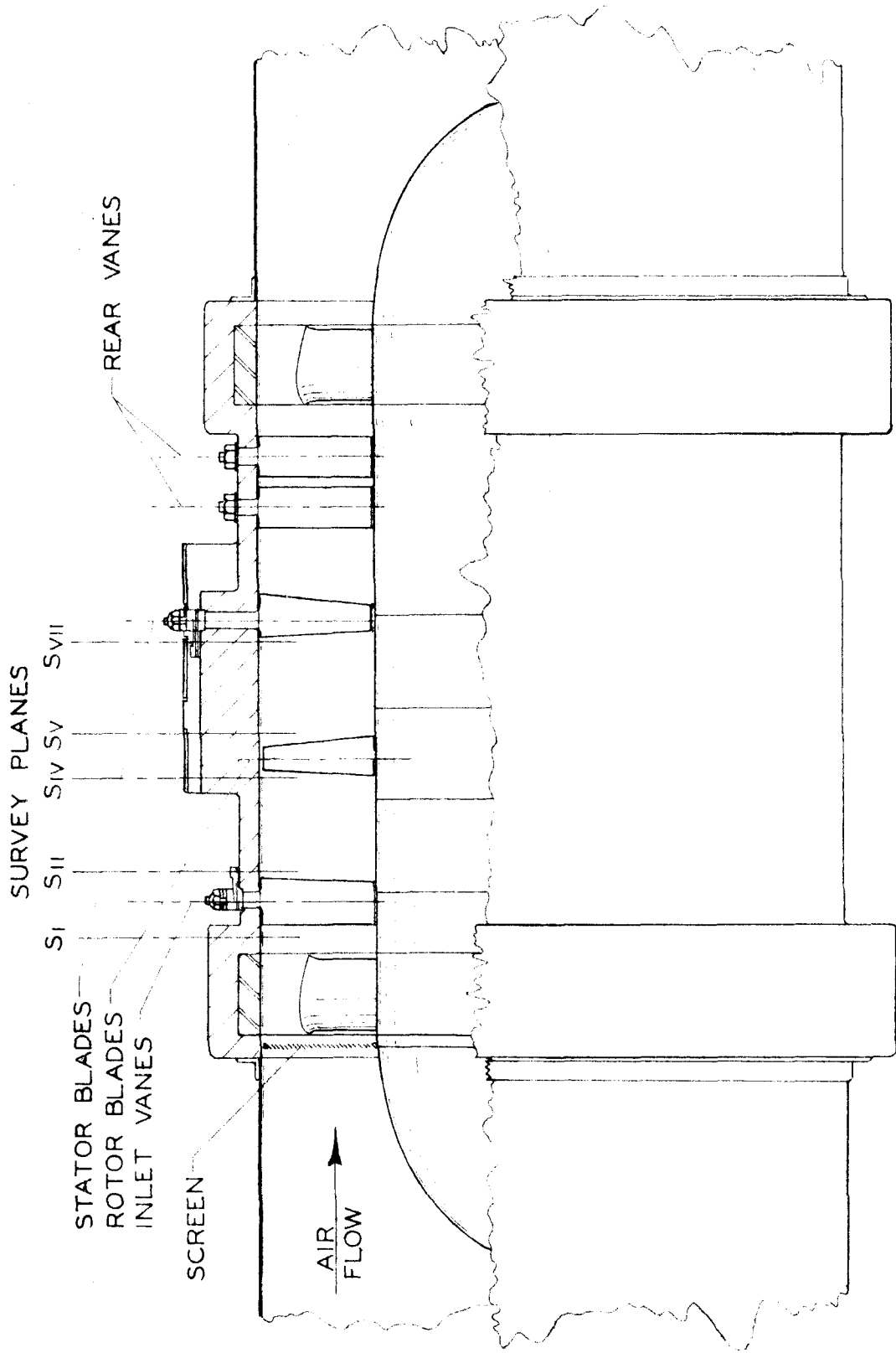
Fig. 28. Expanded Single Stage Configuration.

CIRCUMFERENTIAL ANGLE
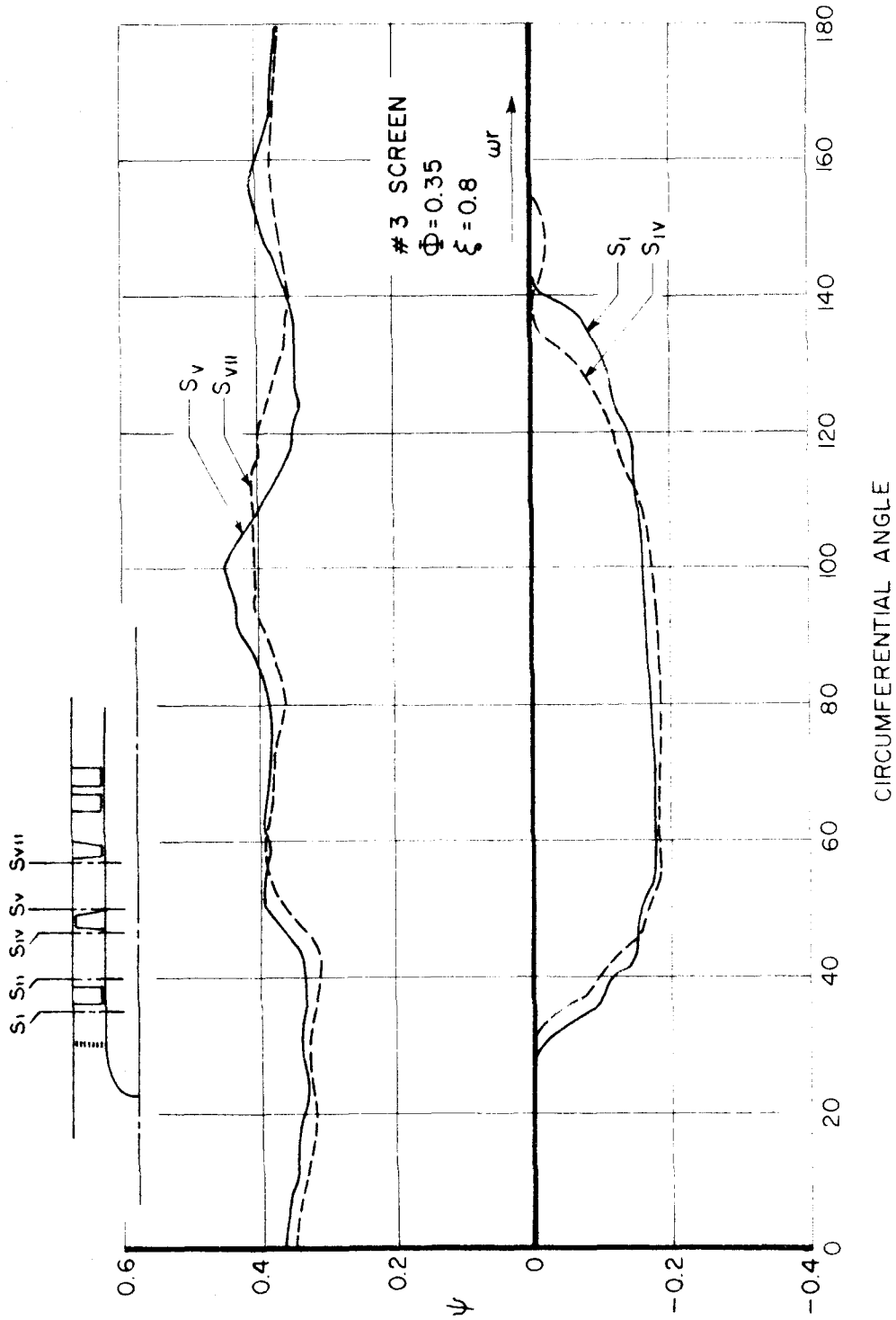
Fig. 29. Total Pressure Survey at the Mean Radius.

Expanded Single Stage Configuration.
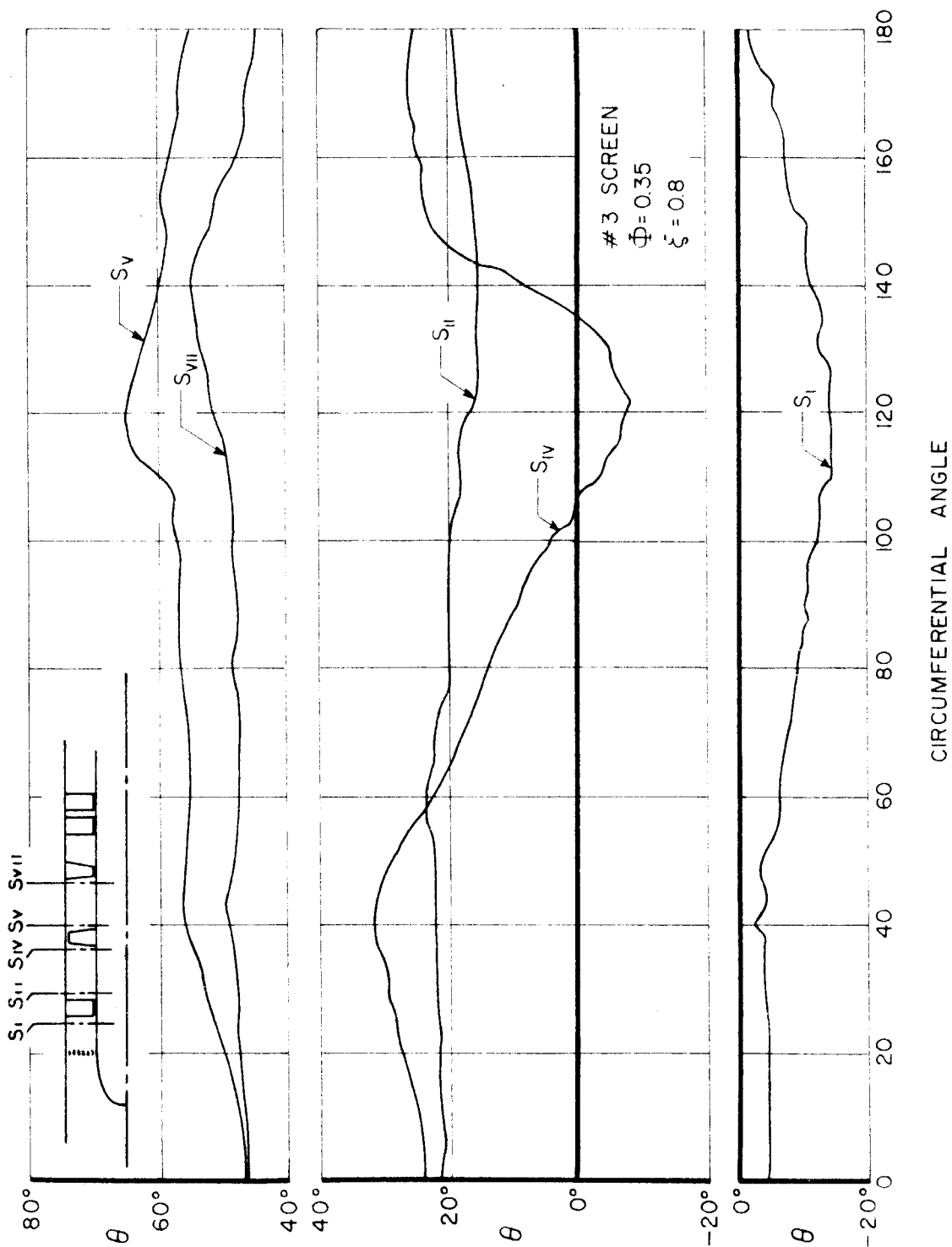
Fig. 30. Flow Angle Survey at the Mean Radius. Expanded Single Stage Configuration.
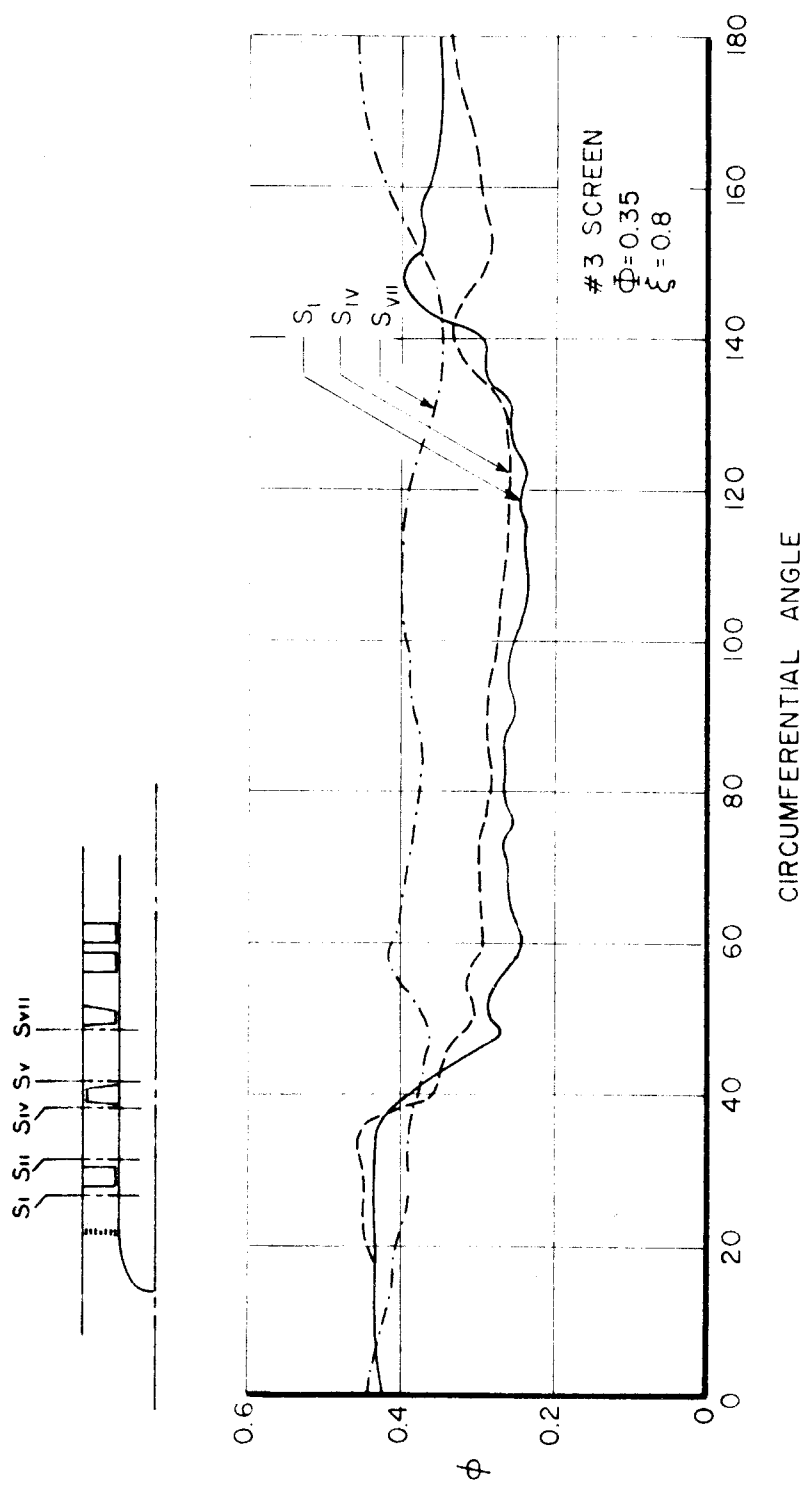
Fig. 31. Flow Coefficient Survey at the Mean Radius. Expanded Single Stage Configuration.
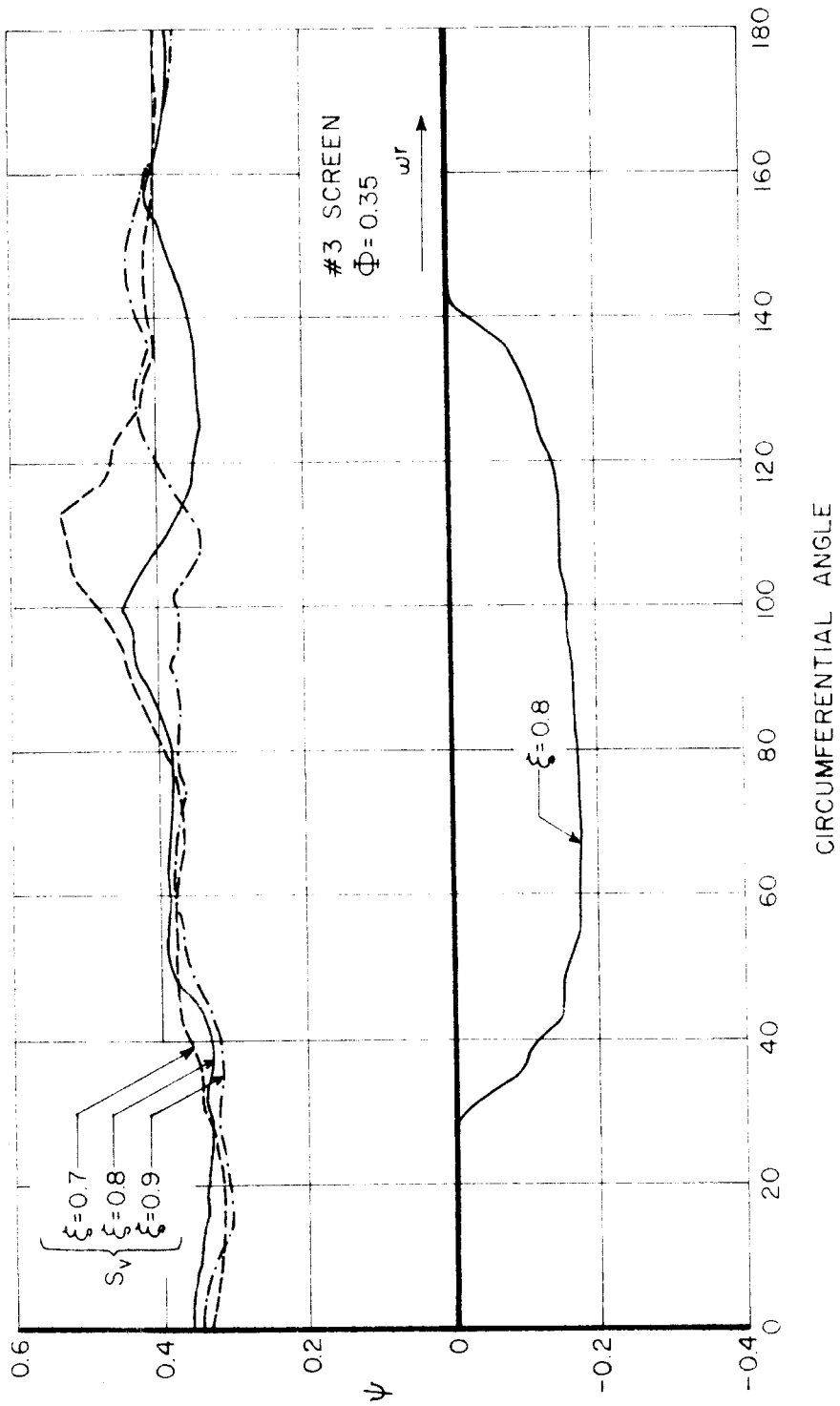
Fig. 32. Total Pressure Survey Downstream of the Rotor.

Expanded Single Stage Configuration.

CIRCUMFERENTIAL ANGLE
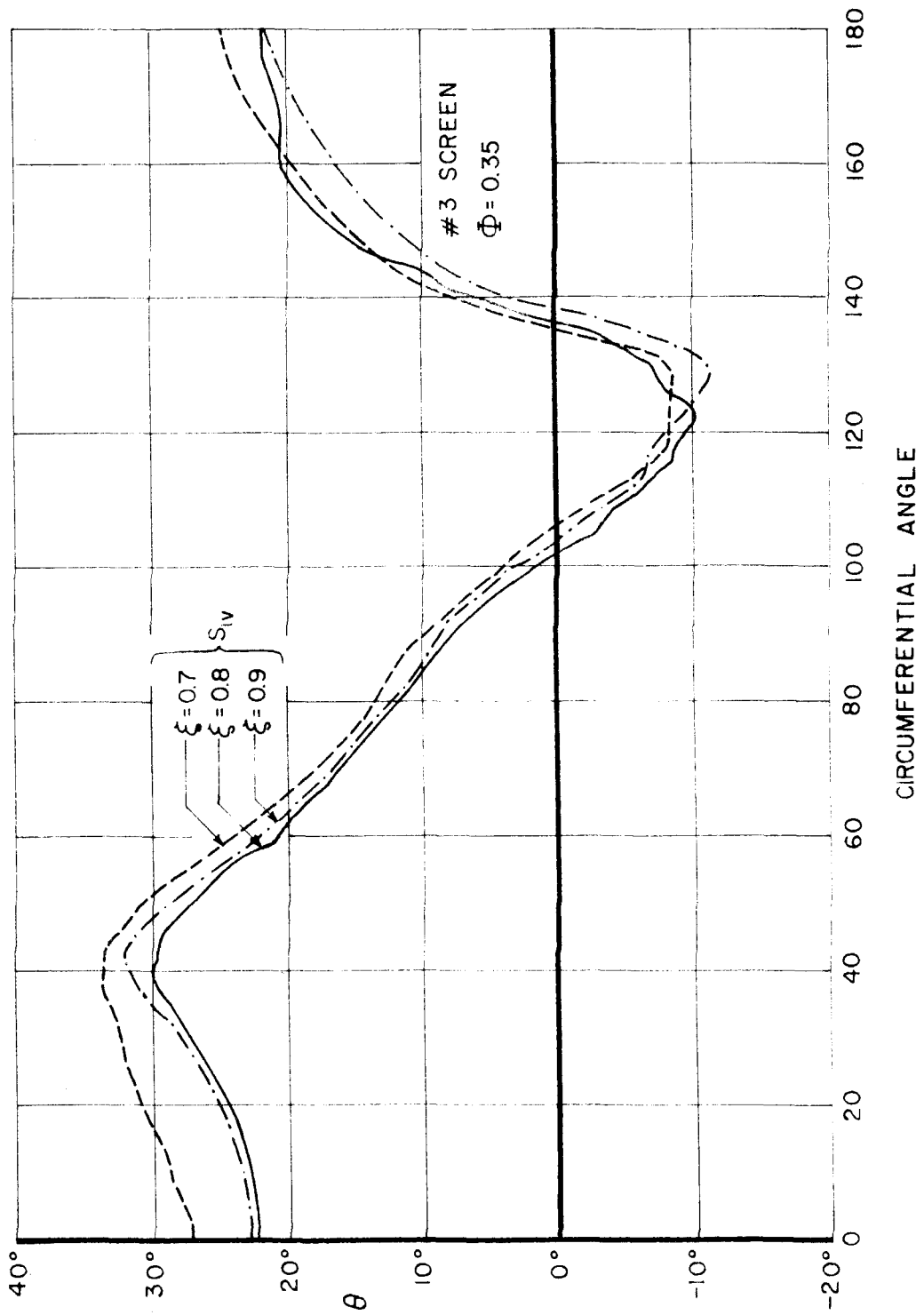
Fig. 33. Flow Angle Survey Upstream of the Rotor.

Expanded Single Stage Configuration.
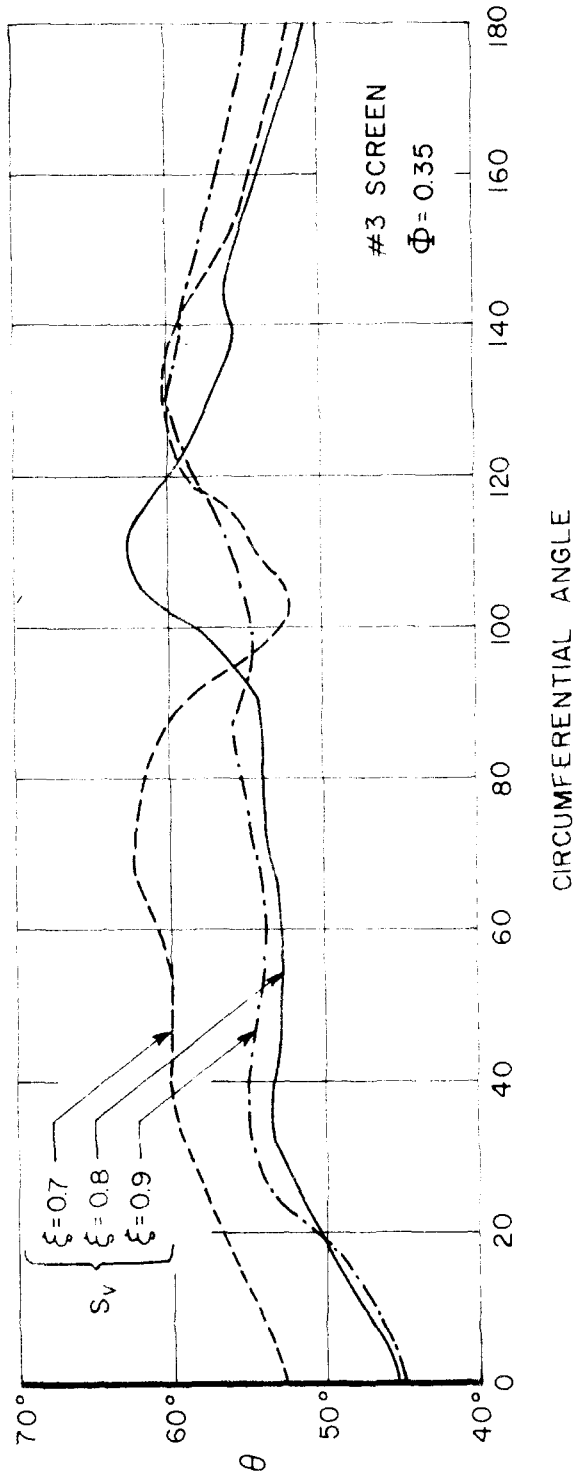
Fig. 34. Flow Angle Survey Downstream of the Rotor.
Expanded Single Stage Configuration.
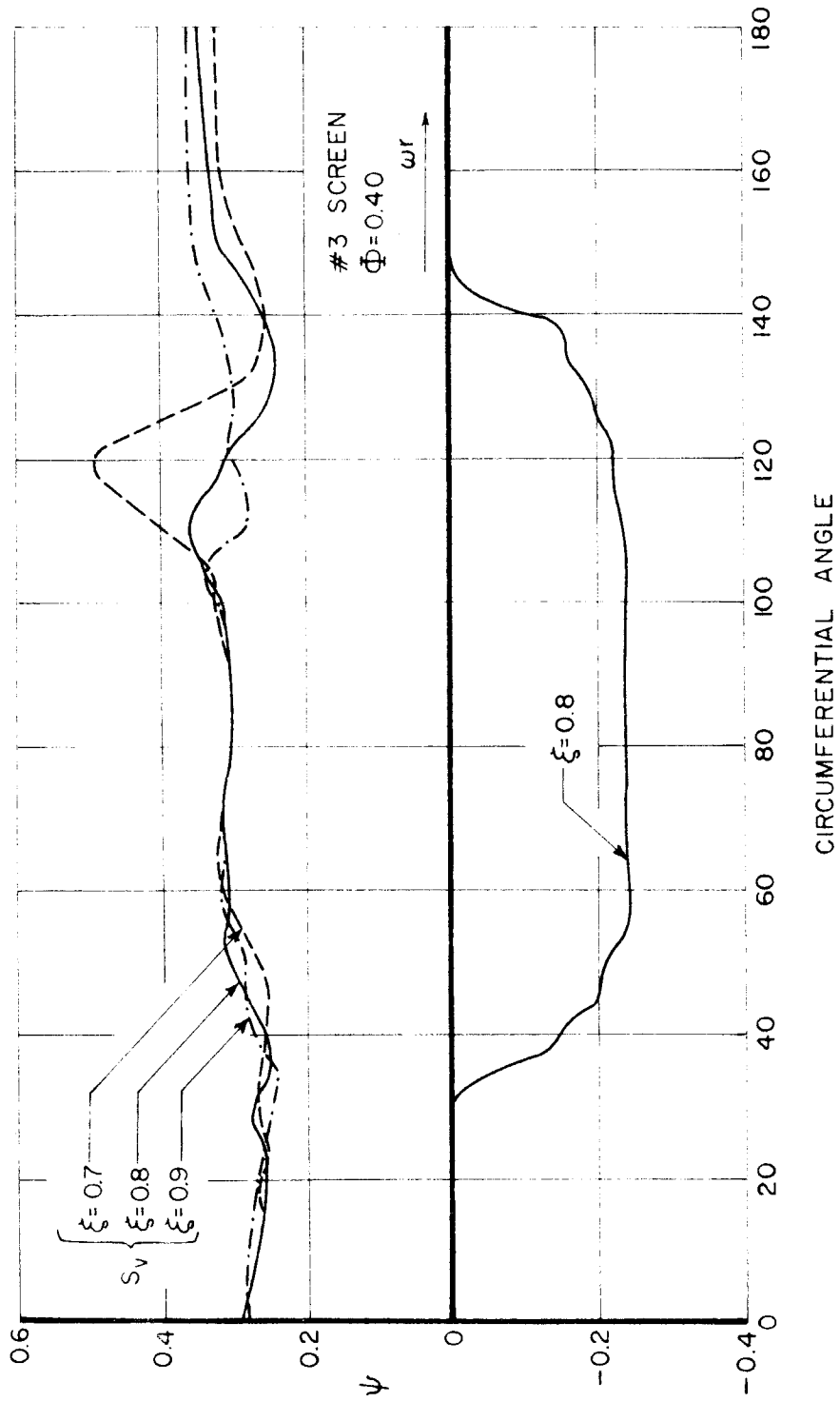
Fig. 35. Total Pressure Survey Downstream of the Rotor.

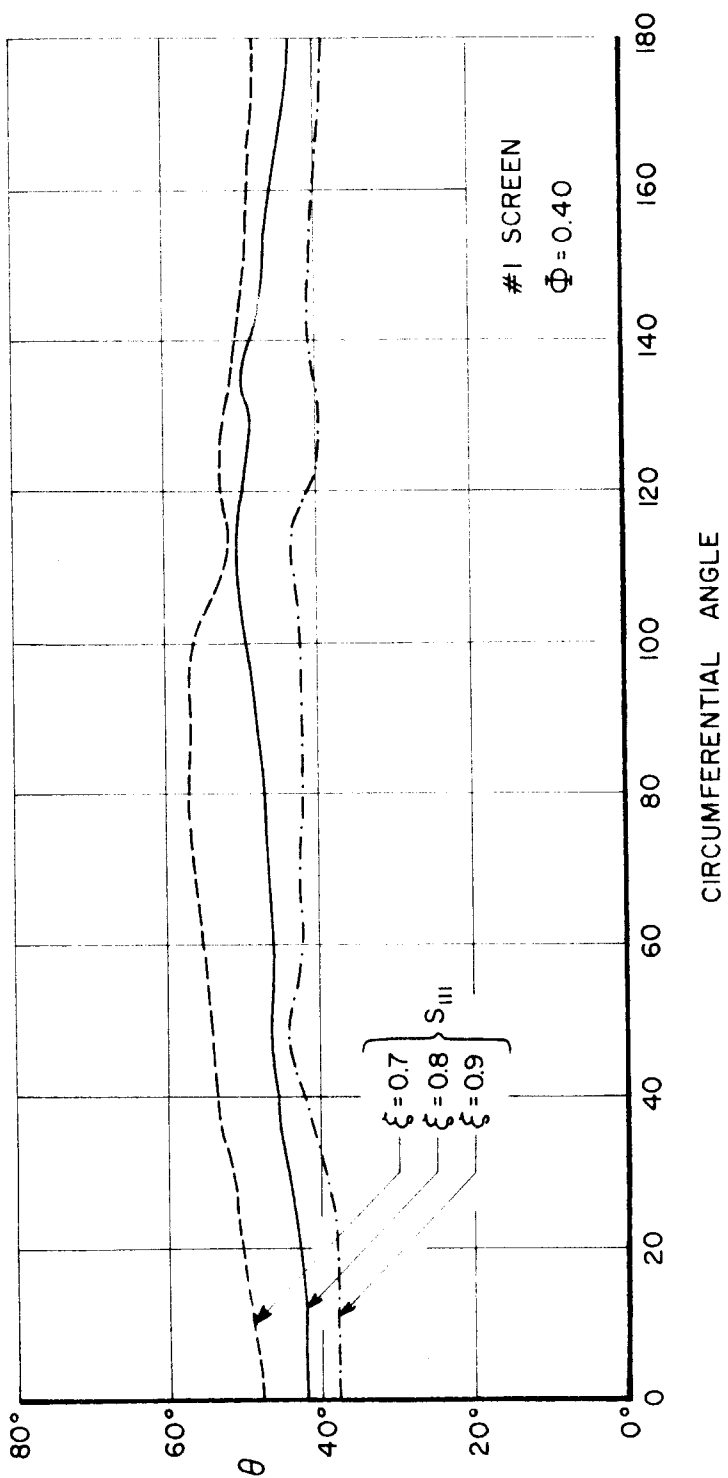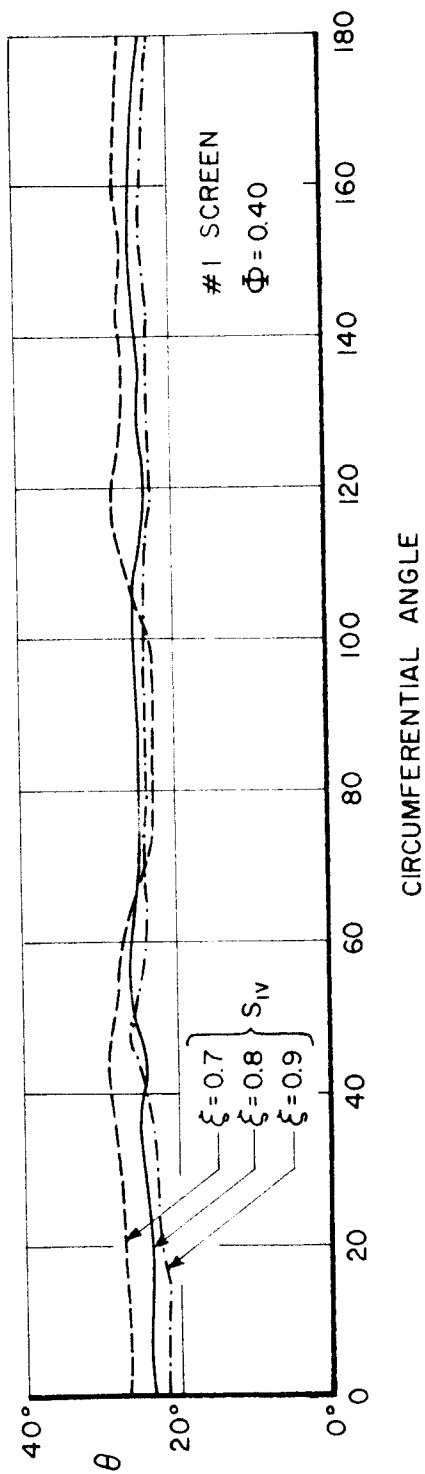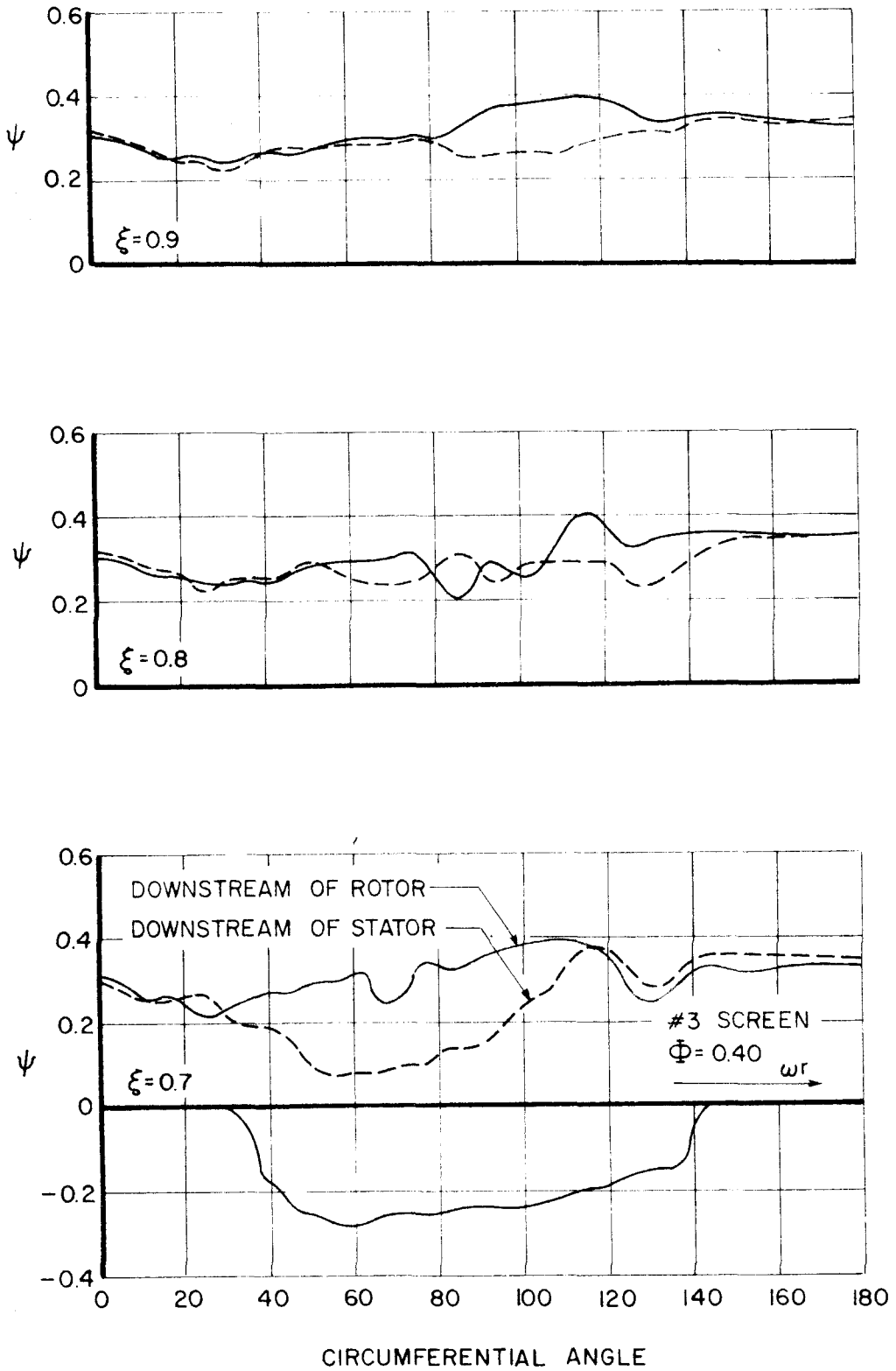Expanded Single Stage Configuration.
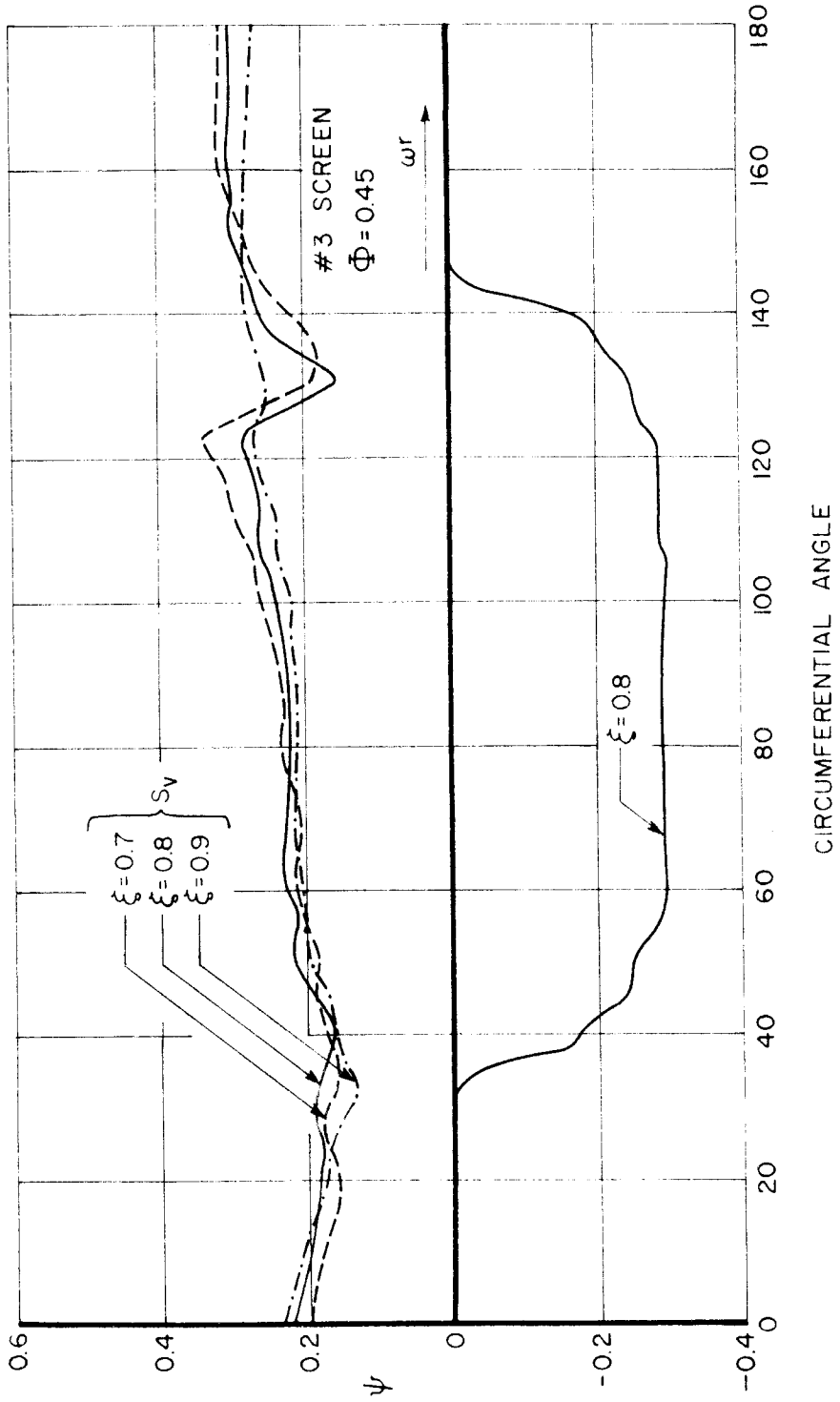
Fig. 36. Total Pressure Survey Downstream of the Rotor.
Expanded Single Stage Configuration.
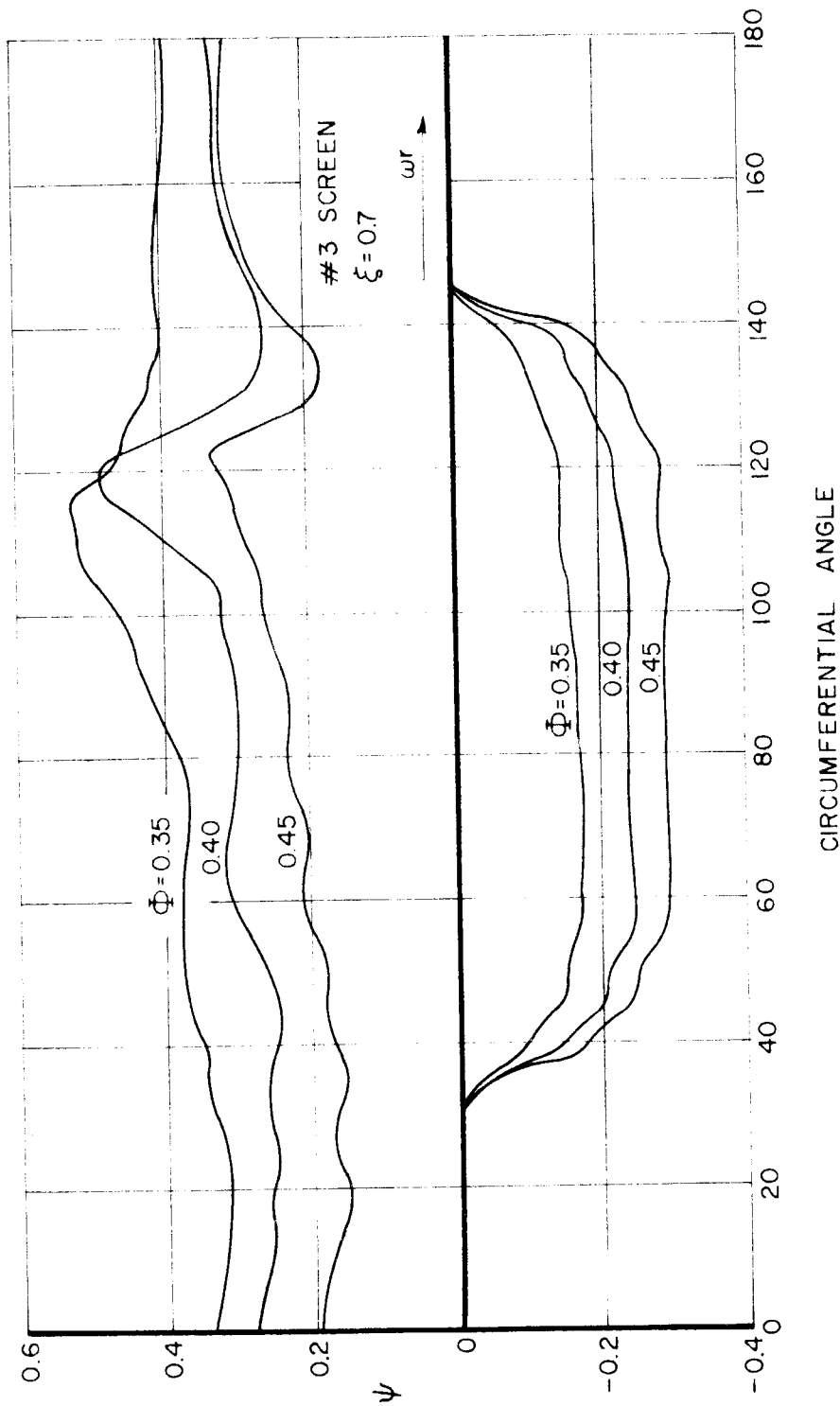
Fig. 37. Variation of the Total Pressure with the Flow Coefficient Downstream
of the Rotor. Expanded Single Stage Configuration.

Fig. 38. Variation of the Total Pressure with the Flow Coefficient Downstream
of the Rotor. Expanded Single Stage Configuration.

CIRCUMFERENTIAL ANGLE
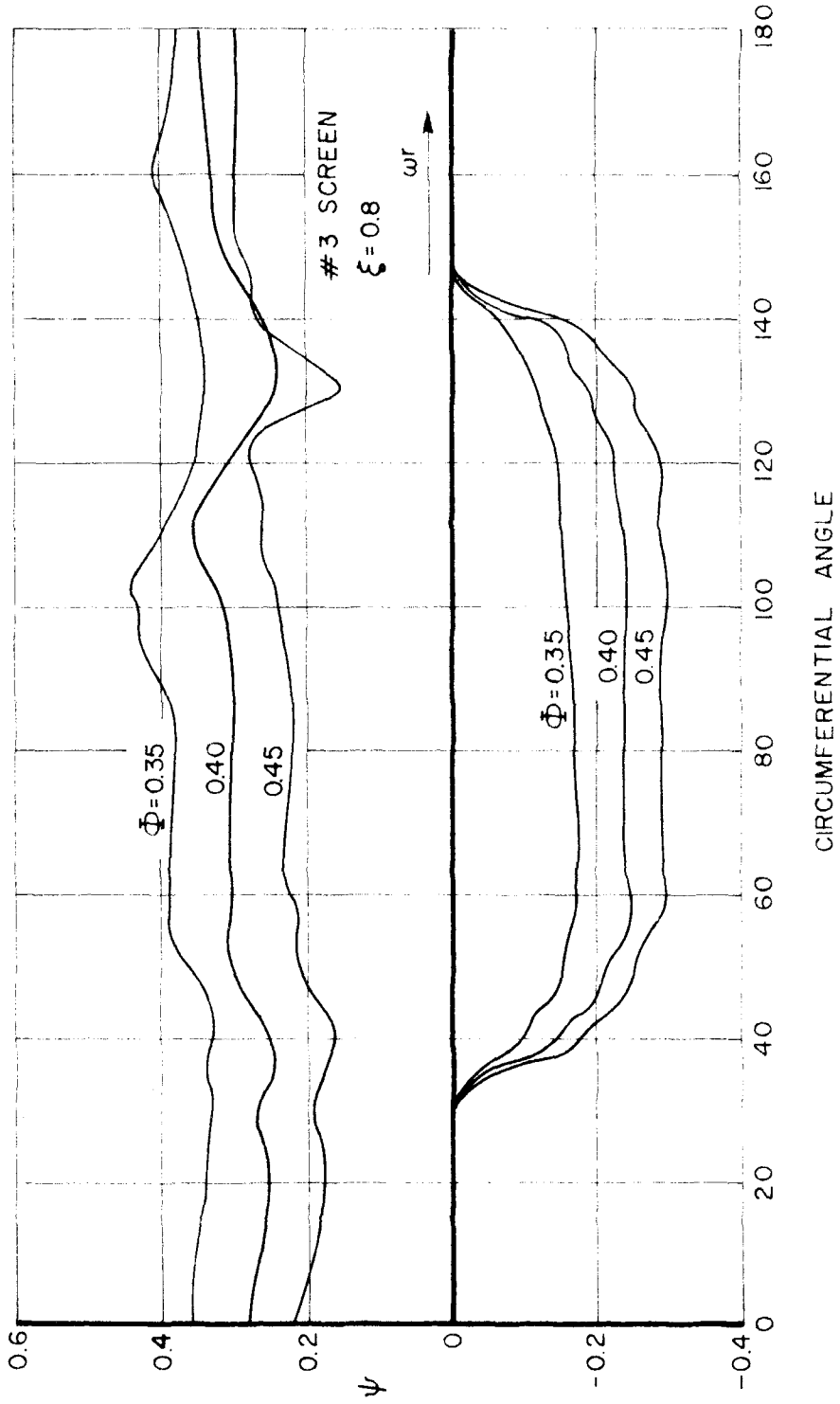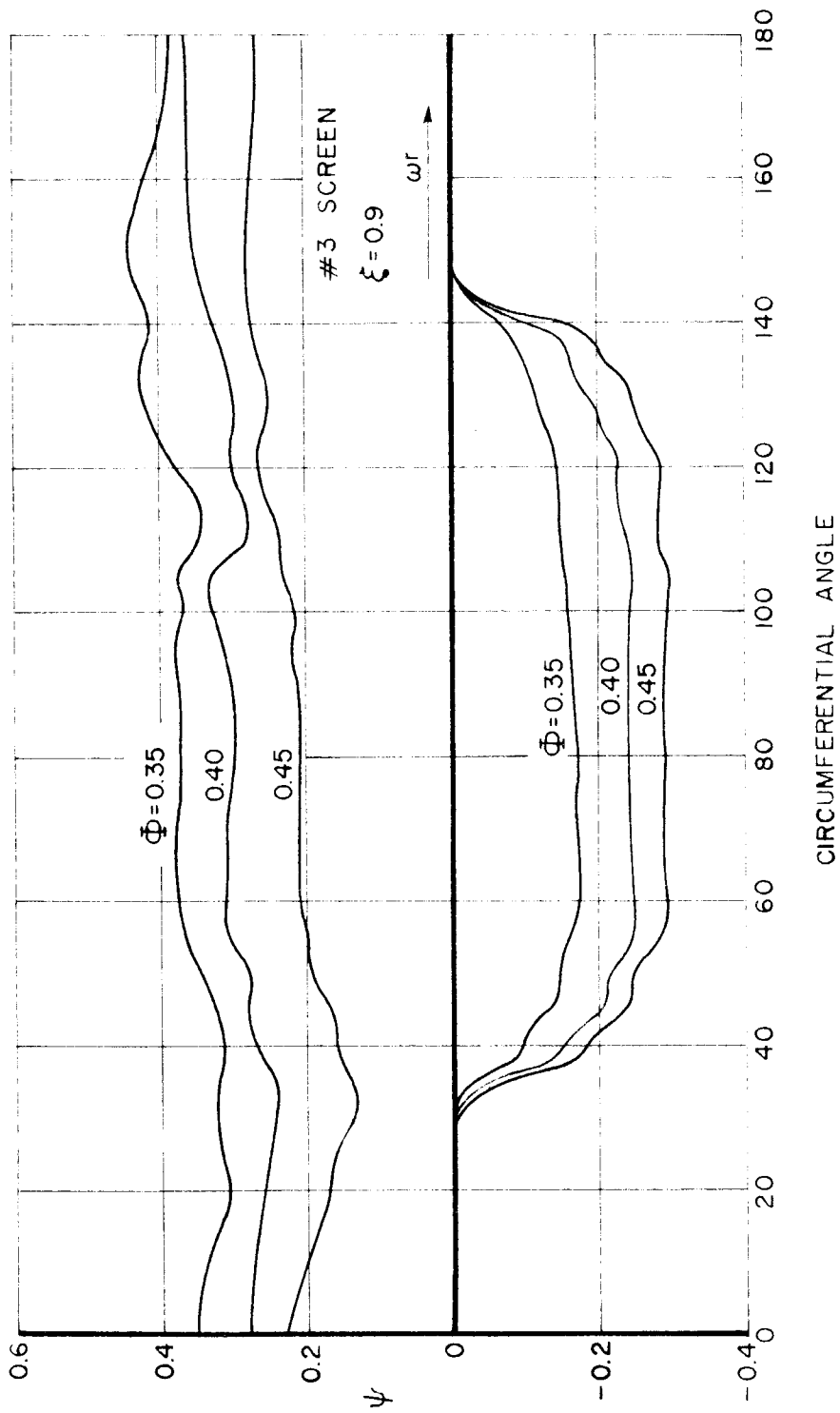
Fig. 39. Variation of the Total Pressure with the Flow Coefficient Downstream

of the Rotor. Expanded Single Stage Configuration.
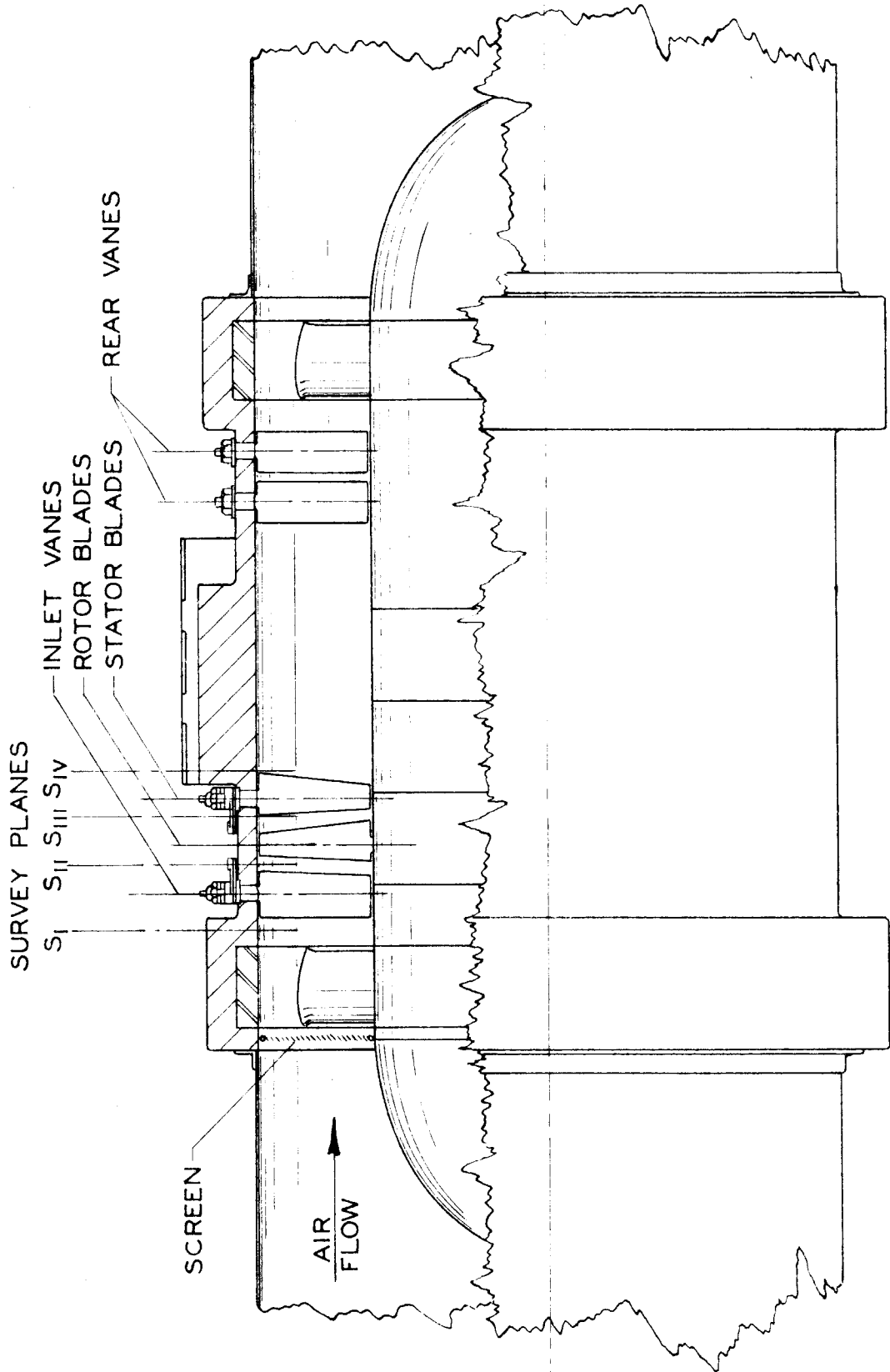
Fig. 40. Normal Single Stage Configuration.

CIRCUMFERENTIAL ANGLE
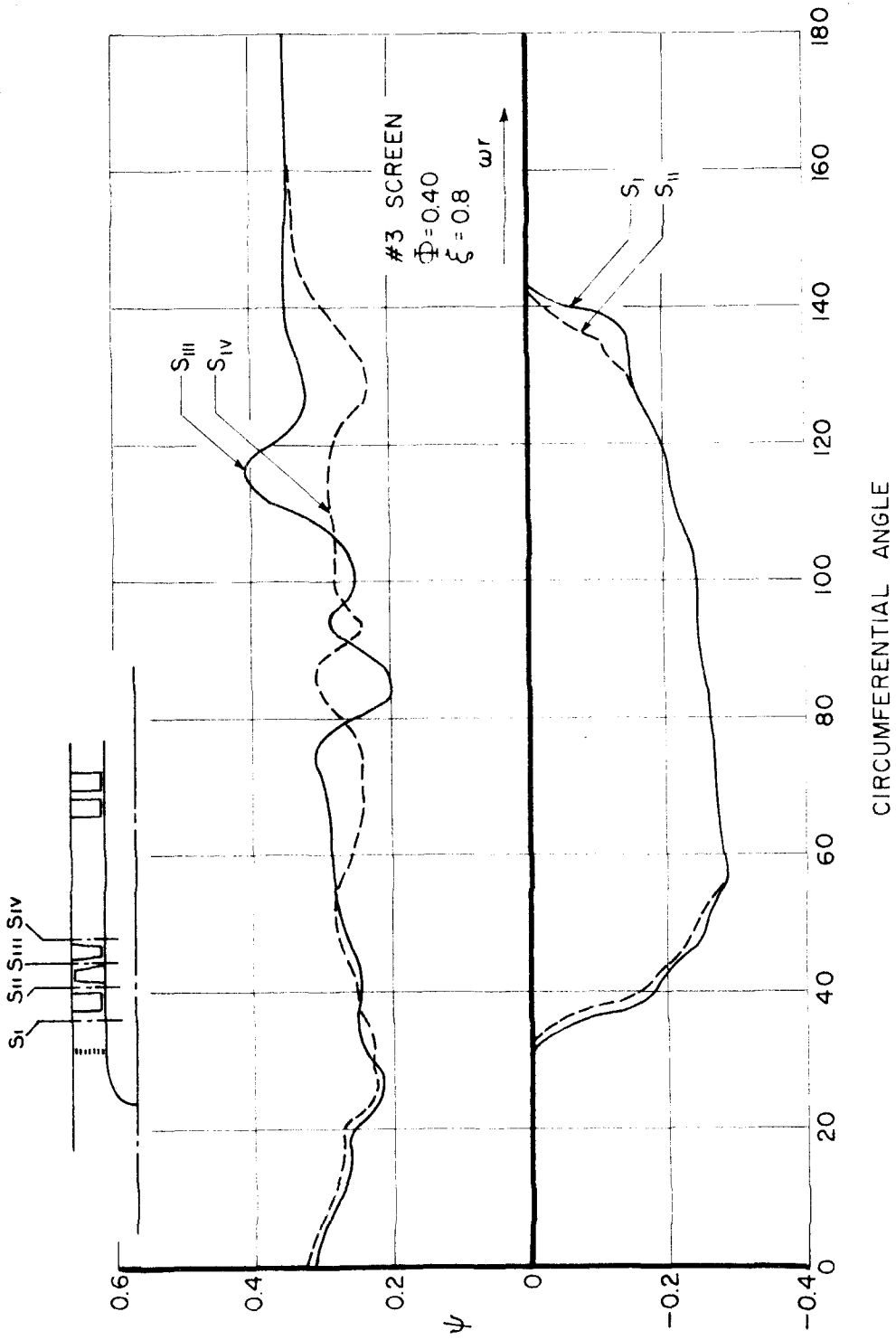
Fig. 41. Total Pressure Survey at the Mean Radius.

Normal Single Stage Configuration.
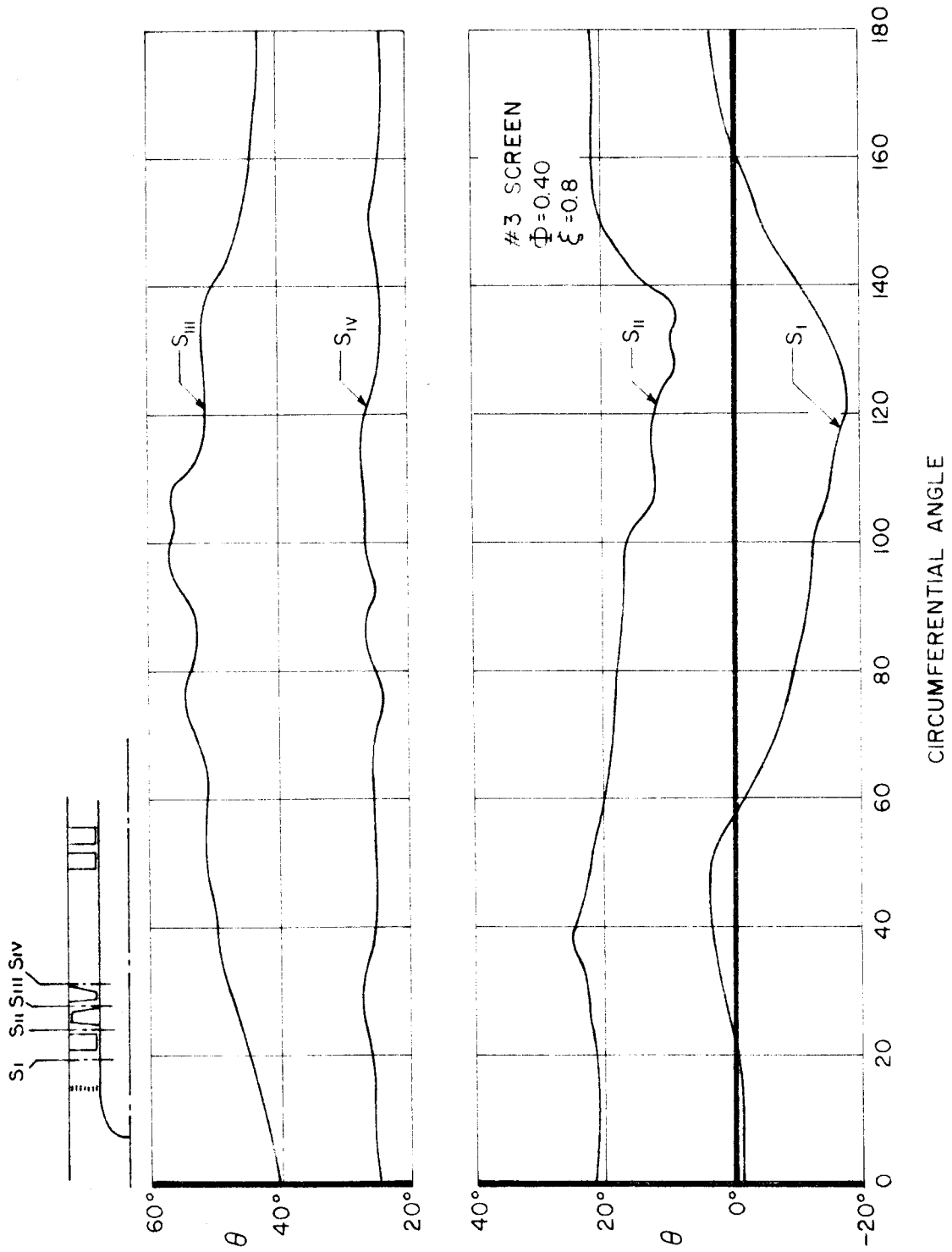
Fig. 42. Flow Angle Survey at the Mean Radius. Normal Single-Stage Configuration.
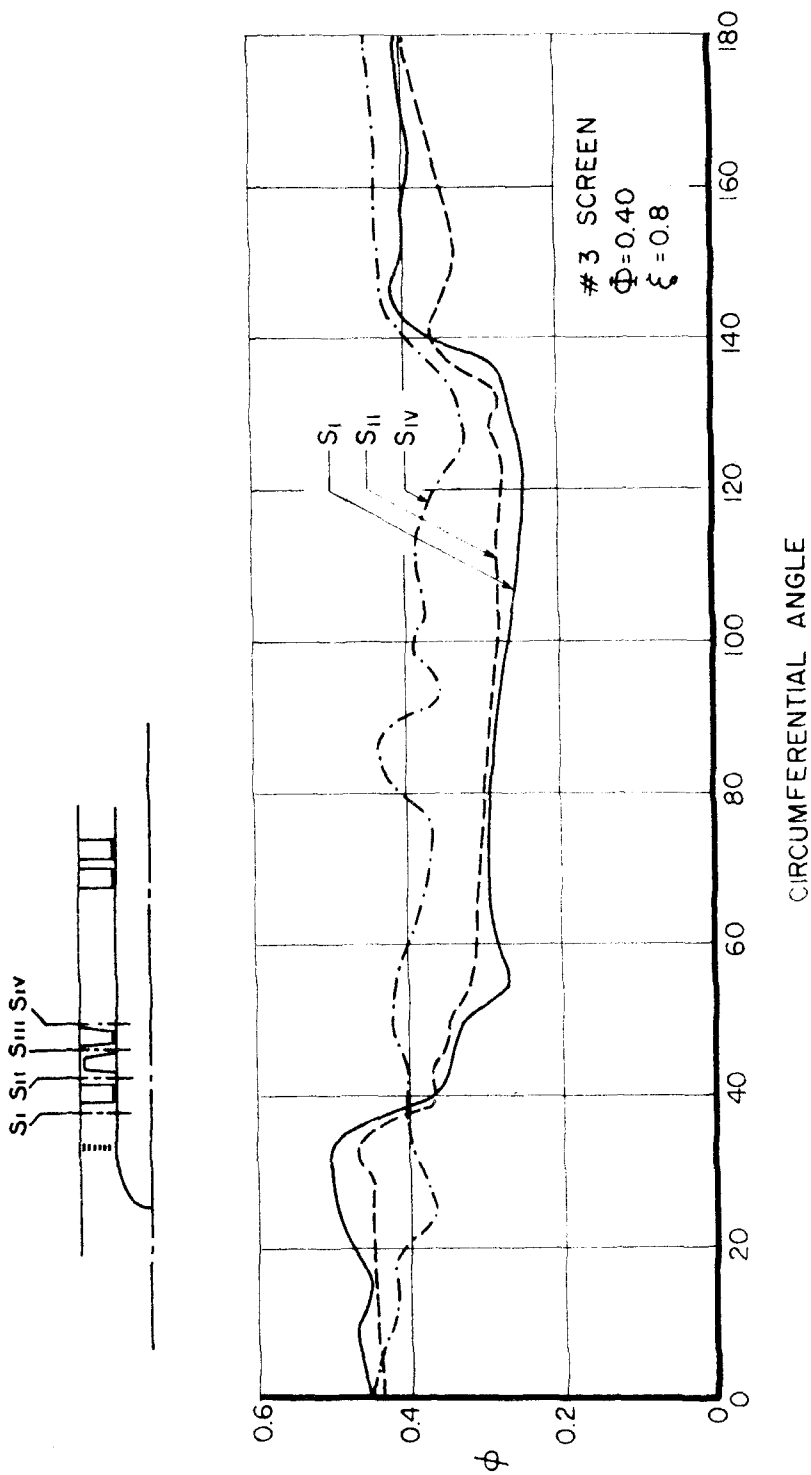
Fig. 43. Flow Coefficient Survey at the Mean Radius.

Normal Single Stage Configuration.
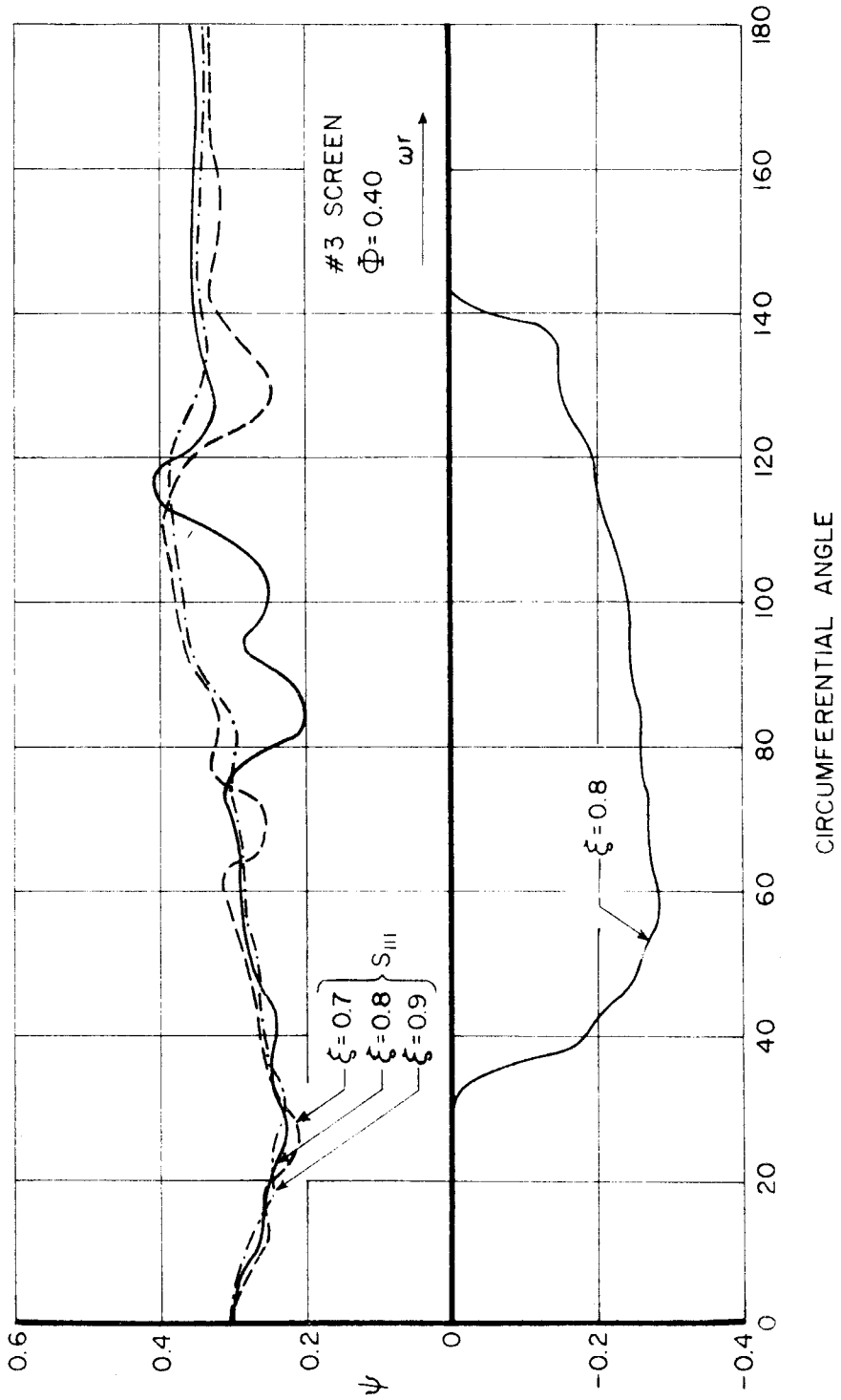
Fig. 44. Total Pressure Survey Downstream of the Rotor.
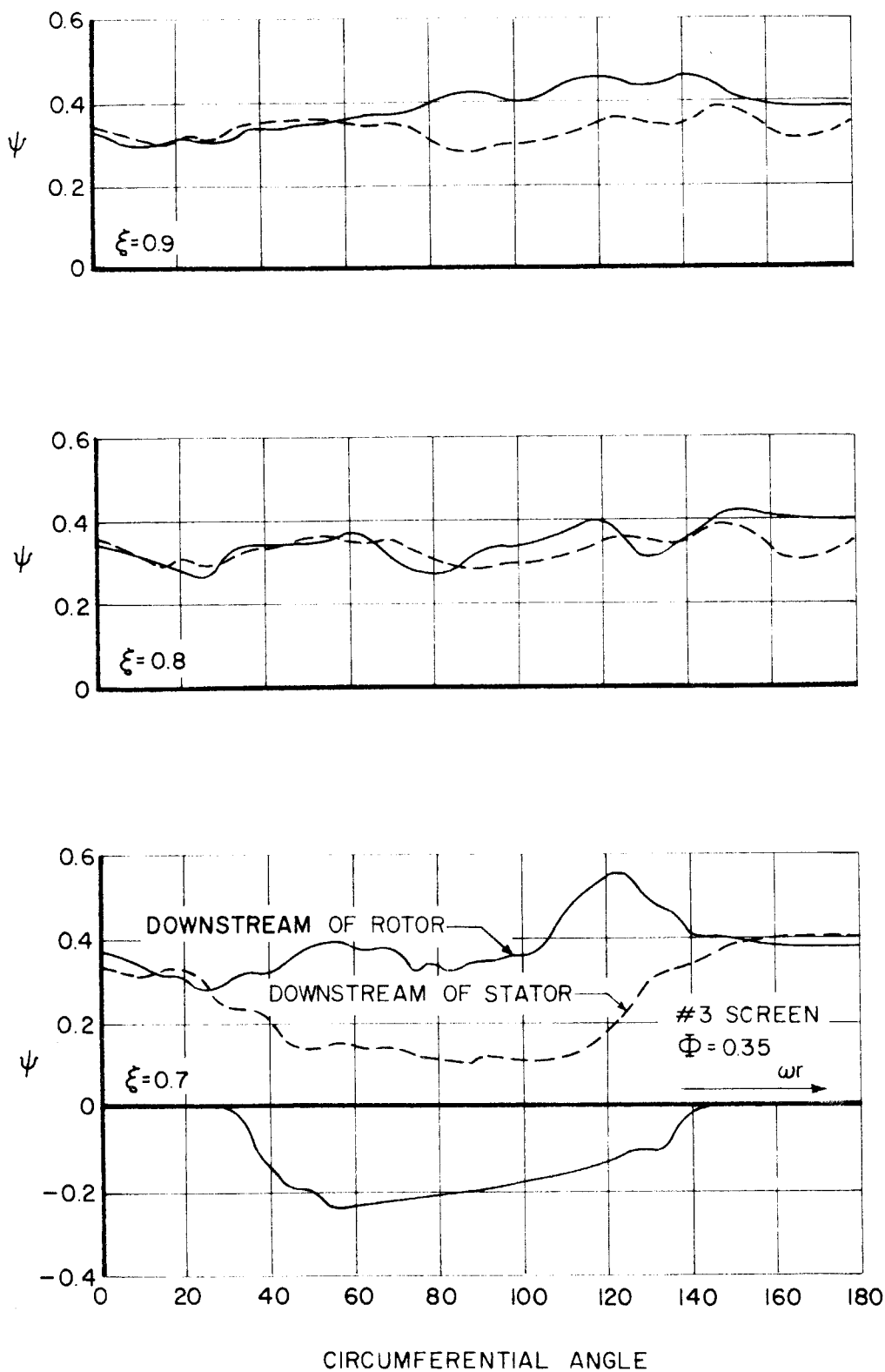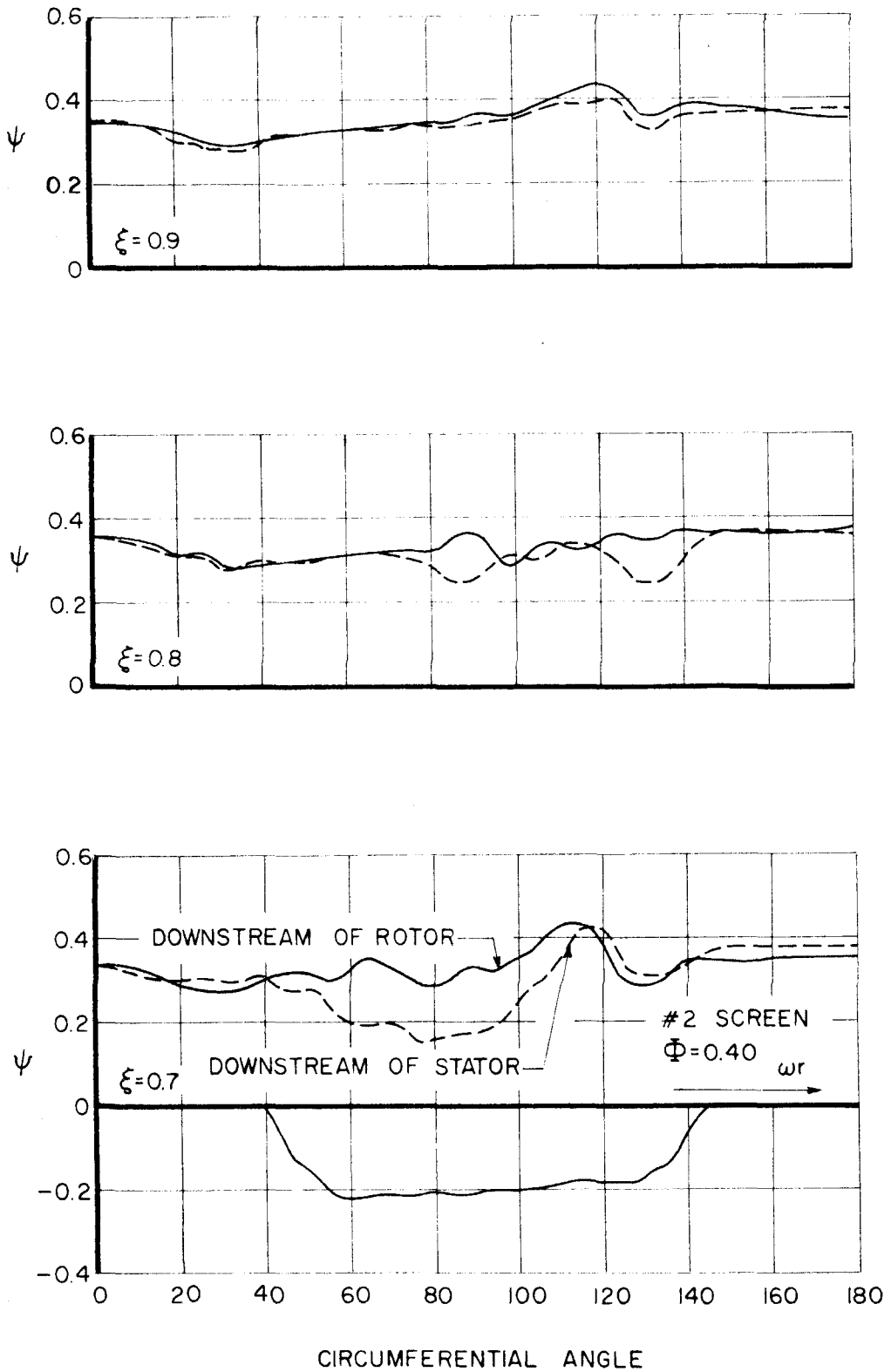
Normal Single Stage Configuration.
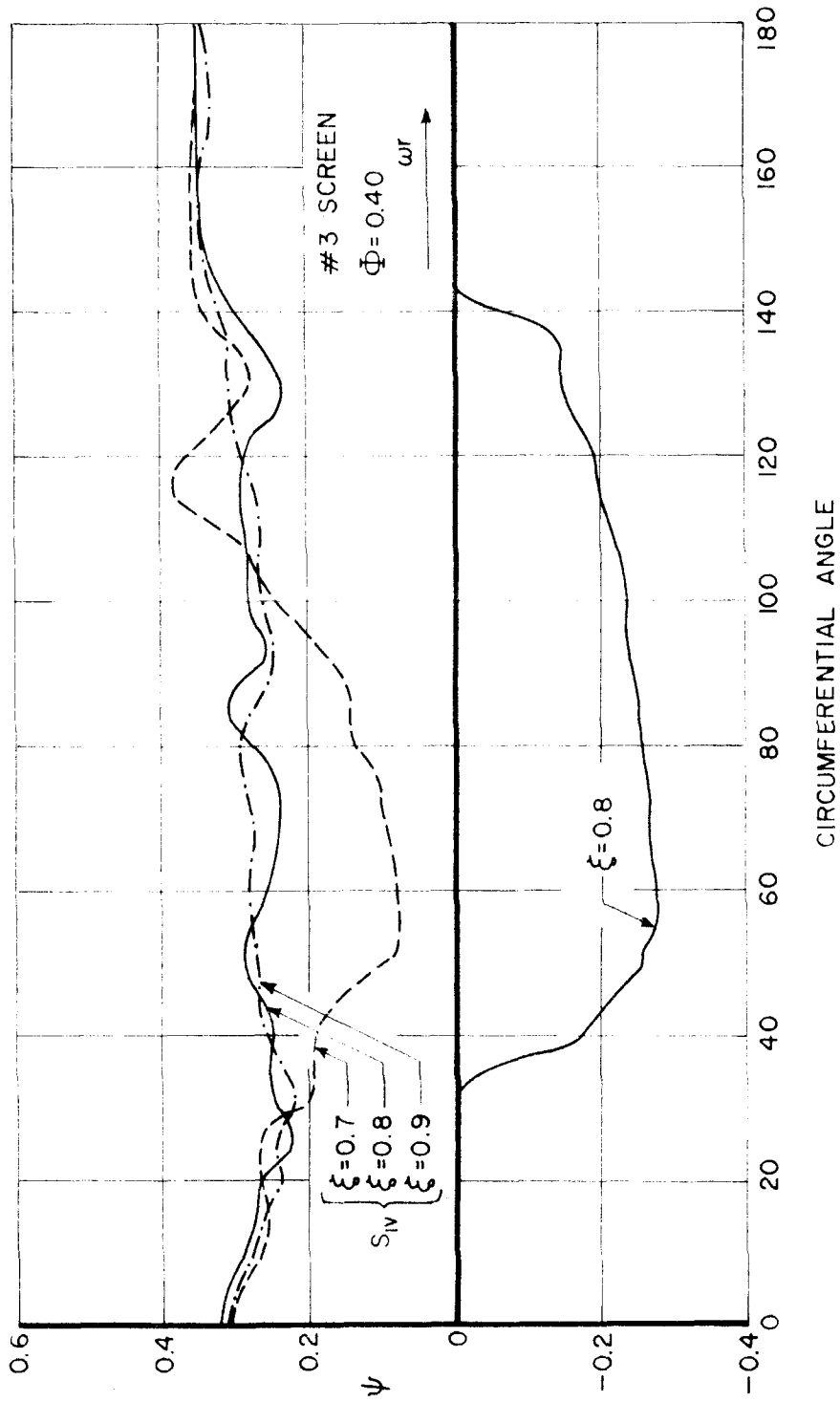
Fig. 45. Total Pressure Survey Downstream of the Stator.

Normal Single Stage Configuration.
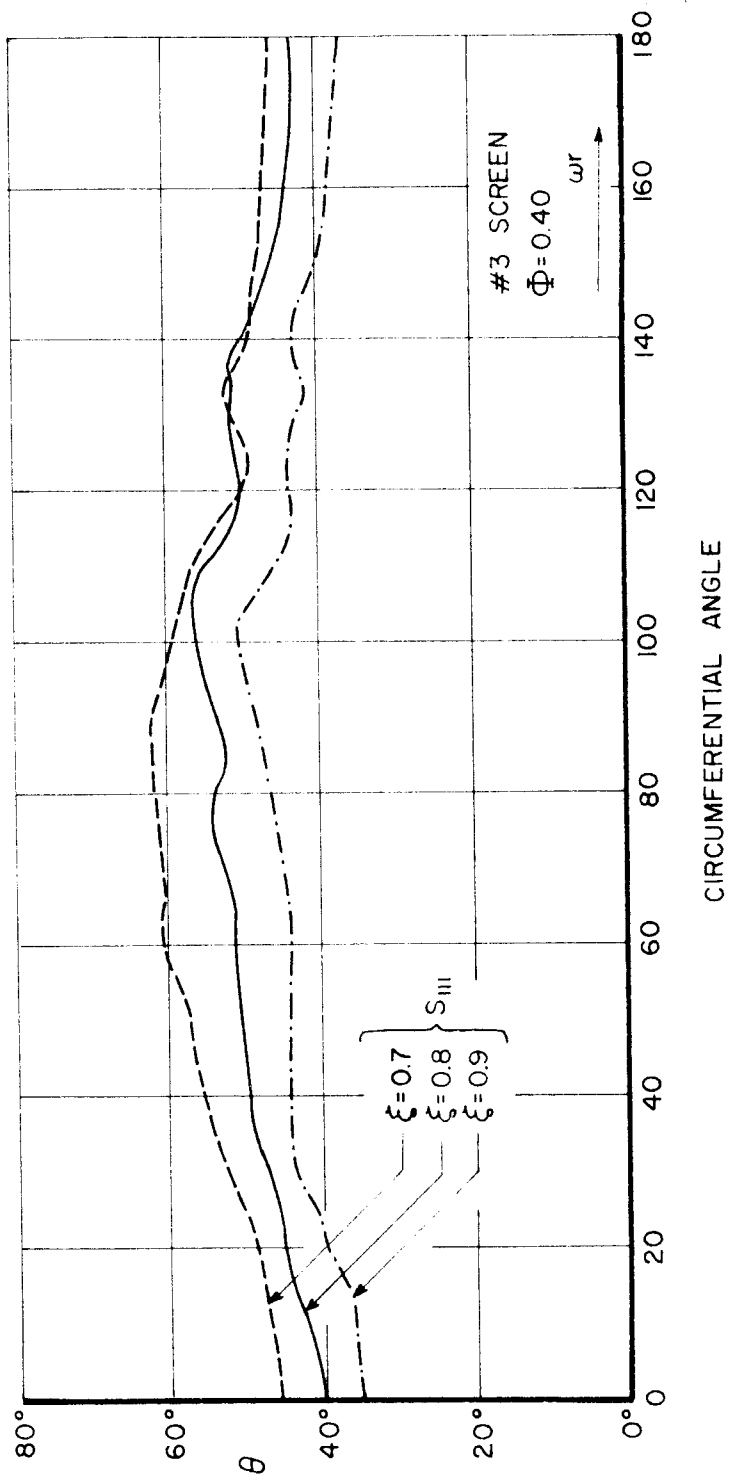
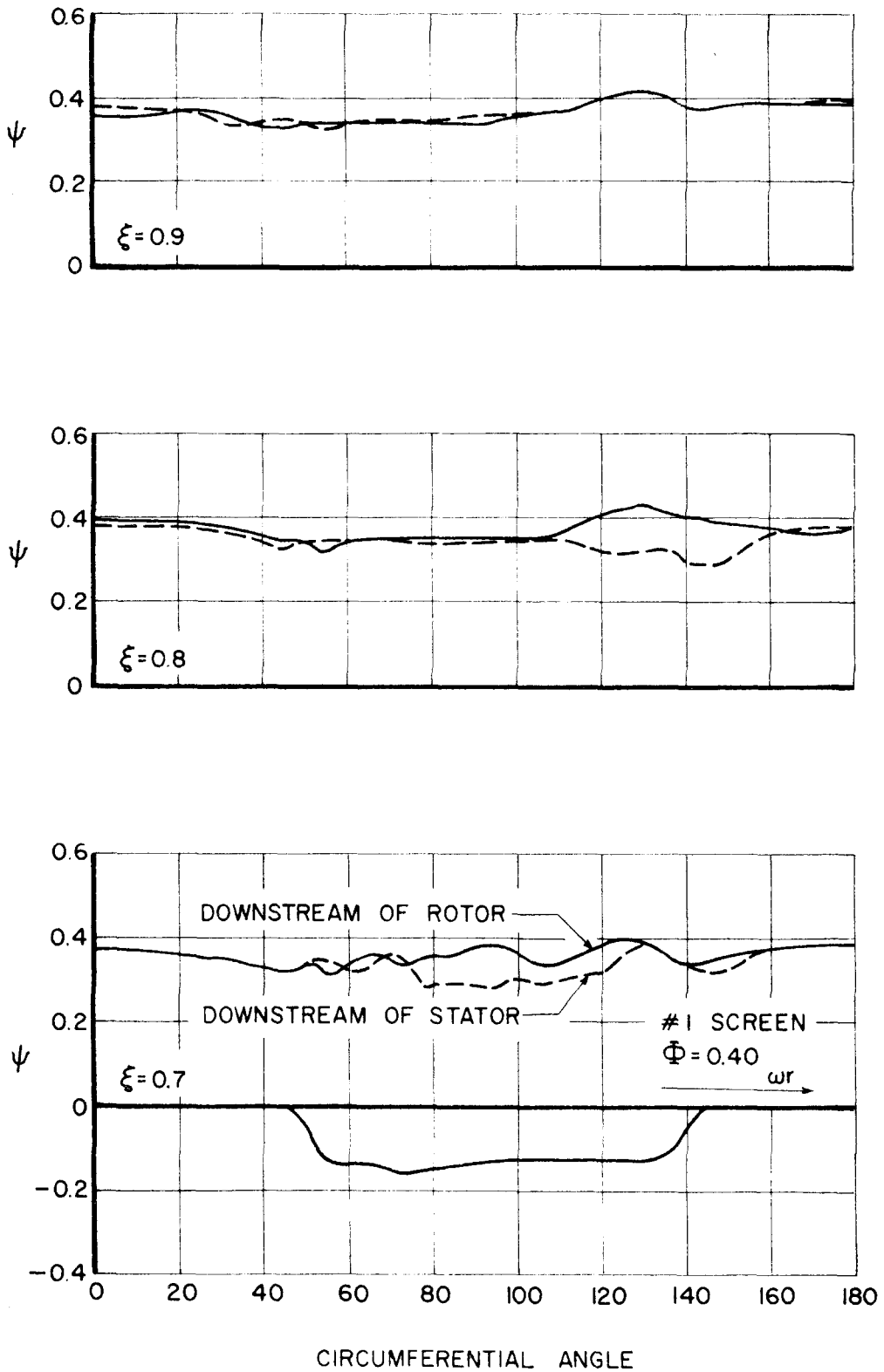Fig. 46. Flow Angle Survey Downstream of the Rotor.
Normal Single Stage Configuration.
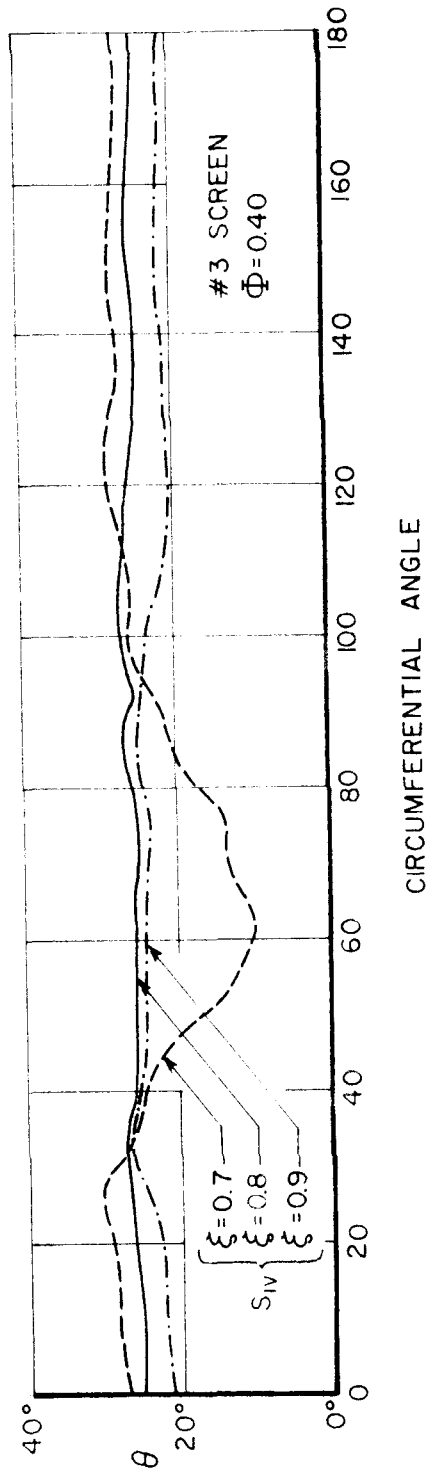
Fig. 47. Flow Angle Survey Downstream of the Stator.
Normal Single Stage Configuration.
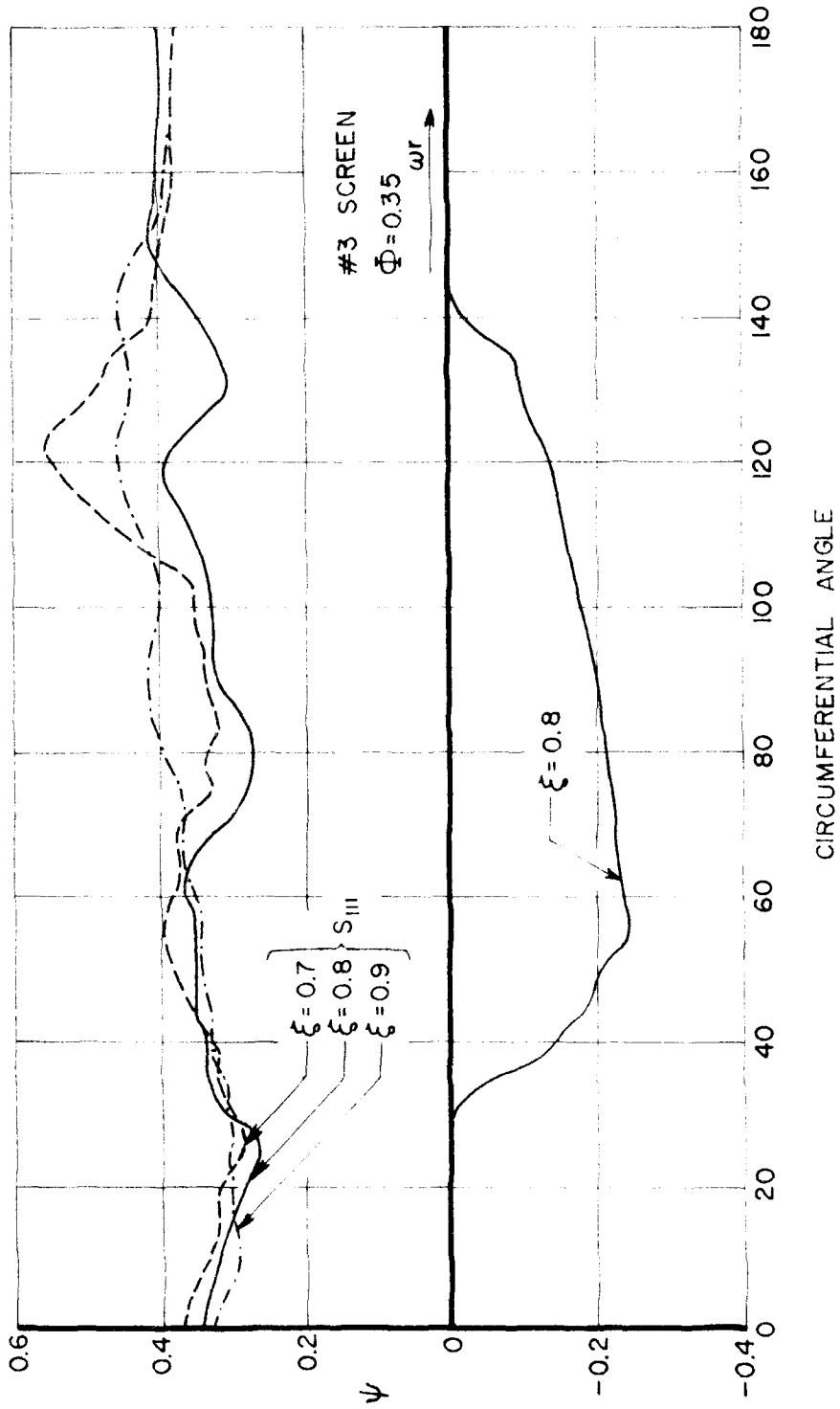
Fig. 48. Total Pressure Survey Downstream of the Rotor.

Normal Single Stage Configuration.
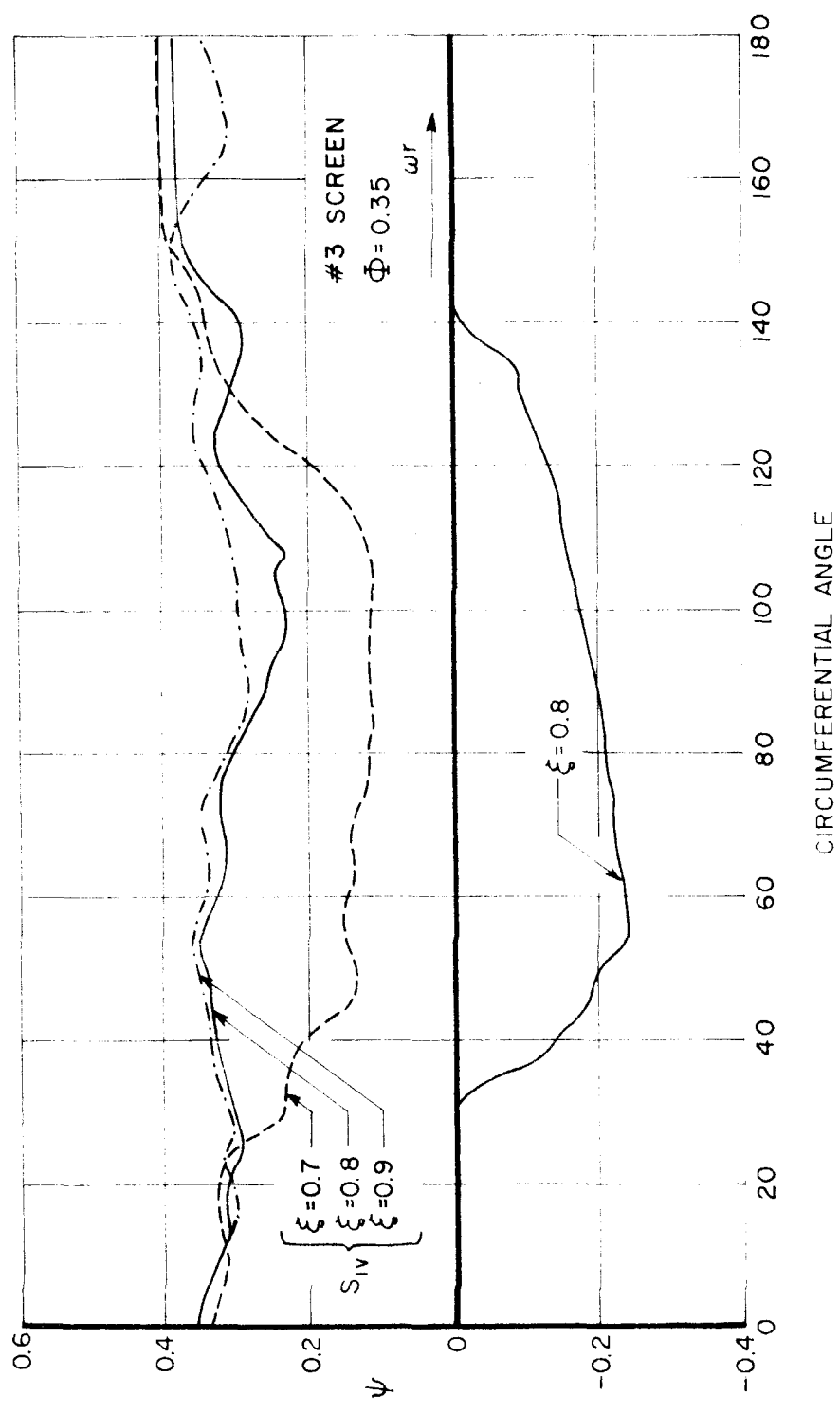
Fig. 49. Total Pressure Survey Downstream of the Stator.

Normal Single Stage Configuration.
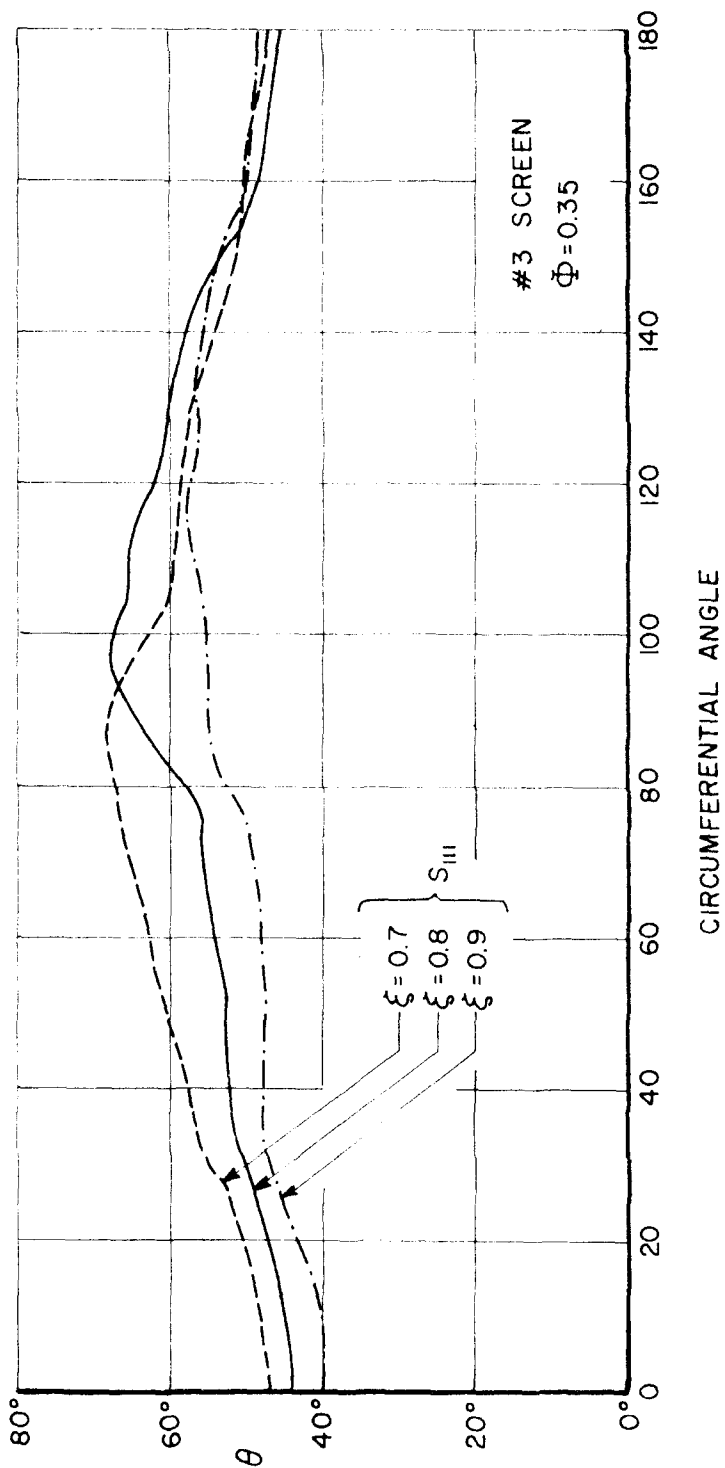
Fig. 50. Flow Angle Survey Downstream of the Rotor.

Normal Single Stage Configuration.
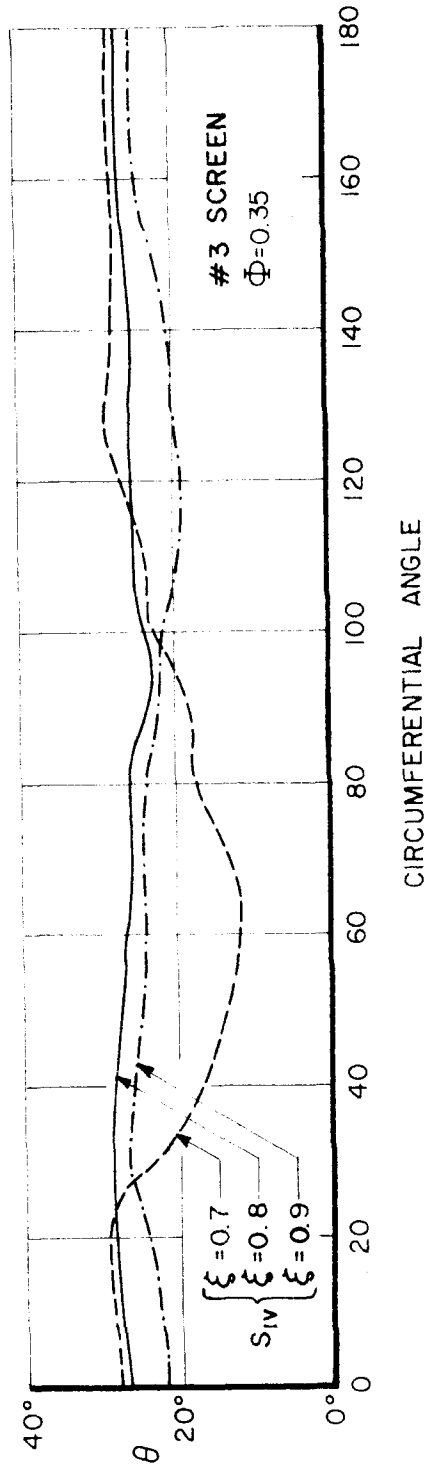
Fig. 51. Flow Angle Survey Downstream of the Stator.

Normal Single Stage Configuration.
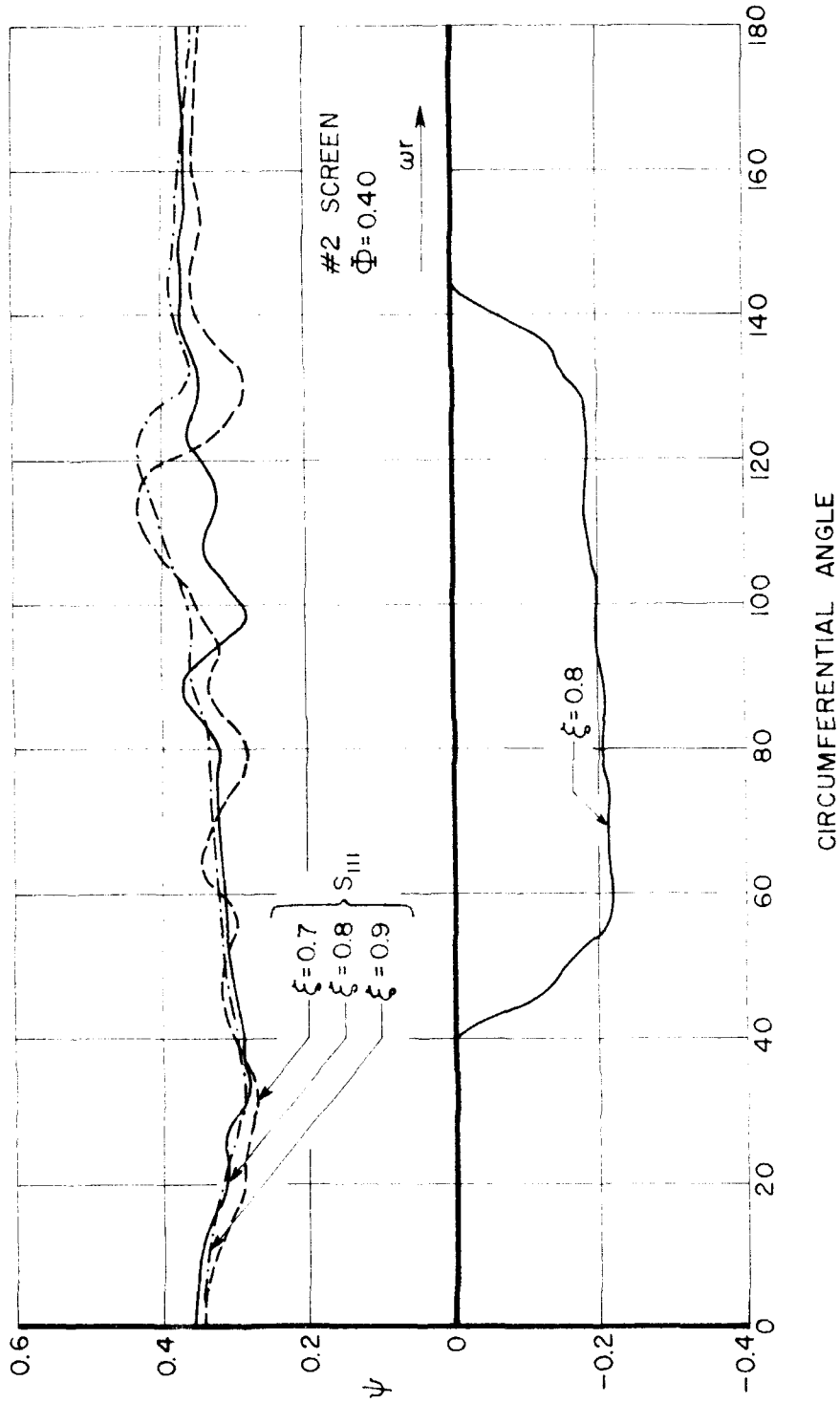
Fig. 52. Total Pressure Survey Downstream of the Rotor.

Normal Single Stage Configuration.
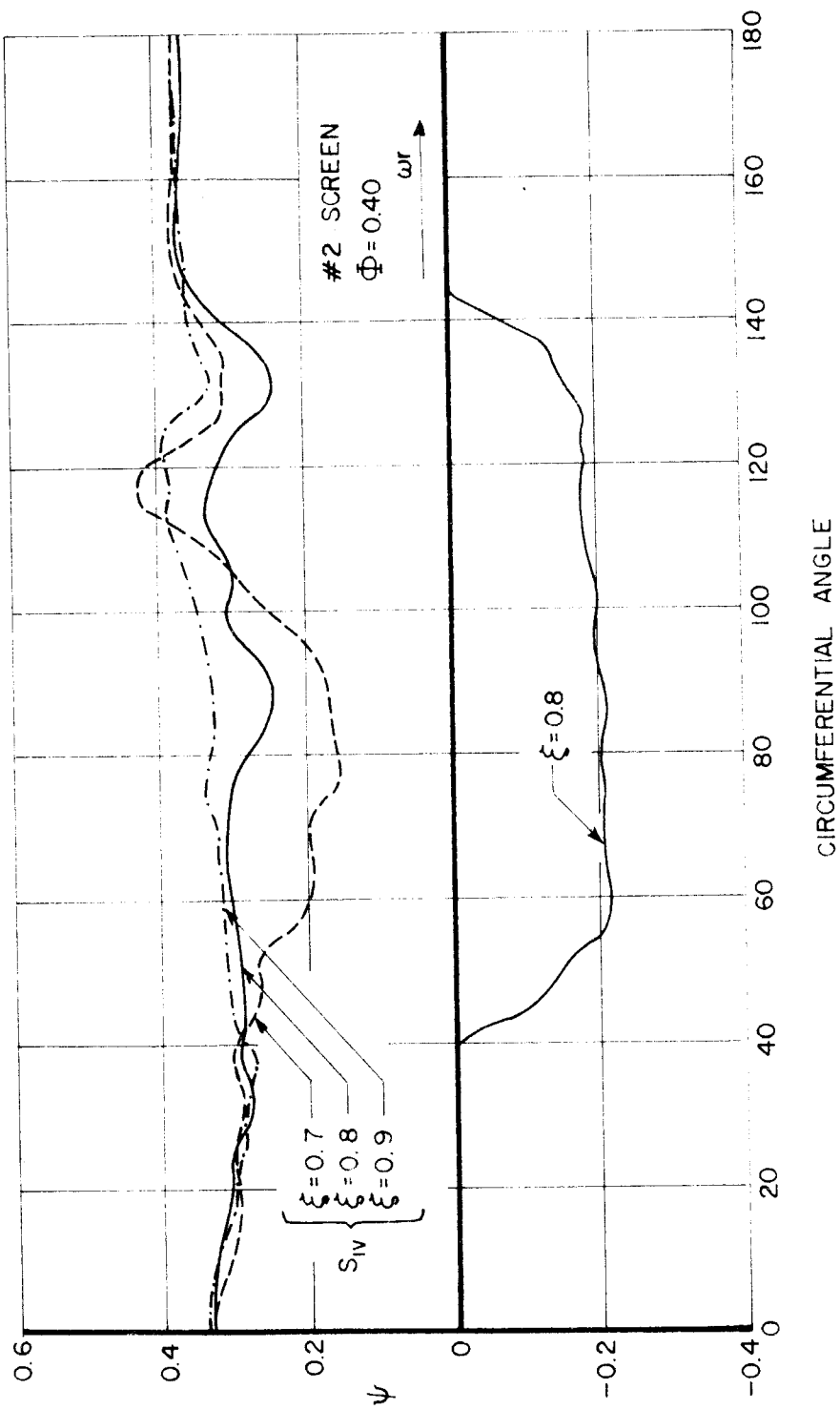
Fig. 53. Total Pressure Survey Downstream of the Stator.

Normal Single Stage Configuration.
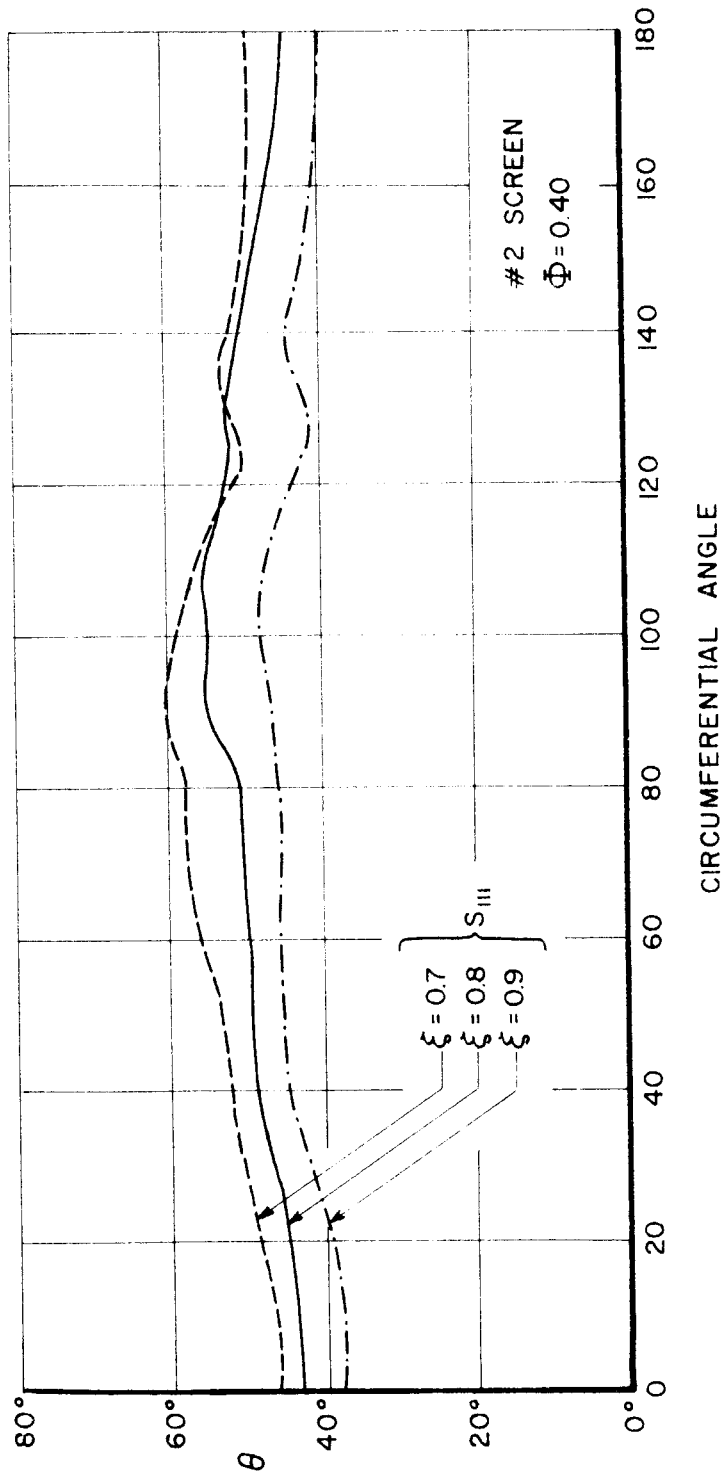
Fig. 54. Flow Angle Survey Downstream of the Rotor
Normal Single Stage Configuration.
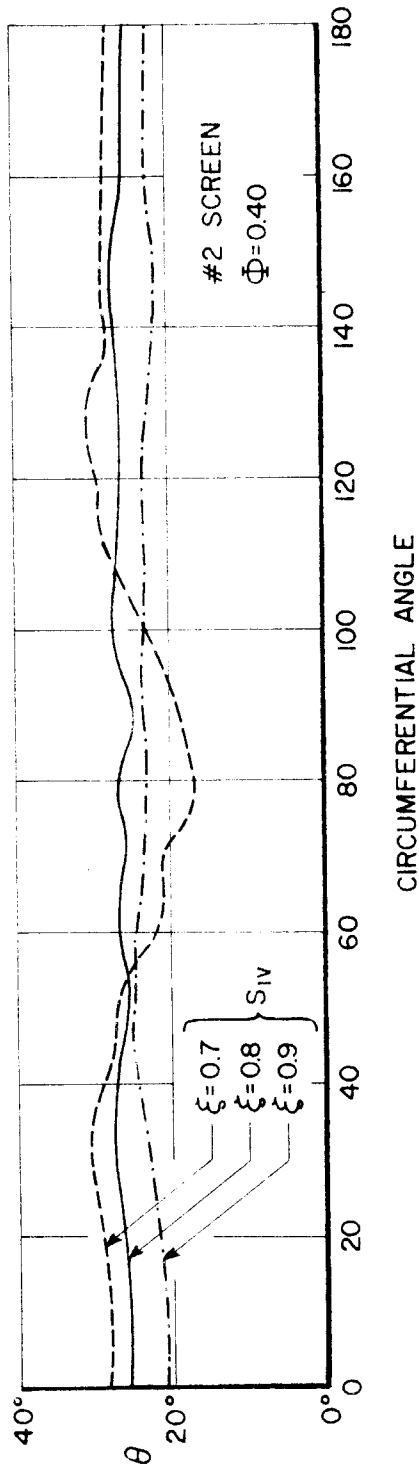
Fig. 55. Flow Angle Survey Downstream of the Stator.
Normal Single Stage Configuration.

CIRCUMFERENTIAL ANGLE
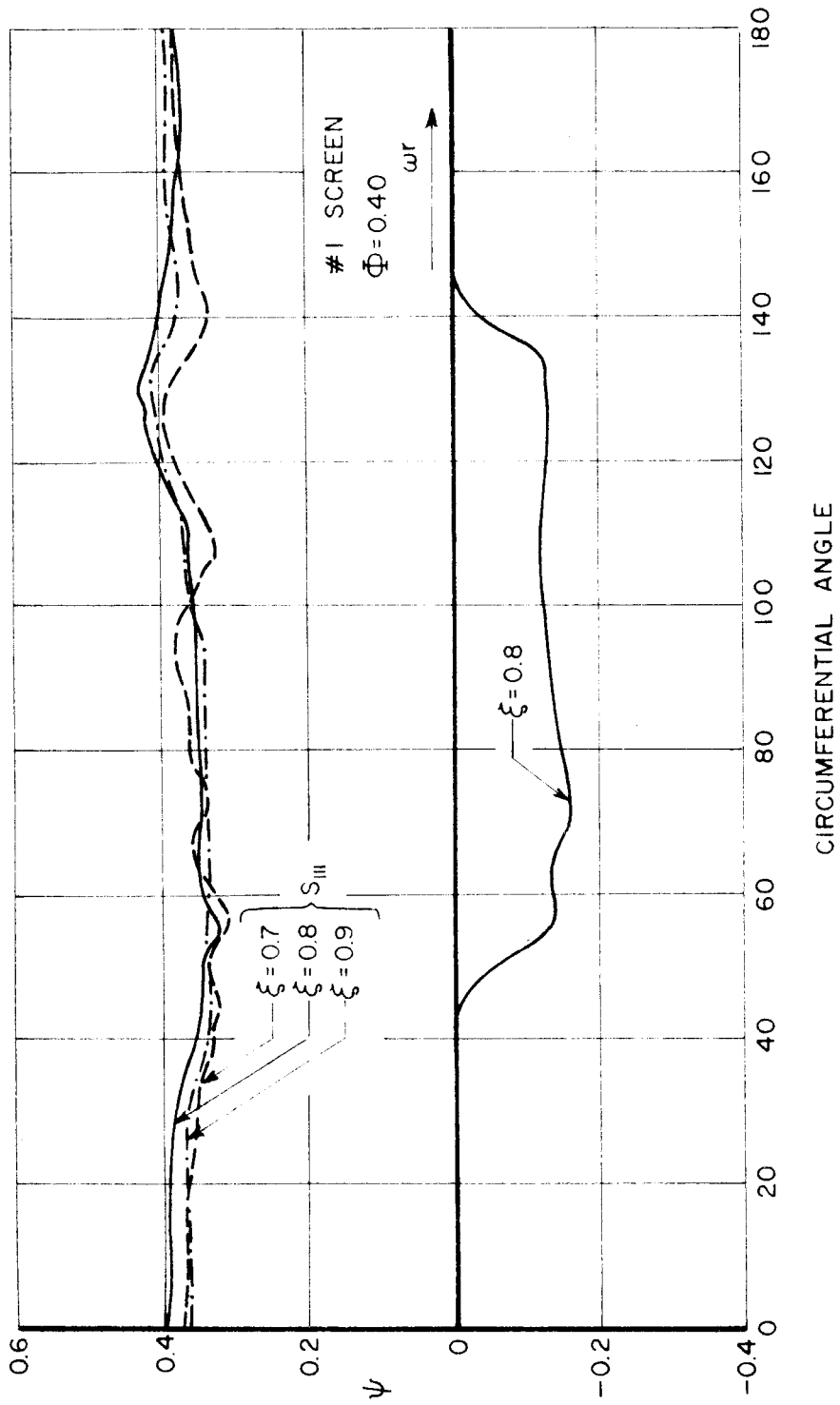
Fig. 56. Total Pressure Survey Downstream of the Rotor.
Normal Single Stage Configuration.

-130-
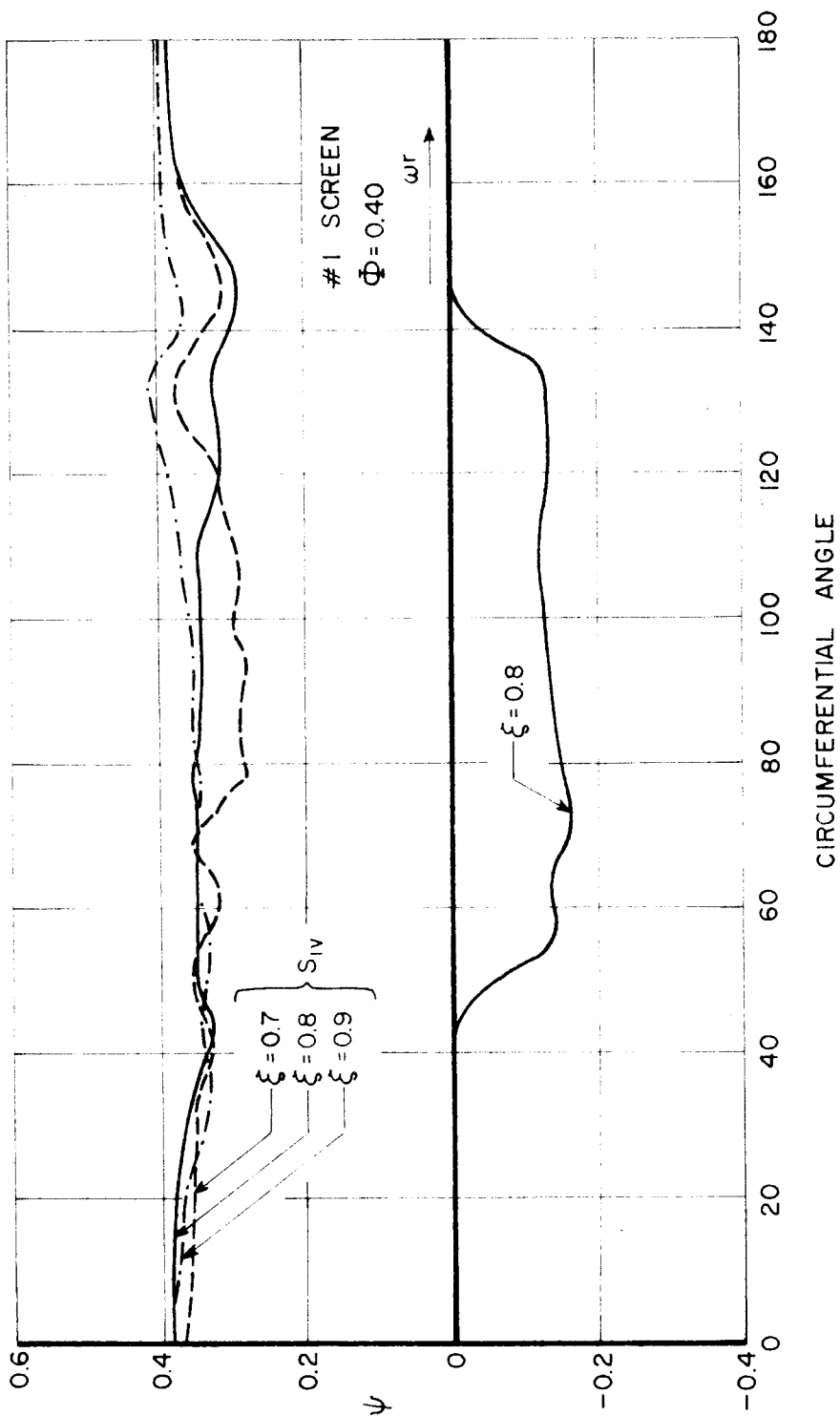
Fig. 57. Total Pressure Survey Downstream of the Stator.

Normal Single Stage Configuration.

Fig. 58. Flow Angle Survey Downstream of the Rotor.
Normal Single Stage Configuration.

Fig. 59. Flow Angle Survey Downstream of the Stator.

Normal Single Stage Configuration.

Fig. 60. Total Pressure Surveys Downstream of the Rotor and Stator.
Normal Single Stage Configuration.

Fig. 61. Total Pressure Surveys Downstream of the Rotor and
Stator. Normal Single Stage Configuration.

Fig. 62. Total Pressure Surveys Downstream of the Rotor and Stator. Normal Single Stage Configuration.

Fig. 63. Total Pressure Surveys Downstream of the Rotor and Stator. Normal Single Stage Configuration.
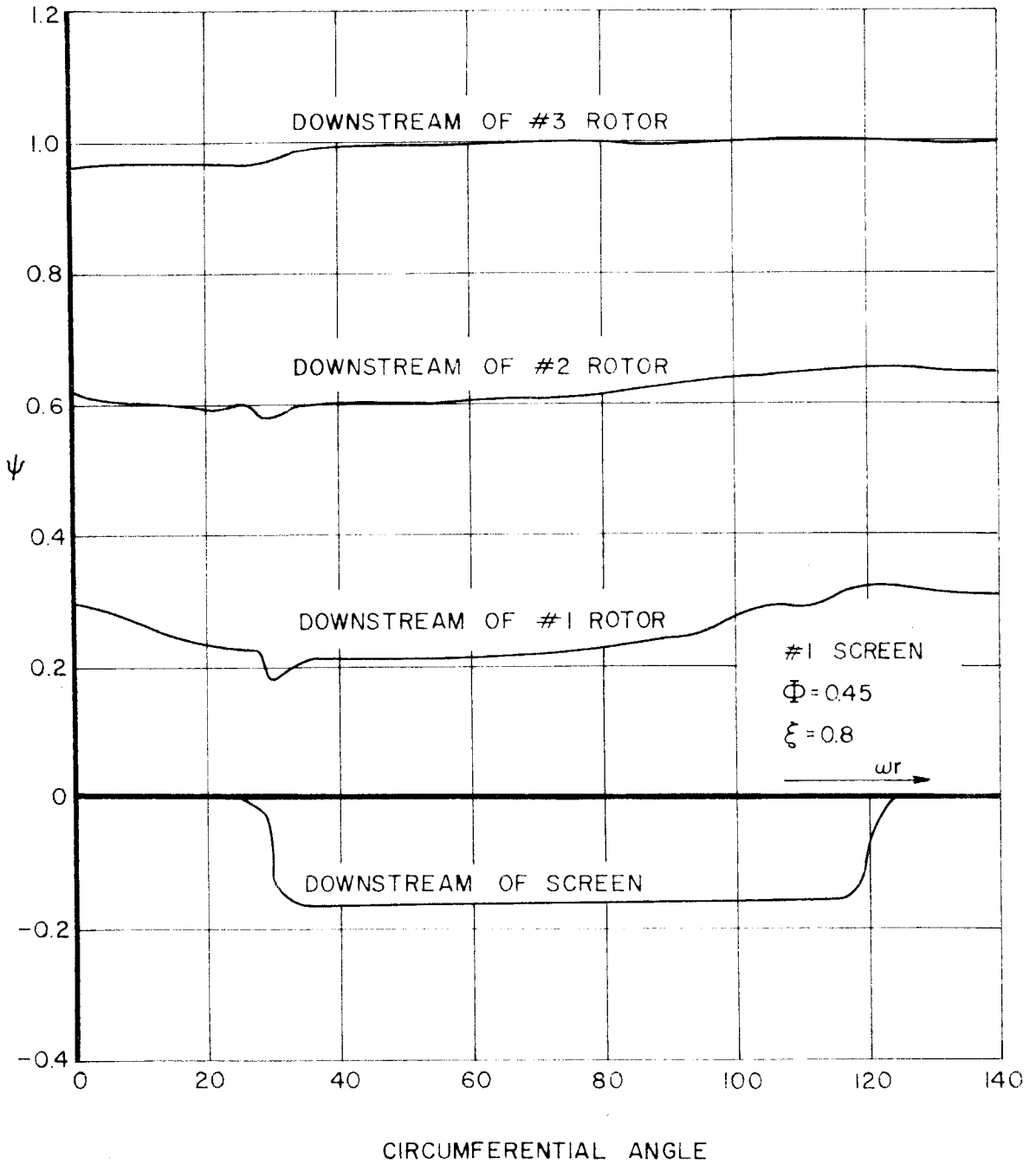
Fig. 64. Total Pressure Survey. Three Stage Configuration.

Fig. 65. Total Pressure Survey. Three Stage Configuration.

.021 D. 4 HOLES

THERMOCOUPLE JUNCTION

$\frac{3}{8}$

$\frac{3}{32}$D.

.015 D. NICHROME WIRE

$\frac{3}{8}$

$\frac{1}{8}$D.

MILLIAMMETER

GALVANOMETER

N.O.

N.O.

N.O.

N.C.
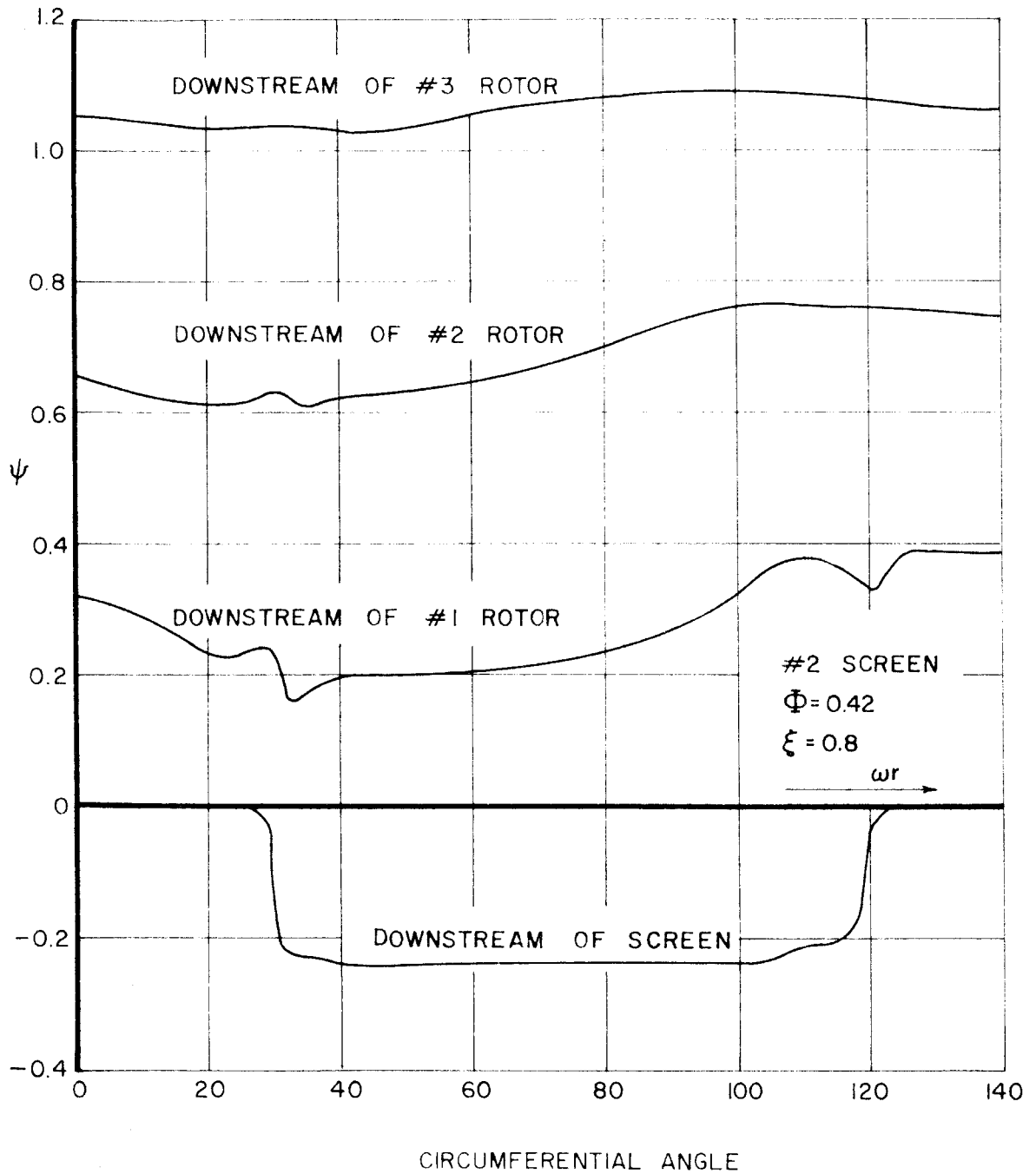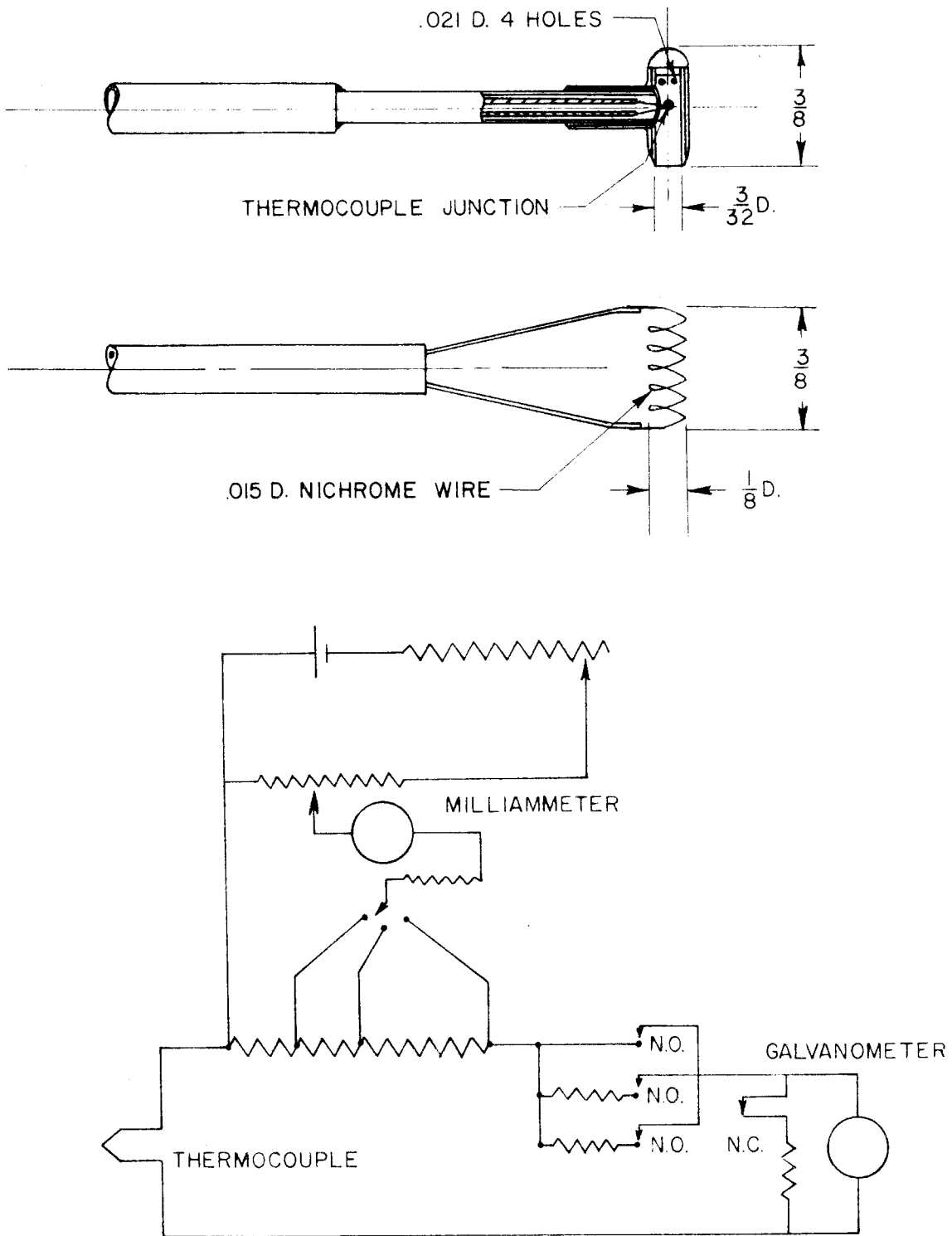
THERMOCOUPLE

Fig. 66. Total Temperature Probe, Heater Probe, and Thermocouple Balancing Circuit.
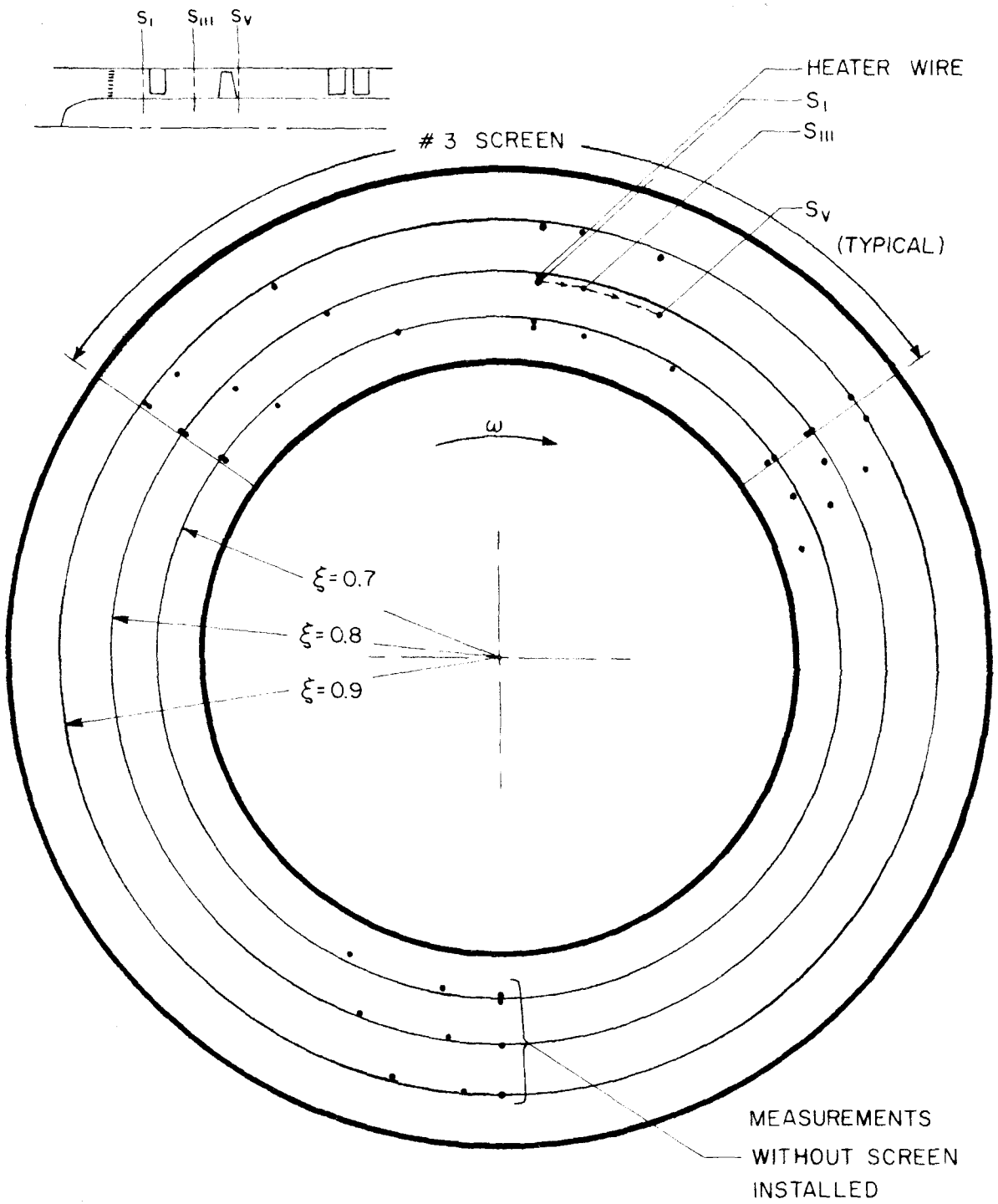
Fig. 67. Streamline Paths as Viewed in the Direction of the Flow.

Inlet Vanes - Second Rotor Configuration, $\bar{\phi} = 0.40$.
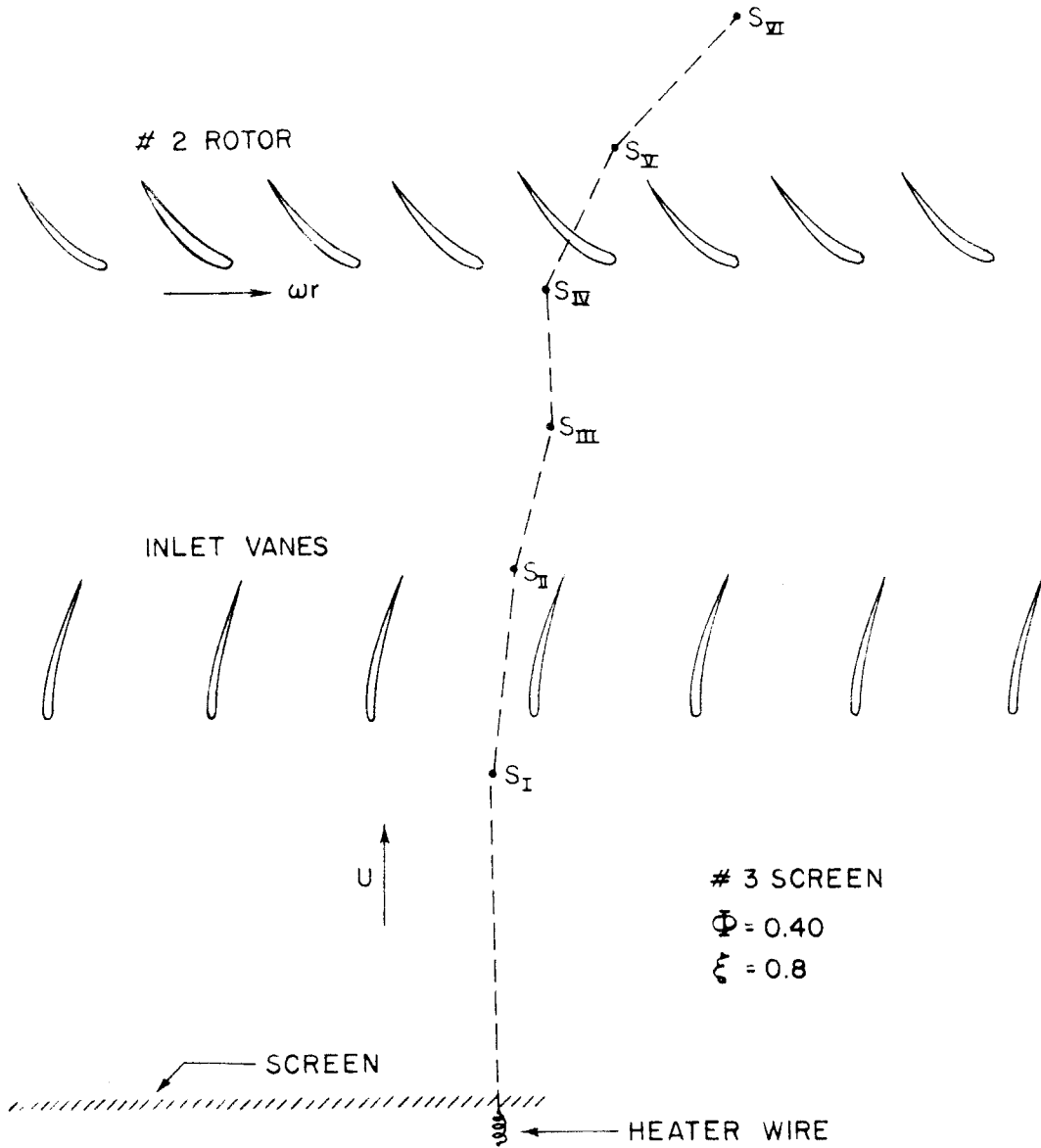
Fig. 68. Two-Dimensional View of a Streamline Path.
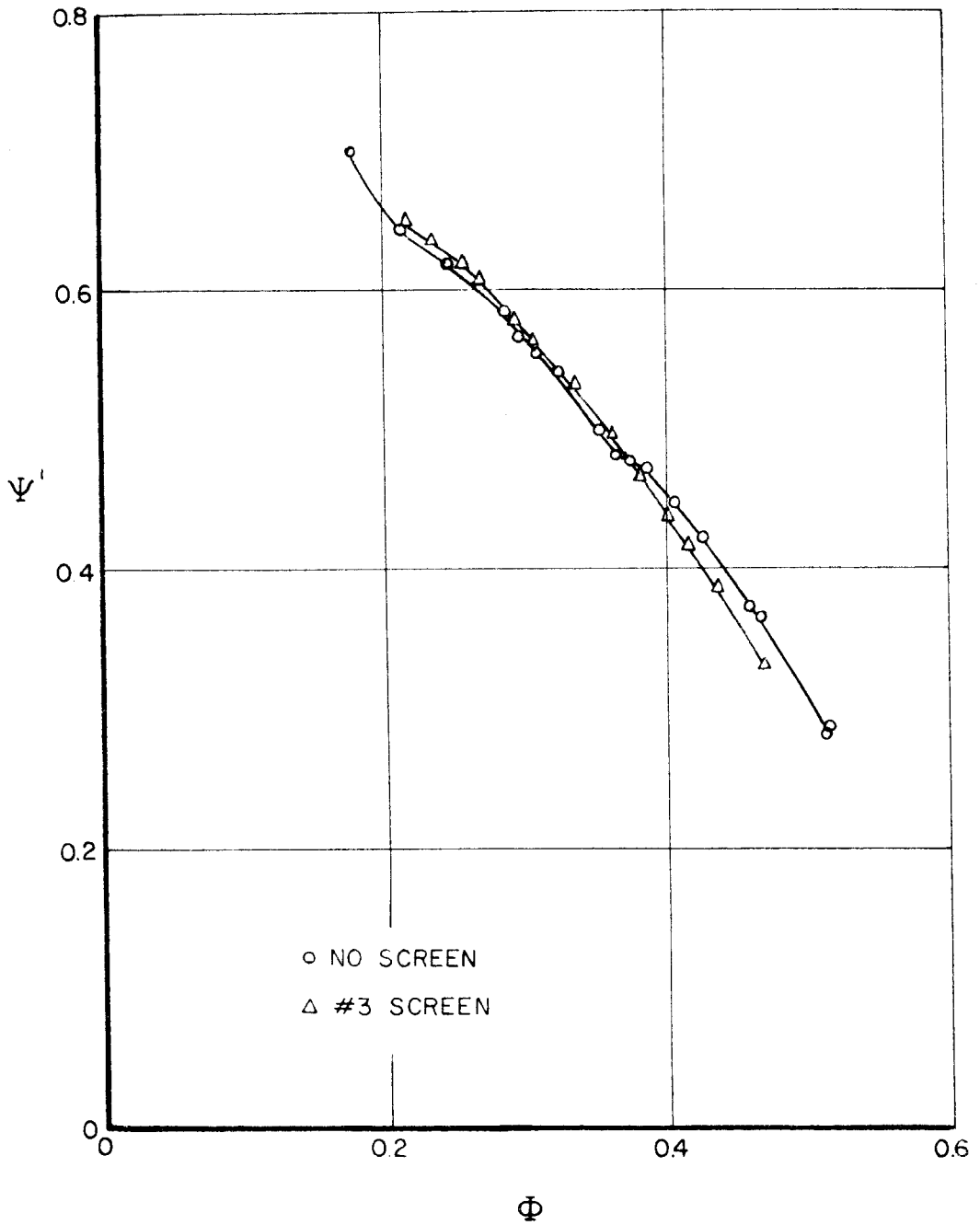
Fig. 69. Work Coefficient. Expanded Single Stage Configuration.
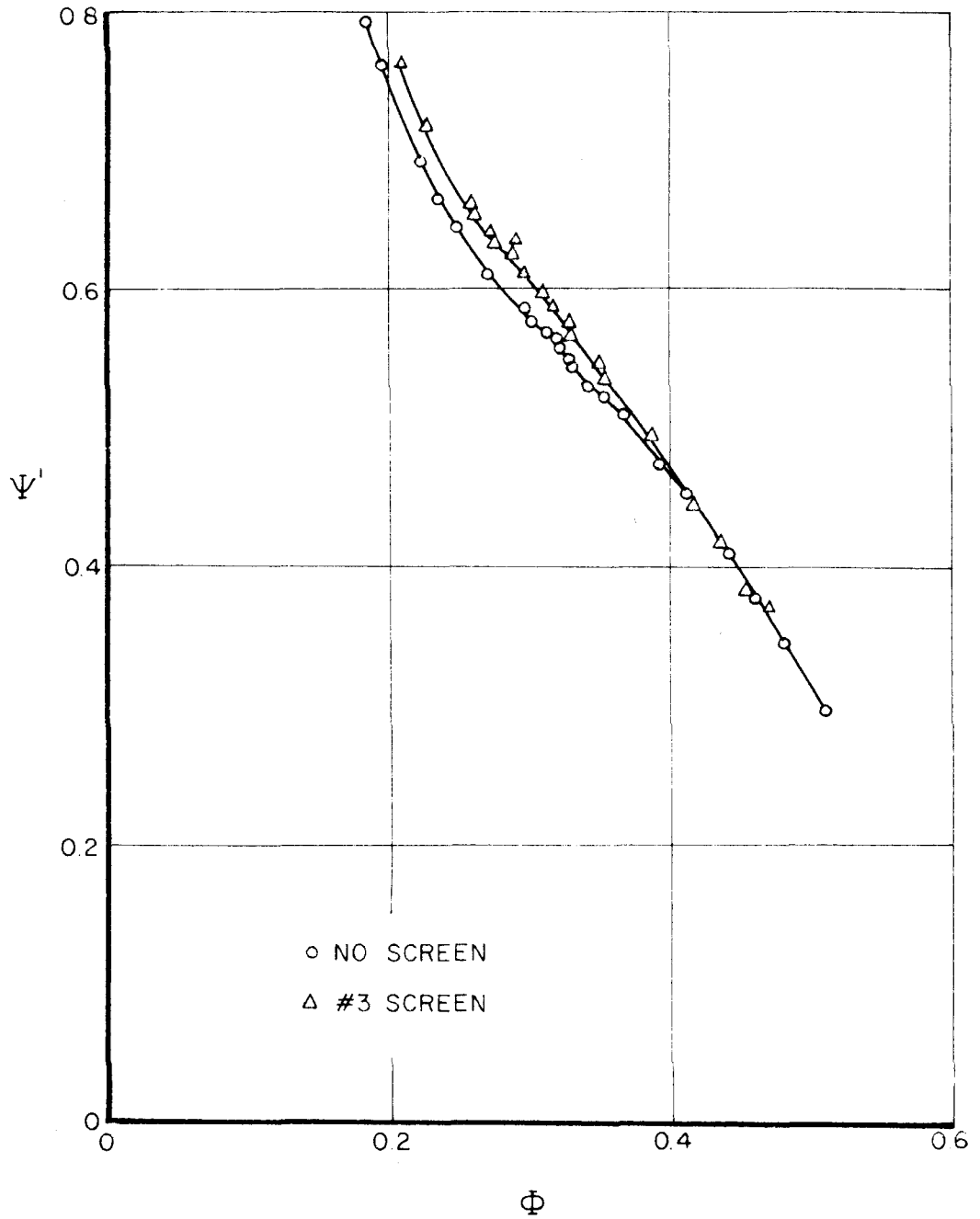
Fig. 70. Work Coefficient. Normal Single Stage Configuration.
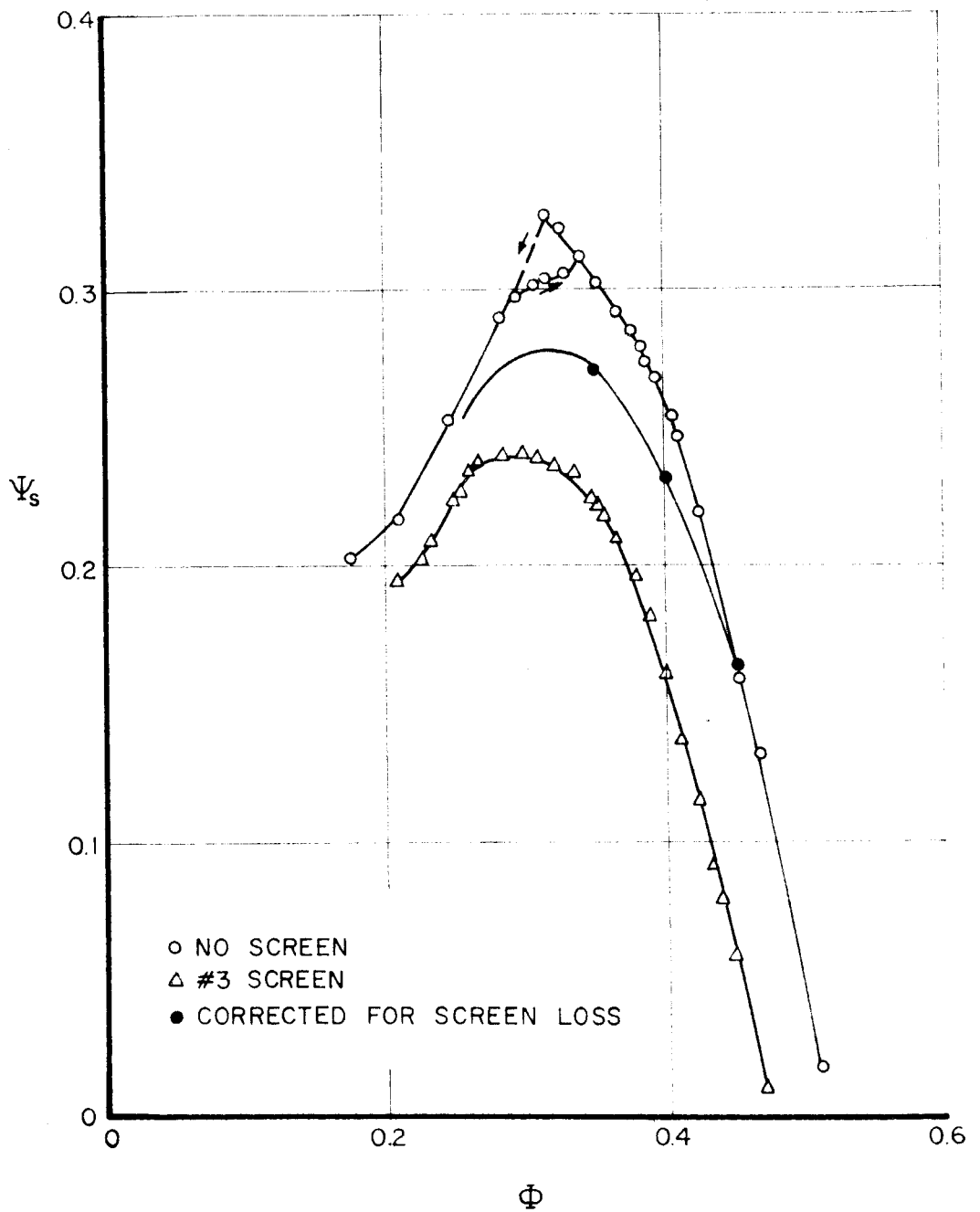
Fig. 71. Exit-Duct Static Pressure Coefficient.
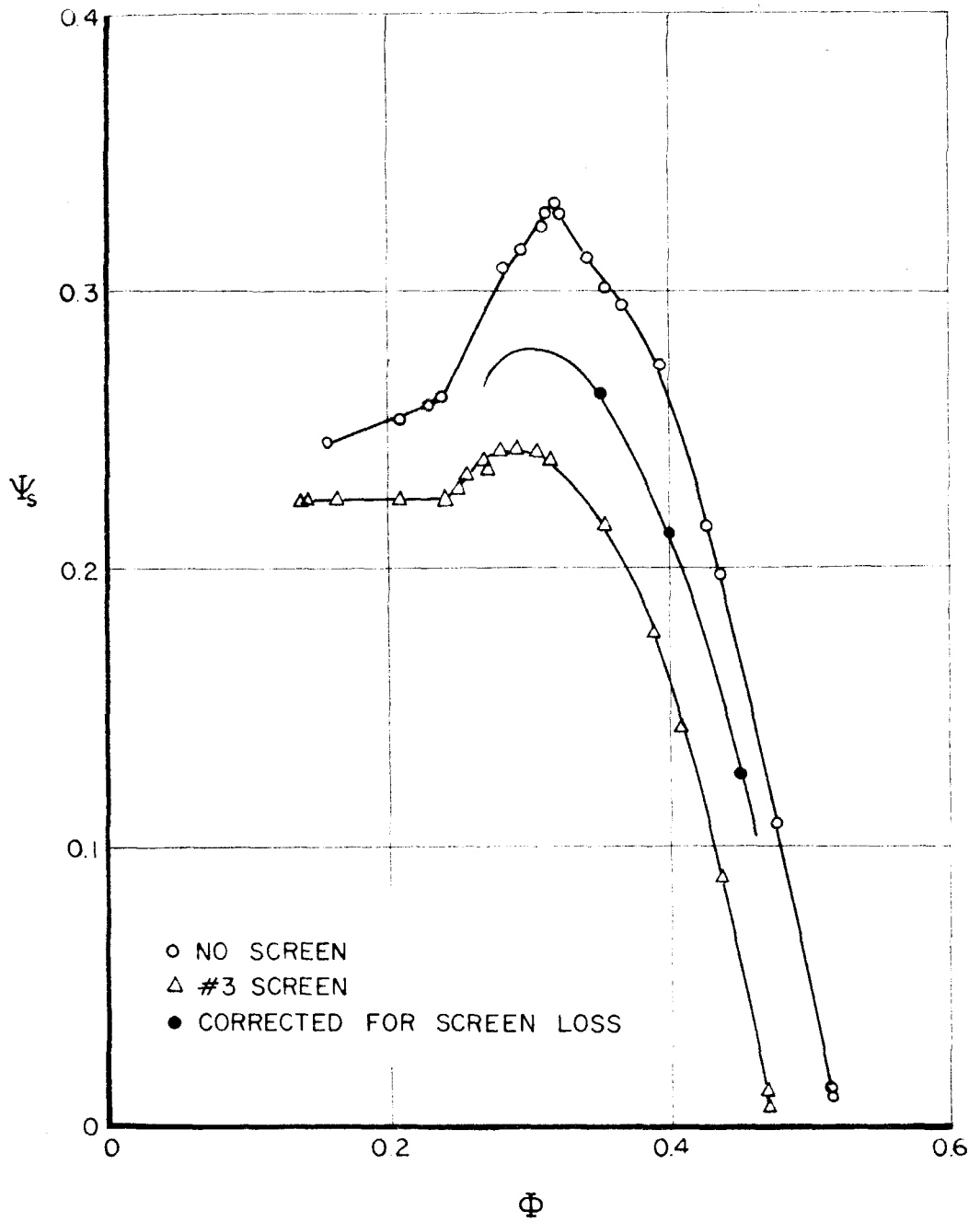
Expanded Single Stage Configuration.

Fig. 72. Exit-Duct Static Pressure Coefficient.
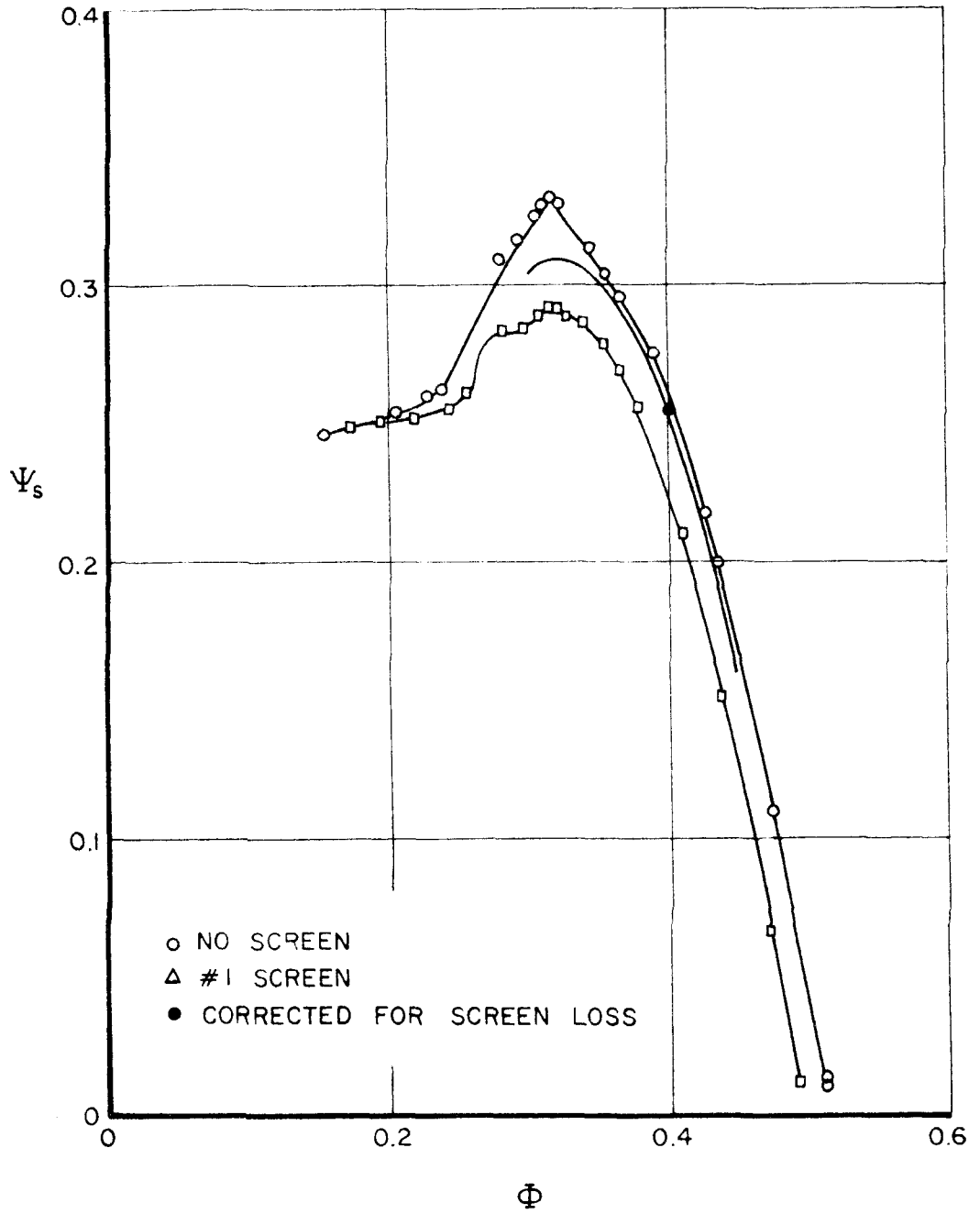
Normal Single Stage Configuration.

Fig. 73. Exit-Duct Static Pressure Coefficient.

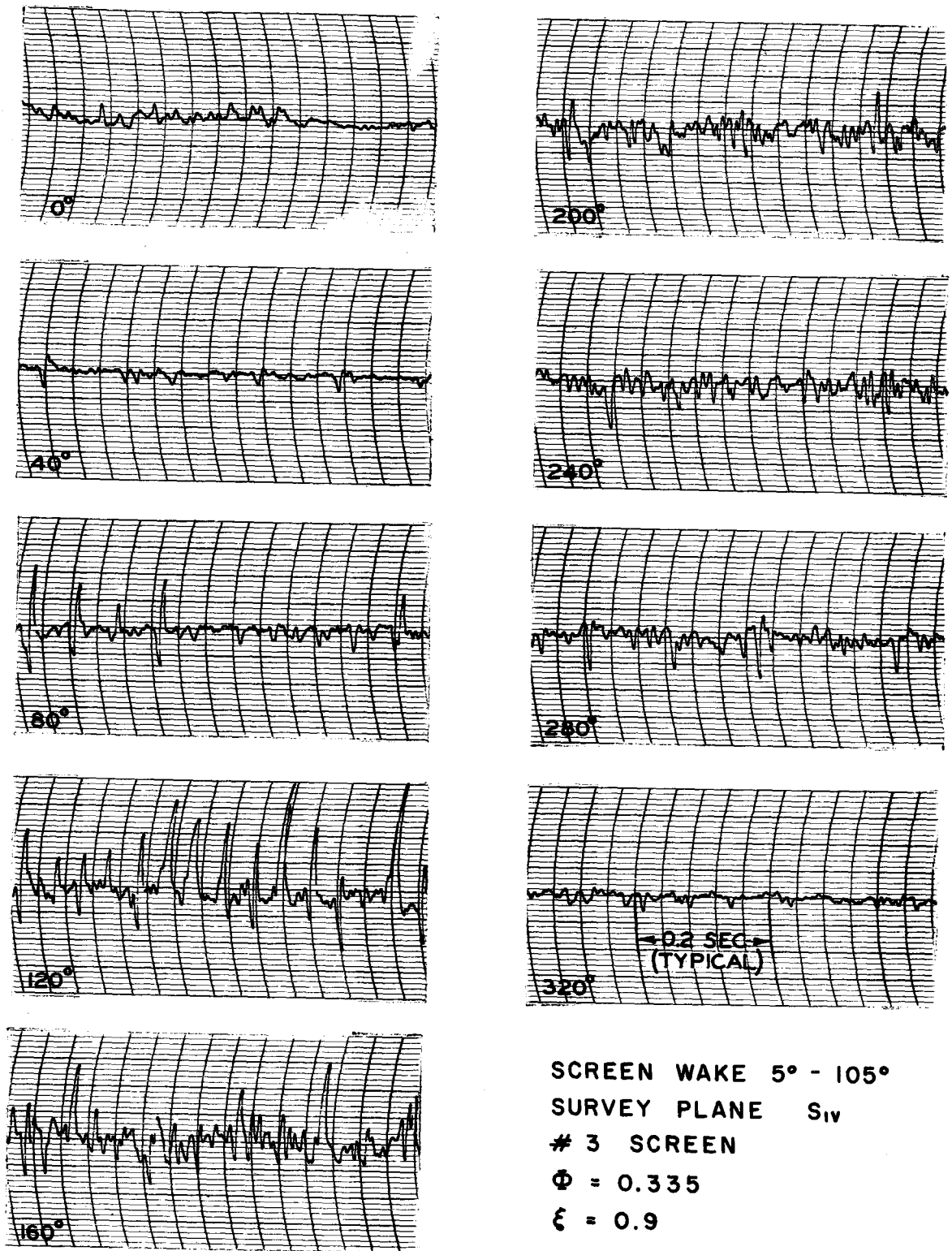Normal Single Stage Configuration.

SCREEN WAKE 5° - 105°
SURVEY PLANE S_{IV}
#3 SCREEN
$\Phi = 0.335$
$\xi = 0.9$

Fig. 74. Velocity Fluctuations at Intervals about the Circumference.
Expanded Single Stage Configuration.

148

SCREEN   WAKE   5° - 105°
SURVEY   PLANE S_{IV}
3   SCREEN
$\Phi = 0.28$
$\xi = 0.9$
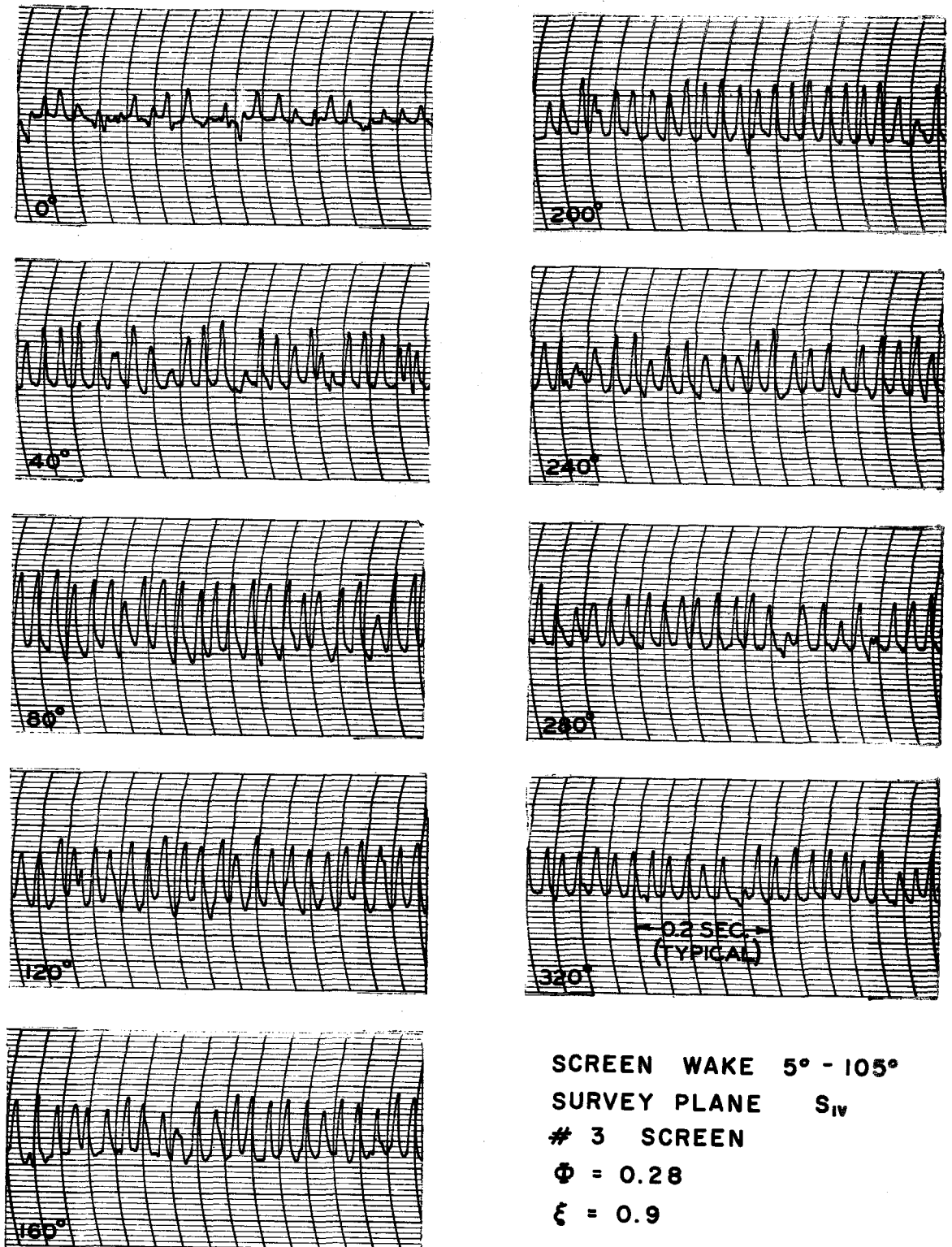
Fig. 75. Propagating Stall at Intervals about the Circumference.

Expanded Single Stage Configuration.

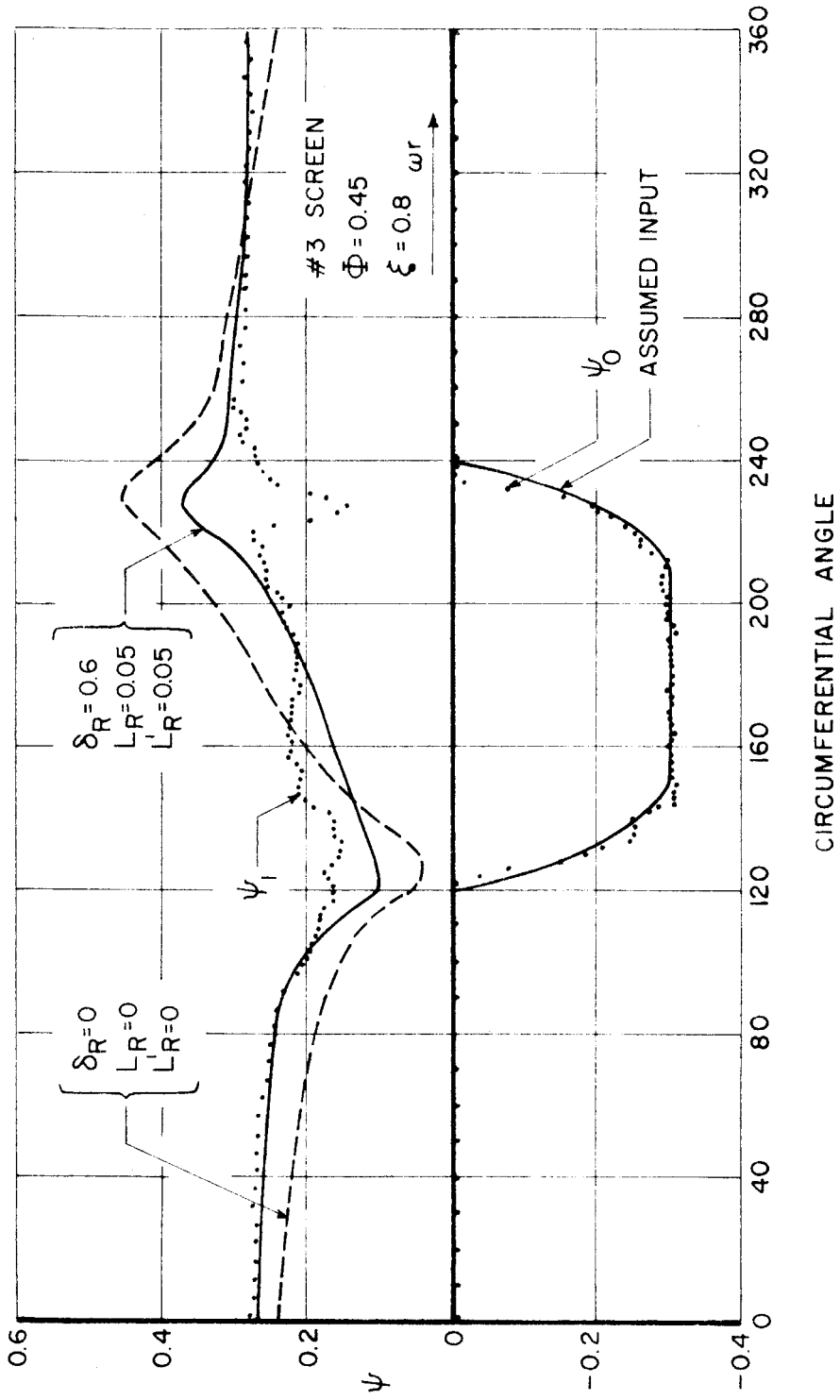
Fig. 76. Comparison of the Theoretical and Experimental Total Pressure Profiles.
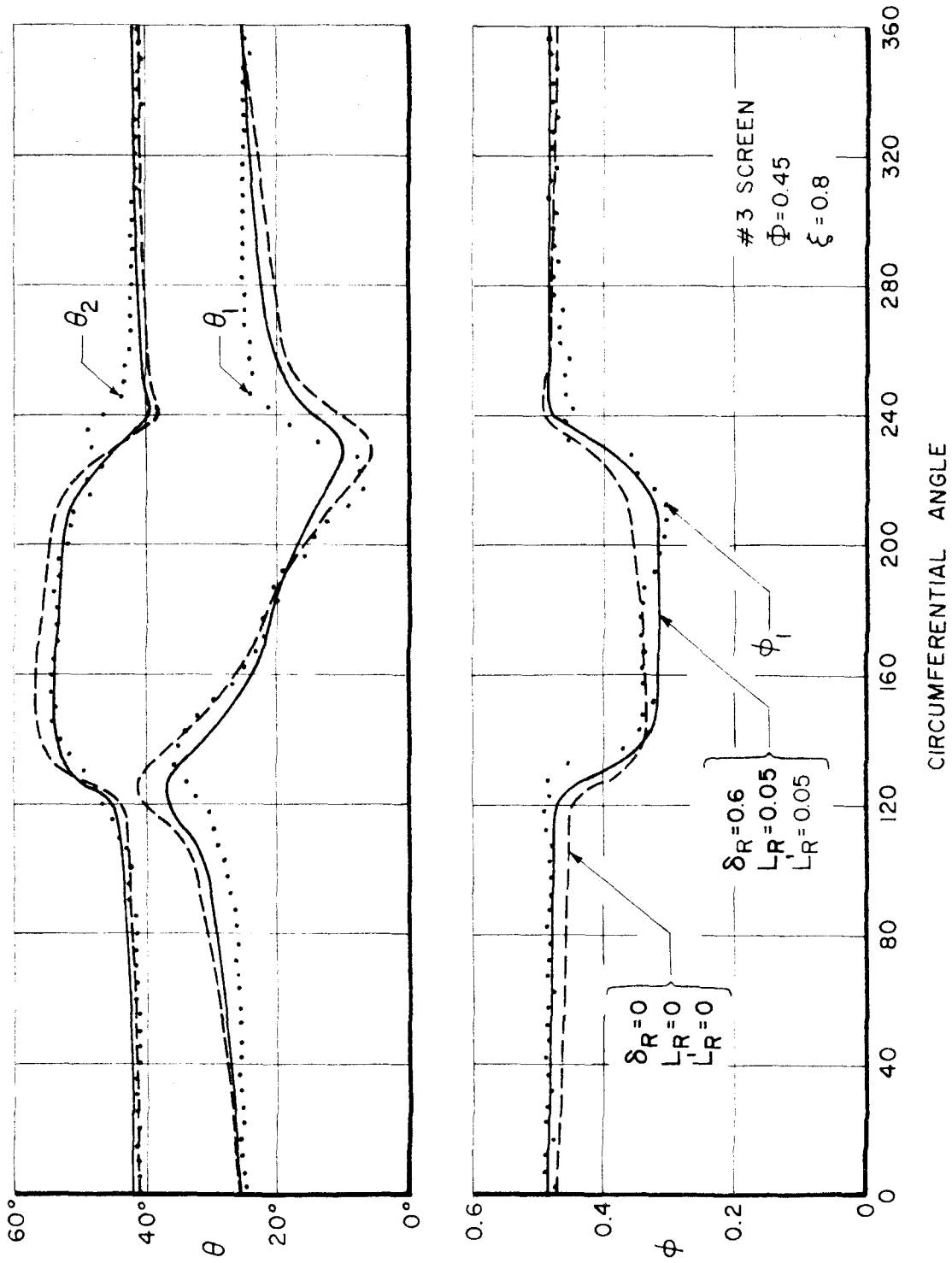Expanded Single Stage Configuration.

Fig. 77. Comparison of the Theoretical and Experimental Flow Angle and Flow
Coefficient Profiles. Expanded Single Stage Configuration.